Hydrodynamics of High-Speed Ship Transit near Level Ice

by

Zhihang Zhang

A dissertation submitted in partial fulfillment
of the requirements for the degree of
Doctor of Philosophy
(Naval Architecture and Marine Engineering)
in the University of Michigan
2023

Doctoral Committee:

Professor Kevin J. Maki, Chair
Professor Matthew D. Collette
Professor Krzysztof J. Fidkowski
Assistant Professor Yulin Pan

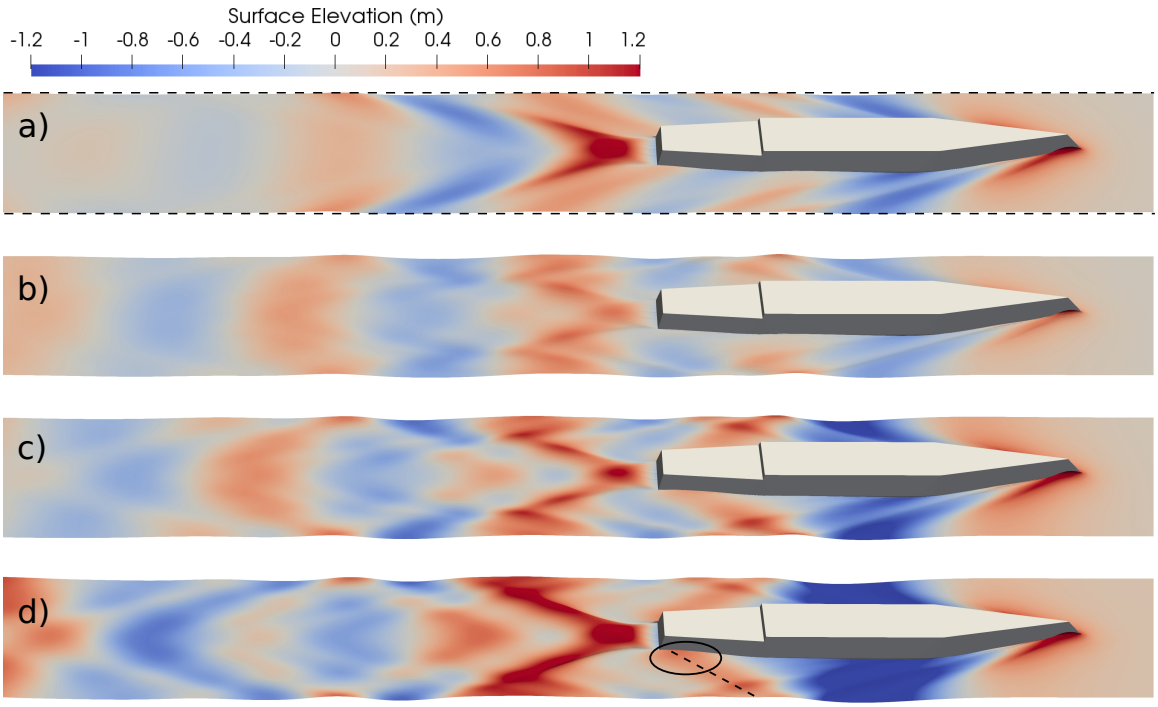

Wave fields for $Fr = 0.33$ with the full-scale ONRT, colored by surface elevation. From top to bottom are in a) open water, b) ice channels with $h^* = 0.05$ and c) $h^* = 0.2$, and d) a canal. For a) open water, the wave field is cut at the dashed lines although the domain has a width of $16B$. For b-d the channels and canal have a width of $w = 3B$.

Zhihang Zhang
zhihangz@umich.edu
ORCID iD: 0000-0001-9398-072X

Dedicated to the loving memory of my grandmother.

ACKNOWLEDGEMENTS

I would like to express my deepest gratitude to my PhD advisor, Professor Kevin Maki for his invaluable advice, continuous support, and patience during my PhD study. His immense knowledge and plentiful experience have helped me in both my academic research and daily life. Kevin is always happy to share his knowledge and perspectives in various subjects and the conversations with him have inspired me in many aspects of my life. I also want to thank my other committee members, Professor Krzysztof Fidkowski, Professor Matthew Collette, and Professor Yulin Pan for critiquing my thesis and giving their valuable insights.

I am grateful to Professor Alexander Korobkin and Professor Pentti Kujala for their advice on my research work. I also thank Dominic Piro for sharing his knowledge of the fluid-structure interaction solver to help the work with flexible ice sheets. I would like to thank my lab mates at the Computational Ship Hydrodynamics Lab (CSHL) for the valuable discussions.

My appreciation goes out to my parents for their understanding and endless support throughout my PhD journey. I am grateful to my fiancée Hongling for her tremendous love, encouragement, and support during the final year of the study.

TABLE OF CONTENTS

LIST OF FIGURES

Figure

LIST OF TABLES

Table

LIST OF ACRONYMS AND INITIALISMS

MYI Multi-Year Ice

NSR Northern Sea Route

NWP Northwest Passage

CFD Computational Fluid Dynamics

FEM Finite Element Method

FSD Floe Size Distribution

MIZ Marginal Ice Zone

RANS Reynolds-averaged NavierStokes

VOF Volume-of-Fluid

DOF Degrees-of-Freedom

FFT Fast Fourier Transform

BC Boundary Condition

MULES Multidimensional Universal Limiter for Explicit Solution

PISO Pressure-Implicit Split-Operator

ONRT Office of Naval Research Tumblehome

GPPH Generic Prismatic Planing Hull

Slerp Spherical Linear Interpolation

COG Center of Gravity

ABSTRACT

The annual average extent of Arctic sea ice has declined steadily in recent decades and the diminishing is expected to continue. Expansion of the duration and spatial extent of seasonal ice-free water will increase the accessibility of maritime activities in this polar region. Much of previous research for ship activities in the Arctic region has focused on ice-breaking operations that are limited to low speeds, where wave-making resistance is less important. Ships will seek to travel at higher speeds in the Arctic. Yet there is little research on high-speed ship transits in icy conditions. The problem of high-speed ship transit in the open water between large ice sheets (lead) is becoming an increasingly common scenario but has not been studied previously.

This dissertation presents a combined theoretical and numerical analysis of a ship traveling in a lead with the objective to understand how the ice sheets influence the ship hydrodynamics, and how the ice responds to the ship-generated waves. The first part of the analysis uses a mathematical model to evaluate the wave resistance in deep-water canals (or ice sheets of infinite thickness). The model is able to separate the contributions of the transverse and divergent waves to the total wave resistance. Significant influence of both the ship speed and canal width is observed to increase the wave resistance by as much as 129% or decrease by up to 82% relative to the open-water conditions.

The second part of the analysis uses high-resolution computational fluid dynamics (CFD) on a contemporary ship that is traveling between two rigid ice sheets of finite thickness. The CFD simulations identify the critical ice thickness that corresponds to the condition in which the ice sheets function nearly as canal walls. It is found that

the effect on the wave resistance is noticeable when the ice is 5% of the fundamental wavelength λ, and when the ice sheets are thicker than 20% of λ, the resistance change due to the sheet ice is nearly that of canal walls. CFD simulations are also performed for the same idealized canal from the first part, which demonstrate strong agreement in wave resistance with the theoretical analysis. The more accurate CFD confirms a 74% increase and 31% decrease of wave resistance in leads.

The last part of the analysis investigates the problem of a ship traveling in a lead between flexible ice sheets by using an adapted fluid-structure-interaction (FSI) solver. The FSI solver couples a moving CFD domain and a static ice sheet that is modeled as a thin elastic plate. The thin ice sheets are generally compliant with the water waves, where the ice deflections are found to correspond to the ship-generated waves. The maximum ice deflections always occur at the ice edge, which increases with ship speed and decreases with ice thickness. Overwash on top of the ice is found to be a significant phenomenon and greatly affects ice behavior. Higher overwash flux rates unexpectedly occur on thicker ice, which is explained by the smaller relative wave elevations for the thinner ice due to its compliance. Potential ice fractures are identified by using the Mohr-Coulomb yield criterion for sea ice, where both tensile and compressive failures are found for the higher ship speeds and most of them occur on the ice edge.

CHAPTER I

Introduction

1.1 Background and Motivation

The sea ice coverage in the Arctic region is rapidly evolving. Annual average Arctic ice extent has declined steadily in recent decades and the diminishing is expected to continue or accelerate through the century (Overland et al., 2019). Satellite measurements show that the Arctic has lost more than 50% of multi-year ice (MYI) during the period of 1999-2017 and MYI now covers less than one-third of the Arctic Ocean (Kwok, 2018). The heavy losses of thick MYI shifted the Arctic ice cover towards largely seasonal ice that does not grow thick enough to survive the summer. Predictions by climate models suggest a nearly ice-free Arctic in the summer is possible within a few decades (Overland and Wang, 2013; Overland et al., 2019; Landrum and Holland, 2020).

Expansion of the duration and spatial extent of seasonal ice-free water will bring changes in accessibility of maritime activities in the Arctic region (Council, 2009). This part of the planet sees increased traffic each year (Smith and Stephenson, 2013). Commercial ships see advantages to Arctic transit because compared to traditional routes via the Suez and Panama canals, the Arctic routes significantly reduce the travel distance between Asia, Europe, and eastern North America, yielding substantial time, fuel, and emission benefits (Hansen et al., 2016). For example, the Northern

Sea Route (NSR) and Northwest Passage (NWP) are two major alternative shipping routes. NSR shortens the transit distance from northern Europe to northeast Asia and northwest North America by up to 50% relative to the southern routes through the Suez or Panama Canal (Mulherin et al., 1996). NWP shortens the transit distance from western Europe to the Far East by 9,000 km compared to the conventional route through the Panama Canal (Howell and Yackel, 2004).

Figure 1.1: The Northern Sea Route and Northwest Passage.

The increasing global and Arctic temperatures will continue to open access to the Arctic, and both the number of ships and the Arctic shipping season length will continue to increase. However, there is still ice cover throughout the summer and transit using the established routes requires either an ice-strengthened hull or an ice-breaker escort (Melia et al., 2017). Ice breakers create channels in the ice leaving crushed ice between two large ice sheets. As the temperatures change the crushed ice can melt leaving an open-water ice channel (lead), which is demonstrated by the pictures in Figure 1.2. An idealized illustration of ship transit in a lead is depicted

(a) ice channel filled with crushed ice

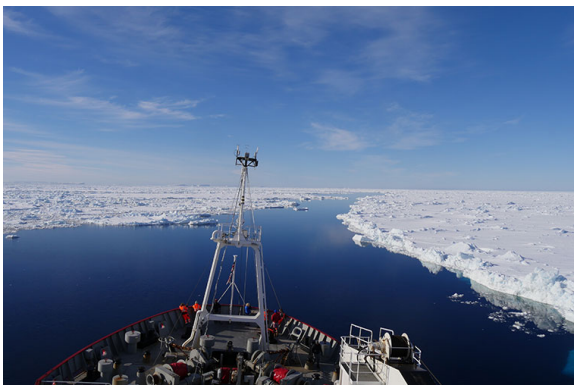

(b) open-water ice channel

Figure 1.2: Ships in ice channels.

in Figure 1.3 along with the open-water and canal conditions. For the lead scenario, the calm water surface is covered with a level ice sheet of uniform thickness that is separated by open water of constant width in the middle of the domain forming a channel. The typical Arctic ice thickness varies from 1 to 3 m (Kwok, 2018), and can be even thicker, especially when considering ridges.

In general, the conditions for Arctic transit are highly variable, and during transit a ship can see segments that are in open water, or partially confined water with solid ice nearby, or crushed ice in the channel between solid ice on either side. Ships will adjust their speed based on the local conditions. Ideally it travels at the target open-water transit speed, but lower speeds are required when the nearby ice is thick and the channel is narrow or full of crushed ice and larger floe ice (Luo et al., 2018).

The existence of ice affects the ship performance, including the ship resistance that is directly related to the required ship propulsive power, ship motions, and unsteady effects that concern safety and passenger comfort (Faltinsen, 2005). Experiments by Leiviskä et al. (2001) show that the ship resistance can more than double in narrow leads compared to that in open water. Newman (1962) shows by theoretical analysis that the wave resistance can increase or decrease $> 50\%$ in canals, where the canal walls can be regarded as ice sheets of infinite thickness. The unsteady effects are

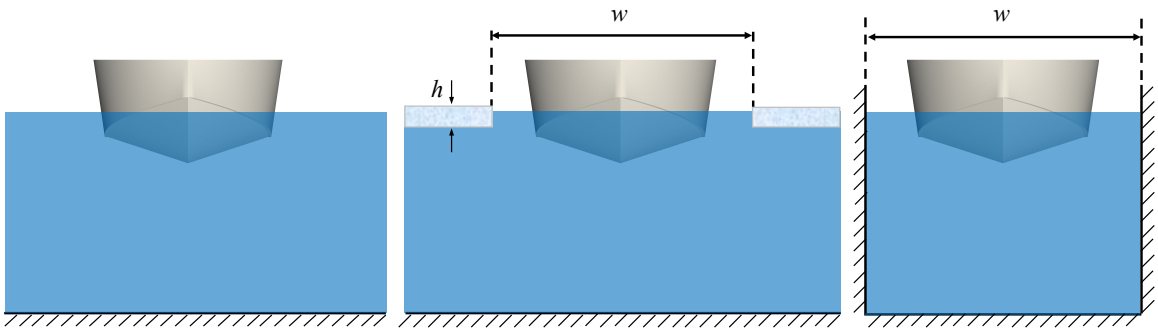

(a) open water (b) open-water ice channel (lead) (c) canal

Figure 1.3: Idealized illustration of three different scenarios for ship transit. Ship front is shown, w is the canal or channel width, h is the ice thickness.

the fluctuations in the ship resistance for a ship traveling in confined water, which occur even the ship has reached a constant speed for a long period of time. The unsteady effects not only impact the propulsive power requirement, but also may cause seasickness to passengers. Fluctuations up to around 50% of the steady resistance are found in the asymptotic analysis of deep-water canals by Doctors et al. (2008). On the other hand, the ship-generated waves can affect the sea-ice hydroelasticity and the integrity of the ice cover (Dumas-Lefebvre and Dumont, 2021), especially for the thin ice. For the problem of ship transit in open-water ice channels, the questions of what happens to the ship hydrodynamics and how the ice responds to the ship wakes as the ship speed and channel conditions change throughout transit need to be addressed. Understanding the involved ship-wave-ice interactions is essential for guiding future ship operations in icy conditions.

1.2 Literature Review

This section reviews the literature related to the topic of ship transit in a lead. First, previous research on ice-breaking activities are reviewed, where the operations are limited to low speed and the ice-breaking resistance is usually the main component

of the total resistance. The second part introduces the interactions between ocean waves and sea ice in a natural environment to discuss the hydroelasticity of ice sheets and the existing continuum models for governing responses of continuous ice covers, from which the thin-elastic-plate model is selected for modeling the flexible sheet ice. Then theoretical works on ship traveling in a canal are reviewed, which can be utilized to elucidate ship operations in a lead. The last part introduces the research on ship transit in a lead, where the investigation approaches include observations, experiments, theoretical analysis, and numerical simulations.

1.2.1 Ice Breaking at Low Speed

The majority of previous research for ship activity in the Arctic has focused on ice-breaking operations and how to strengthen the hull and transit at low speed (Valanto, 2001; Su et al., 2010; Myland and Ehlers, 2016; Li et al., 2021). Resistance in level ice is one of the main performance criteria for evaluating vessels operating in ice-covered waters. The total ship resistance for ice breaking can be divided into four distinct components (Spencer, 1992; Kim et al., 2013)

$$R_T = R_{br} + R_c + R_b + R_0, \tag{1.1}$$

where

R_T = total ship resistance in ice,

R_{br} = resistance due to breaking the level ice,

R_c = resistance due to clearing of the broken ice,

R_b = resistance due to buoyancy of the broken ice,

R_0 = open-water resistance.

A level-ice resistance test can be conducted to determine the total resistance R_T. The test is repeated, in which the ice sheet is cut to remove the ice strength but the ice pieces are in place, to determine the combination of three components $(R_c + R_b + R_0)$. The latter is called the *pre-sawn test*. The resistance due to breaking the level ice R_{br} is the difference between the two. Open-water resistance R_0 is known from open-water tests. At low ship speed, R_0 and R_c are small, R_{br} is thought to be the main component of the total resistance for breaking high-strength level ice.

Figure 1.4: Breaking patterns of model ice under water with two different ship models. From Fig. A6. in Myland and Ehlers (2016).

The important parameter to characterize ship speed is the ship-length Froude number $Fr = U/\sqrt{gL}$, where U is the ship speed, g the acceleration of gravity, and L the ship length. Herein the speed is considered low in the sense that the wave resistance is small, and this corresponds to conditions when $Fr < 0.15$ (Myland and Ehlers, 2016; Li et al., 2021; Riska et al., 2001). There is very little previous work done on the influence of ice sheets on the wave resistance of ships when traveling at higher speeds when the wave resistance is not small, (*i.e.* $Fr > 0.15$). The design speed of commercial vessels for open-water operation is often in the range $0.15 < Fr < 0.25$, in which there is significant wave resistance. Naval vessels can travel even faster, and reach Froude numbers up to $Fr \approx 0.4$ and even higher. With the new transit routes

of the Arctic with more open water segments and proximal sheet ice, it is important to understand the influence of the ice on the ship resistance for speeds in which the wave resistance is important. The presence of ice near the ship alters the wave resistance, both beneficially and detrimentally, and this has important ramifications for fuel efficiency, emissions, safety, and for time of transit and logistical planning.

1.2.2 Wave-Ice Interactions and Ice Modeling

A closely related topic to the ship-wave-ice interactions is that of environmental ocean waves and sea ice. Sea ice is found in various forms including loosely compacted ice floes, pancake ice, grease ice, frazil, and continuous ice plates. Many theoretical models have been constructed to describe how sea ice affects ocean waves, and vice versa. In these models, the sea ice is presumed to be elastic, viscous, or visco-elastic. Each assumption is reasonable under various circumstances, but there is no comprehensive model that can describe the interaction between surface gravity waves and all types of ice covers (Squire, 2020).

In the marginal ice zone (MIZ), which is the boundary between the open ocean and ice-covered seas (see Figure 1.5), such interactions usually occur on small to medium scales in terms of the relative size of sea ice to ocean waves as the floe sizes in the MIZ are generally smaller due to wave-induced ice breakage and the ice cover is therefore normally less compact. Internal stresses are less important than other forces (e.g. floe-floe collision forces) for the compact ice packs because ice floes tend to move laterally. In this region, understanding how the surface waves affect the floe size distribution (FSD) is required to define the MIZ (Williams et al., 2013; Montiel and Squire, 2017; Montiel and Mokus, 2022; Mokus and Montiel, 2022).

For large floes or consolidated ice sheets, the ice is highly compact and deforms in response to stresses imposed by currents and waves, known as the hydroelasticity of sea ice. The length scales associated with the ice cover are large enough and its

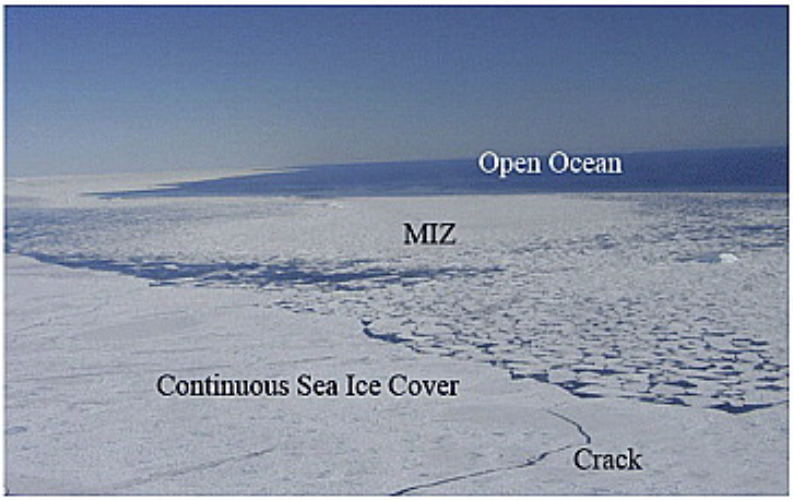

Figure 1.5: Marginal ice zone (MIZ) of Prydz Bay. Photo from Lu et al. (2008).

integrity is sufficiently high that the ice may be regarded as quasi-continuous. Several continuum models have been developed, including the mass-loading model, the thin-elastic-plate model, the viscous-layer model, and the visco-elastic model. This dissertation concerns continuous sheet ice and all these continuum models are appropriate candidates for modeling the flexible sheet ice in this work. The mass-loading model considers the ice cover as a collection of noninteracting point masses (Peters, 1950; Wadhams and Holt, 1991). The thin-elastic-plate model assumes that sea ice behaves as a homogeneous semi-infinite thin elastic plate. Many features of the ice response can be described by the thin-elastic-plate model, but since the initial model cannot predict energy attenuation, additional mechanisms have been adopted to model the energy loss (Wadhams, 1973; Squire, 1984). The viscous-layer model, first introduced by Weber (1987) and improved by Keller (1998), considers the ice layer as a suspension of solid particles. Wang and Shen (2010) proposed a visco-elastic model to describe the ice-ocean system as a homogeneous visco-elastic fluid layer overlaying an inviscid layer of water by generalizing earlier models of ice-coupled wave propagation in continuous ice (Fox and Squire, 1994; Keller, 1998). Viscosity is suggested to come from the interactions of particles like ice floes that are much smaller than the

wavelength, and the elasticity property comes from the rigidity of ice floes in which floe sizes are relatively large compared to the wavelength. A summary of the applicability of different models for governing sea ice covers is provided, which depends on the elasticity and viscosity of the ice field. In general, the thin-elastic-plate model is more suitable for large rigidity and viscous-layer model is better for small rigidity, and visco-elastic model is in between. For this work, the thin-elastic-plate model is selected for governing the flexible ice sheet considering the large modulus of rigidity of the sheet ice ($\mathcal{O}(10^9)$Pa) as well as the simplicity of the model.

1.2.3 Ship Traveling in a Canal

Whereas high-speed transit of a ship near ice sheets has not been been studied in detail in the past, the problem of a ship traveling in a canal, where two side walls extend to the bottom (see Figure 1.3c), is a related problem that has been extensively studied. By constructing the relationship between operation in a canal and transit in water bounded by adjacent sheet ice, the knowledge from operation in a canal can be utilized to develop understanding of Arctic transit.

An early example of the study of operation in a canal is Newman (1962). In that work the problem of a uniform pressure distribution, which represents an idealized ship of shallow draft, is studied for the case of constant-speed travel in a canal of finite width and depth. The *method of images* was used to create canal walls by using a number of identical pressure distributions that are spaced laterally with the distance corresponding to the canal width. Figure 1.6 plots the wave resistance in a canal relative to that in open water as functions of Froude number and canal width, which are calculated using the *method of images* from Newman (1962) with a rectangular pressure patch. In their analysis, both significant increase and decrease in wave resistance are found, which are $> 50\%$ of the open-water resistance, and the effects are most pronounced for Froude number less than 0.5, and in the case of narrow

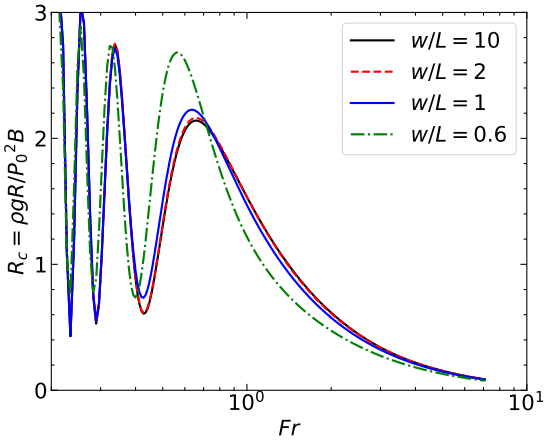

(a) non-dimensionalized wave resistance R_c as a function of Froude number

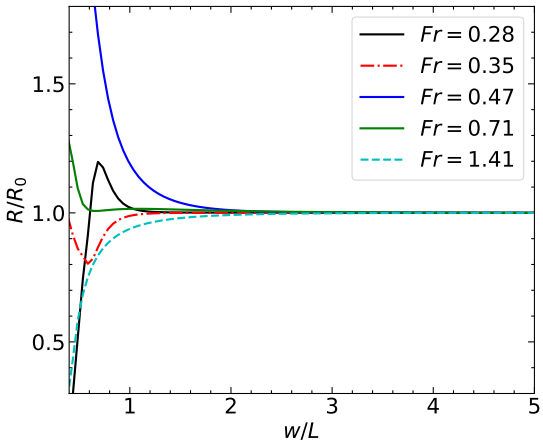

(b) relative wave resistance as a function of canal width

Figure 1.6: Reproduction of the plots for relative wave resistance of a rectangular pressure patch in canal, calculated using the *method of images* from Newman (1962). The pressure patch has a length of $L = 0.86$ m and a width of $B = 0.33$ m, which resembles the waterline of the model scale planing hull used in this work. w is the canal width, R_0 is the wave resistance in open water, $g = 9.81$ m/s^2.

canals. A limitation in the analysis is that a pressure patch is suitable for ships that have very shallow draft (their vertical extent being much less than their lateral or longitudinal length), which is not always the case for many ships.

Instead of using an array of images of a pressure patch, an array of images of an individual hull can be used to represent a multihull vessel. Most multihulls have either two or three hulls (catamaran or trimaran), but if the number of hulls is sufficiently large, then a canal-like boundary condition is implicitly present on the midplane between the inner most hulls. The solution on the midplane between individual hulls is like a symmetry plane, and thus a canal. This concept is used in the theoretical model in this thesis and is based on the wave resistance of multi-hull vessels studied in detail in Tuck and Lazauskas (1998); Faltinsen (2005).

The previously cited studies for either a pressure patch or multihull show a dramatic increase or decrease in wave resistance of a ship traveling in a canal, but much less attention is paid to the resulting wave field. The wave pattern around the hull

can be used to elucidate wave interaction that leads to the favorable results of reduced wave resistance. For example, Chen and Sharma (1997) demonstrates theoretically that a slender ship moving in a shallow water canal at supercritical speed can make wave resistance vanish, which was explained through the favourable interference of the reflected bow waves and the stern waves. The analysis of the wave field is used in this work to show how the ship in ice may alter speed to achieve fuel savings.

1.2.4 Ship Traveling in an Open-Water Ice Channel

Open water between large ice sheets, or leads, are common features of polar ice fields and can be formed when a crack opens either by ice-going vessels or divergent forces due to ocean currents and wind. As shown in Figure 1.7, modern ice-breakers are able to create open-water ice channels through level ice by flushing the broken ice fragments out of the channel. When a lead is narrower than the beam of the navigating ship, the ship has to break some ice by itself (Li et al., 2021). If the lead is wider than the ship, the ship will be able to travel in the open water with two ice sheets on either side. Although if the lead is wider than the ship beam there could be no direct ship-ice interactions, the ship performance will still be influenced by the existence of the ice sheets through the wave pattern changes.

Figure 1.7: Ice-breakers creating open-water ice channels either in straight-ahead or oblique mode. Pictures courtesy of Aker Arctic.

1.2.4.1 Observations and Experiments

There is specific work for ships that operate in a lead. In situ observations of wave-induced sea ice breakup in natural environment were reported in Dumas-Lefebvre and Dumont (2021), where a coast guard ship sailed at constant speed near large ice floes (0.3 to 0.5-meter thick) to create waves and footage was recorded to obtain the temporal evolution of the ice breakup and resulting floe size distribution (FSD). Figure 1.8 shows an image of sea ice breakup from the edges caused by ship-generated waves. The incident wavelength, which is suggested to belong to waves of maximum amplitude and propagate at the angle, $\theta = \arcsin(1/\sqrt{3}) \approx 35°16'$ with respect to the ship track, was found to be a determinant of the maximum ice floe size besides the ice rigidity. The comparison of the observed breakup extents showed that the thicker ice broke up much further from the ice edge than the thinner ice, while the incident waves were similar in terms of period, wavelength and amplitude for both experiments. Dumas-Lefebvre and Dumont (2021) suggested that thicker ice can attenuate waves less than thinner ice, which may contradict some proposed theories. Floe-area-weighted FSDs exhibit a modal shape, indicating that a preferential size is generated by wave-induced breakup. Furthermore, the increase of the mode of the distribution with greater thickness indicates that ice thickness plays a defined role in determining the preferential size.

Model tests were conducted by Leiviskä et al. (2001) in an ice tank to investigate the effects of ship speed and channel width on the ship resistance. The layout of the ice tank in the experiments is shown in Figure 1.9, in which B is the ship beam and W is the channel width between the two ice sheets made of model ice. Various ice sheets of different ice thickness, stiffness (Young's modulus) and strength were tested. Figure 1.10 shows the resistance of the ship model in the ice channel relative to that in open water as a function of ship speed and relative channel width (W/B). Note the ship model has a length of 5.215 m, the ship speed of 1 m/s corresponds

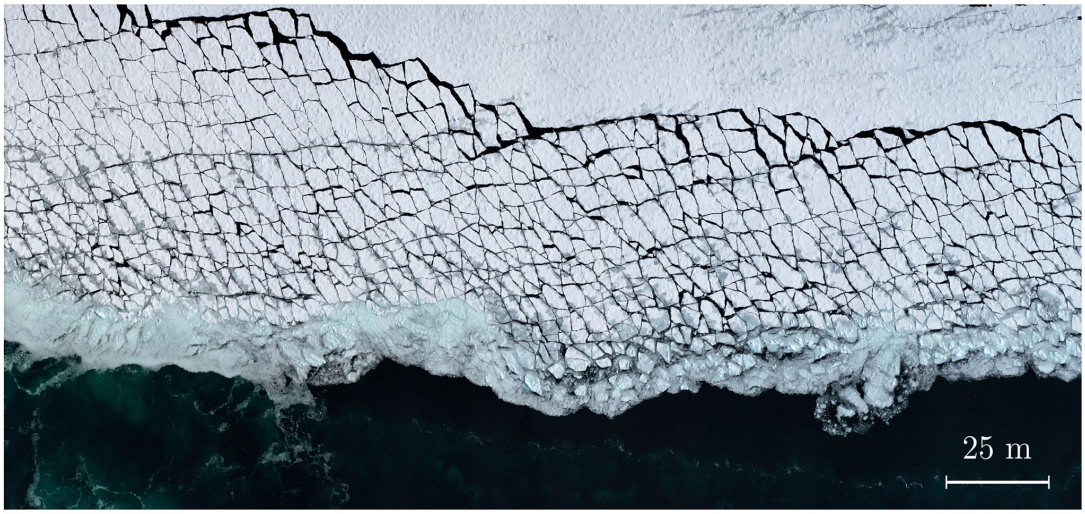

Figure 1.8: Breakup of sea ice sheet caused by ship-generated waves. Picture from Dumas-Lefebvre and Dumont (2021).

to $Fr = 0.14$. Significant increase in the ship resistance is found in narrow channels with a relative resistance of $R/R_0 > 2$, which indicates an increase over 100% relative to that in open water.

1.2.4.2 Theoretical Models

Recently a theoretical model was used to investigate the problem of a ship traveling in open-water ice channels, where a pressure load is employed to mimic the ship hull and ice covers are treated as a thin elastic plate or visco-elastic plate. Ren et al. (2016) investigated the wave-excited motion of a body floating on water confined between two semi-infinite ice sheets, where the fluid was treated as ideal and the ice sheet was modeled as an elastic thin plate. Added mass and damping coefficients of the body due to the ice sheets and excitation force were analyzed in the work, which were found to be different from that in open sea. Resonant behaviour with extremely large motion was found to be possible under certain conditions. Similarly, Shishmarev et al. (2016) studied the fluid beneath the ice sheet using potential-flow theory and the hydrodynamic pressure on the ice-fluid interface was given by the linearised Bernoulli

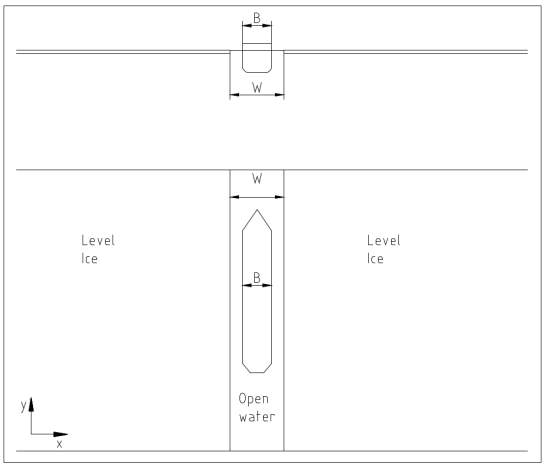

Figure 1.9: The layout of the ice tank in the experiments by Leiviskä et al. (2001).

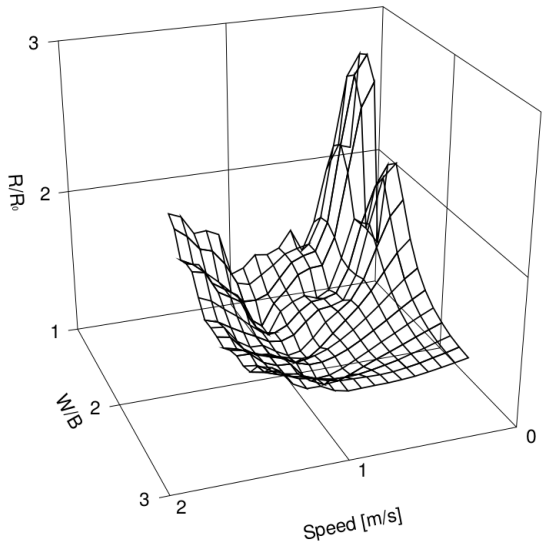

Figure 1.10: The relative resistance as a function of ship speed and channel width (Leiviskä et al., 2001).

equation. The ice sheet was modeled as thin visco-elastic Kelvin-Voigt plate and the deflection of the ice sheet w is described by

$$Mw_{tt} + D\left(1 + \tau\frac{\partial}{\partial t}\right)\nabla^4 w = -P(x, y, t) + p(x, y, 0, t), \tag{1.2}$$

where M is the mass of ice per unit area, D is the ice rigidity, τ is the retardation time accounting for the viscosity, p is the hydrodynamic pressure and P is the external pressure. The equation can be solved mathematically with Laplace's equation for velocity potential and the boundary conditions for the ice deflection and fluid velocity. The results show that the dynamic component of the fluid pressure is important for the accurate prediction of ice-fluid interaction and multiple critical speeds of hydroelastic waves, at which amplified ice deflection and stress occur, were also observed. Xue et al. (2021) investigated the hydroelastic response of floating ice sheets with open water between them and a moving load either in the open water or on the ice sheet. The flow under the ice was modeled as potential and linear by a boundary-integral method,

and the ice was modeled as a visco-elastic plate. The effects of the ice thickness, lead width and load properties on the critical speeds were investigated, and the moving speeds that provide the maximum ice deflection, maximum stress in the ice, and maximum wave-making resistance, were determined separately. Figure 1.11, which is from that paper, shows the maximum deflection and stress along the ice edge as a function of ship speed. It is shown that the ice deformation is very small for speeds that are smaller than the critical speed. As the speed is increased towards the critical speed (peak of the curve) the deformation grows rapidly and reaches a maximum, and then as the speed continues to increase the ice deformation slowly decreases. The hydroelastic responses of thin ice sheets were also mathematically studied by other researchers (Li and Wu, 2021; Khabakhpasheva and Korobkin, 2021; Li et al., 2017), where the effects of the ice dimensions and load properties on the hydrodynamic forces and ice responses were investigated. Li and Wu (2021) finds that the existence of the ice sheet leads to an oscillatory behavior of the hydrodynamic force compared to open-water condition. The oscillatory force implies that ships can have motion when operating in otherwise calm conditions.

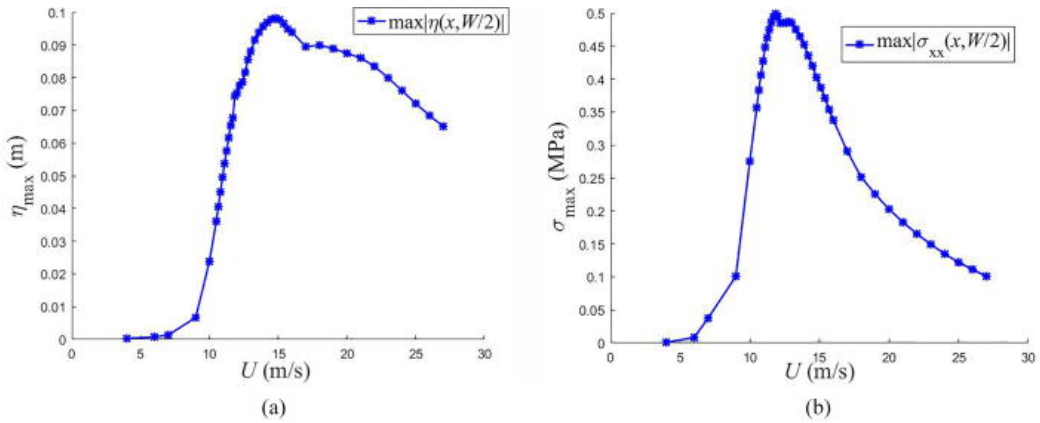

Figure 1.11: (a) Maximum deflection that peaks at $U = 14.8$ m/s and (b) maximum stress along the ice edge that peaks at $U = 11.85$ m/s. The ice thickness is 0.4 m and the Young's modulus is $E = 5$ GPa. From Figure 19 in Xue et al. (2021)

Theoretical models have provided great insight into sea-ice hydroelasticity, but

they are built upon certain assumptions and can exclude some non-trivial phenomena, such as wave nonlinearity, realistic ship geometry, and effects such as turbulence, viscous separation, viscous wave damping, and the overwash on floating bodies of small freeboard (Skene et al., 2018). Recent experiments assessed the accuracy of existing theoretical models in certain scenarios of wave-ice interactions, which showed these assumptions can cause considerable deviations. Bennetts and Williams (2015) conducted experiments to investigate the transmission of regular water waves by arrays of floating discs in a wave basin and compared it with theoretical predictions that are based on potential-flow theory and the thin elastic plate model. Agreement was found except for tests with large-amplitude waves and dense arrays of discs, where they attributed the loss of model accuracy to the wave-energy attenuation due to overwash. Nelli et al. (2017a) measured the wave fields reflected and transmitted by thin floating plastic plates with or without edge barriers that are equipped to restrict overwash waves. The proportion of energy transmitted by the plates without barriers was shown to decrease as the incident waves become steeper, which the authors hypothesized to be related to the wave energy dissipation due to wave breaking in the overwash region. Other two experimental studies (Toffoli et al., 2015; Yiew et al., 2016) also suggests increasing wave energy dissipation happens due to overwash with large-amplitude waves.

1.2.4.3 Numerical Simulations

Computational Fluid Dynamics (CFD) is an approach for modeling hydrodynamic problems in which the Navier-Stokes equations can be numerically solved with the inclusion of turbulence models and complex and realistic structural geometry.

CFD approaches have been successfully applied to study wave-ice and ship-wave-ice interactions. Bai et al. (2017) used both the potential-flow model *HydroSTAR* and a viscous-flow OpenFOAM solver to simulate the kinematic response of small

sea-ice floes in regular waves. The results were compared against experimental data and suggested the potential-flow solver overestimated the heave and surge Response Amplitude Operators (RAOs), while OpenFOAM provided a much better agreement with the experimental data. Nelli et al. (2017b) also employed the OpenFOAM solver *IHFOAM*, which was developed by Higuera et al. (2013) and solves for Reynolds Averaged Navier-Stokes (RANS) equations, to simulate wave reflection and transmission by a floating thin plastic plate. The comparison with the experiments conducted in Nelli et al. (2017a) also validated the ability of the numerical model to accurately predict the energy dissipation in the overwash process.

Huang et al. from University College London authored a series of works focussed on wave-ice or ship-wave-ice interactions with CFD. Based upon the work of Tuković et al. (2018), Huang et al. (2019) presented a Fluid-Structure-Interaction (FSI) solver within the framework of OpenFOAM to simulate the hydroelastic response of a large ice sheet in regular waves. In the solver, both the fluid domain and solid domain were solved with the Finite Volume Method (FVM), where the ice deformation was governed by the St. Venant Kirchhoff solid model and the interactions were achieved through a two-way coupling between the fluid and solid solutions. The validation against experiments of Sree et al. (2017), Nelli et al. (2017a) and Skene et al. (2015) showed good agreement in predicting wave reflection and transmission. Compared with theoretical methods, the numerical model demonstrated the capability in predicting overwash and the associated wave energy dissipation with the incorporation of interface capturing technique through the Volume of Fluid (VOF) approach (Hirt and Nichols, 1981). In Huang et al. (2020), CFD was used to simulate a ship traveling in water with small floating ice floes, where the Discrete Element Method (DEM) was coupled to govern the ice motions and the ship-ice/ice-ice collisions. Froude numbers from 0.06 to 0.18 were considered for the simulations. The accuracy of this model in predicting the ice-floe resistance was confirmed by the towing tank tests (Guo et al.,

2018). An empirical equation that can quickly predict the effects of ice floes on ship resistance was derived based on the same model (Huang et al., 2021b). Huang et al. (2021a) simulated a KRISO Container Ship (KCS) model advancing in an open-water channel between two rigid ice sheets at speeds between $Fr = 0.03$ and 0.12. Channel width from 1.1 to 3 times the ship beam and ice thickness from 10% to 30% of ship draught were tested and their influences on the ship resistance and wave pattern were analyzed. An increase in the pressure component of the ship resistance was found in the case of narrow channels at the lower speed $Fr = 0.03$. Ice thickness was varied for $Fr = 0.03$, in which tests the ship resistance plateaued after ice thickness reached 15% of ship draught, suggesting that the ship-generated waves were largely reflected by the thick ice edges which function nearly as canal walls.

1.3 Research Gap and Open Questions

Following the research overview on ships traveling in canals or ice channels, clear research gaps can be identified.

Much previous research for ship activity in the Arctic has focused on ice-breaking operations at low speeds. Research on ship transit in open-water ice channels is rare. Among the handful works, Huang et al. (2021a) is the only numerical work but is limited to a low-speed regime ($Fr < 0.12$) and rigid-ice assumption. Higher-speed transit ($Fr > 0.2$) of a ship near sheet ice has been not been studied in the past. The Arctic is already been used for tourism, military and rescue ships that will seek to travel at higher speeds. More dramatic changes in ship hydrodynamics and wave fields occur at higher speeds, understanding the involved ship-wave-ice interactions in higher-speed regime is essential for guiding future ship operations in icy conditions. The ship-generated-waves can also affect the integrity of the ice covers, which has a potential impact on the Arctic environment and can cause destructions to the

open-water ice channels that are maintained by ice breakers. Therefore, it is also indispensable to assess the ice reponses to the ship-generated waves by modeling the fluid-structure interactions between the ship wake and sea ice.

In the past three decades, sea ice hydroelasticity subject to ocean wave loads has been extensively studied with theoretical models. However, theoretical models can exclude some non-trivial phenomena, including wave nonlinearity, realistic ship geometry, and overwash. Recent experiments indicate that the ideal assumptions used for these theoretical models can cause considerable inaccuracies. Theoretical models tend to underestimate wave energy dissipation as the wave breaking occurring in the overwash process is not taken into account. Numerical models capable of simulating ship-wave-ice interactions under high ship speeds with adequate fidelities and reasonable cost have yet to be proposed or demonstrated.

Ship transit in open-water ice channels is a complex hydrodynamic problem with multiple sub-problems involved. Figure 1.12 depicts the sub-processes in the ship-wave-ice system for the problem of ship-transit in open-water ice channels. No direct contact happens between the ship and ice in this problem, while the wave acts as the means to transfer the momentum and energy. This complex problem also involves many variables, which include but are not limited to the water depth, hull geometry, ship speed, channel width, ice dimensions (ice thickness, draft and freeboard, and ice extent), and other ice properties that determine the ice flexure and internal stresses. The large number of dimensions of variables presents a difficult challenge in the full-spectrum analysis of the problem, so development of an efficient and affordable investigation method is necessary.

There are some open questions regarding this engineering problem that are worth answering.

1. As the theory of free water waves suggests the momentum and energy transfer concentrates in the vicinity of the free surface with an exponential decay with

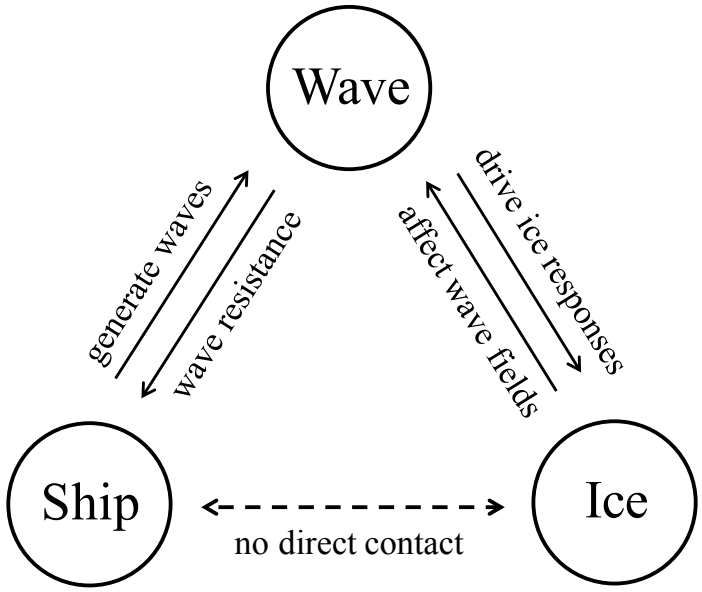

Figure 1.12: Illustration of ship-wave-ice interactions for the problem of ship-transit in open-water ice channels. Adapted from Huang et al. (2021a).

depth in the water, it is reasonable to assume sheet ice functions as canal walls if the ice is thick enough. What is the critical ice thickness above which the ice sheets can be treated as canal walls?

2. A ship traveling in a canal is a related problem to that of ship transit near an ice sheet, and has been extensively studied with theoretical methods. Theoretical methods are more efficient and affordable compared with experiments and CFD simulations. Can we utilize the wave pattern analysis to deepen and generalize the analysis of ship hydrodynamics in a canal and further extend the analysis to elucidate the problem of ship transit in a lead?

3. How do the ship speed, channel width and ice thickness affect the ship resistance, ship motions, wave fields, and ice responses?

4. The ice flexure greatly depends on the ice thickness. How does the ice flexure affect the ship hydrodynamics?

5. What determines the amount of overwash on top of the ice? How does the

overwash affect the ship hydrodynamics, wave fields, and ice behaviors?

1.4 Overview of Thesis

Numerous studies have focused on ship-ice interactions in ice-breaking through level ice, and ocean wave and sea ice interactions, where investigation approaches have been well established. Yet there lacks of work into high-speed ship transit in open-water ice channels, which is becoming an increasingly common scenario in the polar region as leads are created by modern ice breakers or due to ocean currents or wind.

This work proposes to investigate the ship-wave-ice interactions for ship transit in open-water ice channels with high-resolution CFD models, where a high-speed regime of $0.2 < Fr < 1.4$ is studied. Ship resistance, ship motions, wave fields, and ice responses are analyzed.

An idealized scenario is constructed for the problem of ship transit in a lead to simplify the analysis. Figure. 1.13 shows a schematic of the computational domain, in which the initially calm water surface is covered with a level ice sheet that is separated by open water of constant width w in the middle of the domain forming a channel. The ship travels straight ahead at a constant speed U in the middle of the open water between the floating ice sheets. The rectangular ice sheet of uniform thickness h is either treated as rigid or flexible and the fracture is neglected. Only half of the domain is discretized with the use of *symmetry* plane through the centerline. Details of the setup are presented in Chapter II.

The thesis is orginized as: following the introduction to the problem and literature review in this chapter, Chapter II describes the numerical solvers and simulation setup that are applied in this work, including the CFD solver for modeling the fluid domain, the equation of a thin elastic plate for governing the ice behavior, and the FSI solver for coupling the fluid and structural domain solutions.

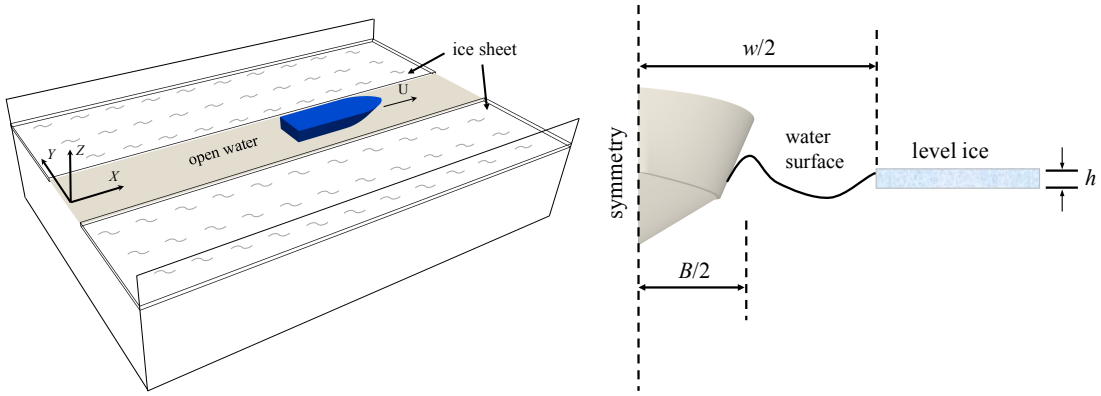

Figure 1.13: Computational domain of the open-water ice channel.

Chapter III uses theories from wave pattern analysis and the multi-hull model from Tuck and Lazauskas (1998) and Faltinsen (2005) to analyze a single ship travel in a deep-water canal. The changes of the wave resistance relative to that in open water are analyzed with respect to the ship speed and canal width. The analysis is used to distinguish between the transverse and diverging waves that contribute most significantly to the alteration of the wave resistance. The contributions due to transverse and divergent waves are validated by towing-tank tests conducted by a student team.

Chapter IV investigates the problem of ship transit in a lead between rigid ice sheets. It first discusses the typical ice thicknesses in the Arctic region and utilizes the knowledge of the relationship between ice flexure and critical speed to justify the rigid-ice assumption for the investigated ice thicknesses. The CFD solver is validated by comparing open-water simulations with existing experiments and is then used to study the same idealized canal from Chapter III of constant width. The relation between the theoretical analysis and the CFD of a full-scale combatant ship in a canal is made such that the wave pattern analysis from the theoretical model can be used to elucidate operation in lead with finite-thickness ice sheets. The analysis is extended to rigid ice sheets of finite thicknesses, where the effects of the ship speed and ice thickness on the ship resistance and wave fields are discussed in the speed

range of $0.2 < Fr < 0.4$. The vertical distribution of momentum flux in the lateral direction is analyzed to strengthen the hypothesis on the effects of ice thickness. Wave resistance and ship motions of a planing hull model traveling in the speed range of $0.4 < Fr < 1.4$ are also discussed in this chapter. Chapter III and IV are expanded upon the author's pulished research (Zhang and Maki, 2023; Maki et al., 2022) with the inclusion of complete case studies and analysis.

Chapter V extends the study to ship transit in open water between thin and flexible ice sheets, where the full-scale combatant ship travels in the speed range of $0.2 < Fr < 0.4$ between ice sheets that are 0.5, 1 or 2-meter thick. The sheet is modeled as a thin elastic plate and the wave-ice interactions are solved with an FSI solver. The chapter begins with a group of convergence studies to determine the appropriate ice dimensions, finite element resolution and number of mode shapes for the modal decomposition. Then the wave patterns are discussed along with the ice deflections, where special attention is paid to the maximum deflection to identify the critical speed. Overwash on top of the ice sheet is a significant phenomenon and is supposed to influence the ice behaviors. The mass flux of overwash is compared for different ship speeds and ice thicknesses.

Finally, Chapter VI concludes the dissertation, discusses its implications and limitations, and provides suggestions for future work.

CHAPTER II

Numerical Methods

This chapter introduces the numerical methods applied in this work. The first section presents the CFD solver for modeling the fluid domain, where both the water and air are solved and their mutual interface is captured by the volume-of-fluid (VOF) method. Ship motions are handled by a six degree-of-freedom (6DOF) library that can solve both prescribed and predicted motions and the corresponding mesh deformation. The second section introduces the fluid-structure interaction (FSI) solver that models the interactions between the flexible ice sheets and ship-generated waves. The ice sheet is modeled as a thin-elastic plate and the deformation is solved by a linear dynamic modal decomposition method.

2.1 CFD Simulations

The unsteady Reynolds-averaged NavierStokes (URANS) equations are solved with the volume-of-fluid method for the air-water flow around the ship hull moving through water that is formed by two ice sheets on either side. This section introduces the computational domain, boundary conditions, governing equations, numerical schemes, hull geometries of the two ship models used in this work, and the corresponding spatial discretization.

2.1.1 Computational Domain and Boundary Conditions

Two coordinate systems used in this work are demonstrated in Figure 2.1. At $t = 0$, the earth-fixed coordinate system $\vec{X} = (X, Y, Z)$ coincides with the translating coordinate system $\vec{x} = (x, y, z)$. The translating coordinate system is fixed to the translation of the ship in the X-direction, i.e. $\vec{x} = \vec{X} - \int_0^t \mathbf{u} dt$, where $\mathbf{u}$ is the ship velocity vector. The translating coordinate system $\vec{x} = (x, y, z)$ is distinguished from the frequently-used ship-fixed coordinate system, which both translates and rotates with the ship motions.

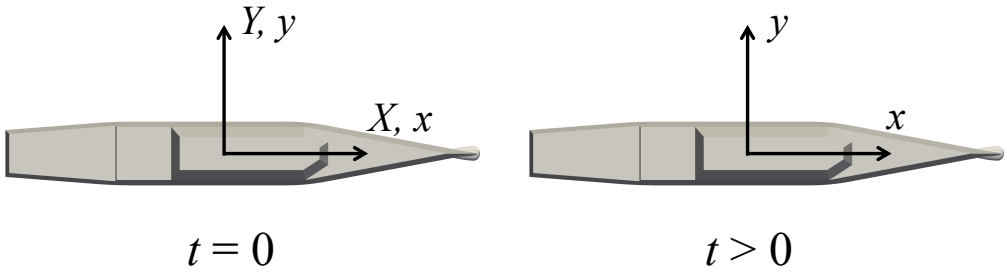

Figure 2.1: The earth-fixed coordinate system $\vec{X} = (X, Y, Z)$ and the translating coordinate system $\vec{x} = (x, y, z)$ that translates with the ship. The origins are at the center of gravity (COG) of the ship. The vertical components Z and z are not displayed, which are positive upward.

Figure 2.2 shows the schematic of the computational domain for a ship transiting in an open-water ice channel in the translating coordinate system. The initially calm water surface is covered with a level ice sheet that is separated by open water (lead) of constant width w in the middle of the domain forming a channel. The ship moves at a constant speed U along the center of the channel and is allowed to heave and pitch. B is the ship beam and is always smaller than w, which means no direct ship-ice interaction occurs in this work.

The computational domain has a length of $7L$ with the ship centered at a distance of $3L$ from the upstream boundary. The half domain width, which is the combination of $w/2$ and the width of the ice sheet, has a large value of $16B$ to minimize the wave

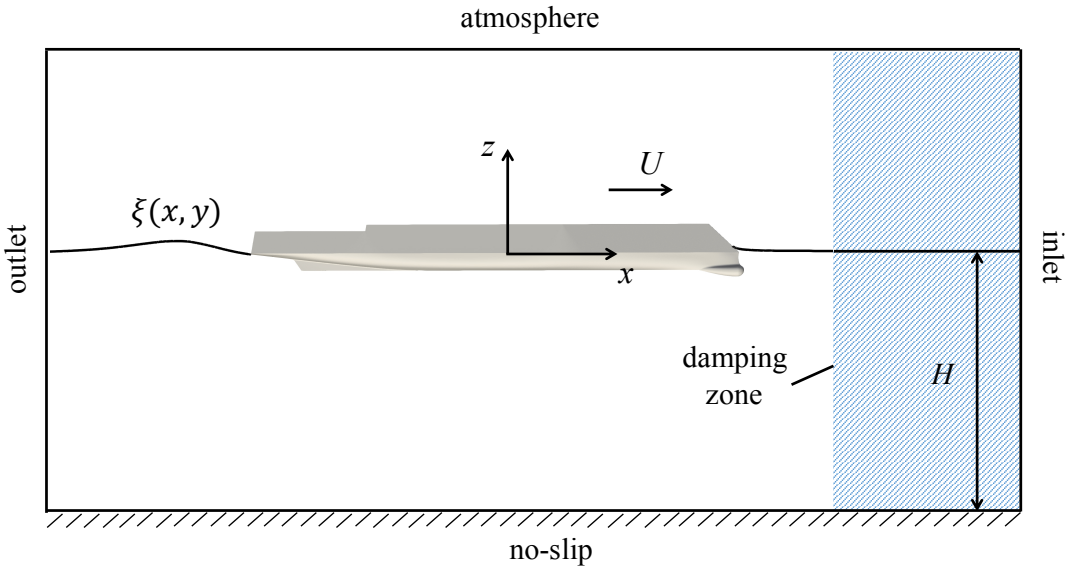

(a) longitudinal plane

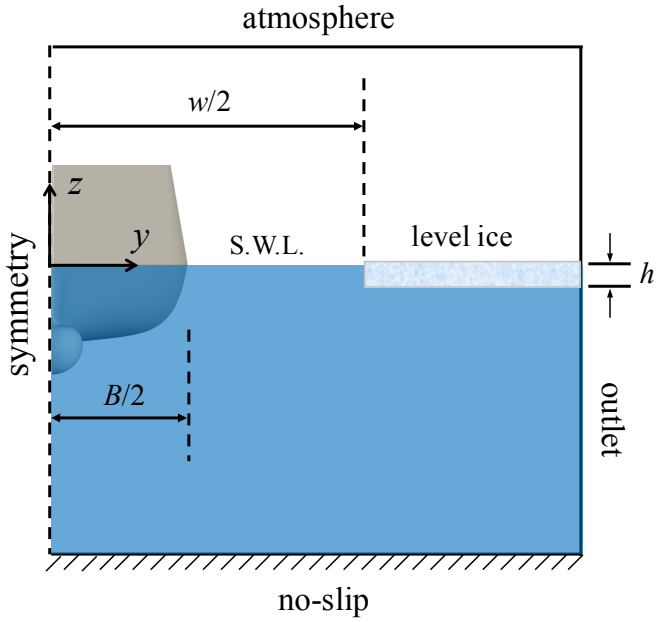

(b) transverse plane

Figure 2.2: Schematic of the computational domain and boundary conditions (not to scale). S.W.L. is the still water level.

reflection from the side wall and to make the domain effectively infinite. The domain dimensions are determined by a group of convergence studies on domain extensions. H is the water depth and has a value that is several times the ship length, which corresponds to a deep water condition $F_d = U/\sqrt{gH} < 0.4$ (Faltinsen, 2005; Sorensen, 2017). The draft of the ice is determined by the densities of water and ice, $\rho_w = 1025$ kg/m^3 and $\rho_{\text{ice}} = 917$ kg/m^3, which means about 10% of the ice is above the calm water plane.

Fluid flows, ship motions (only surge, heave and pitch are allowed), and ice behaviors are all assumed to be symmetric about the centerline of the channel. Therefore, only half of the domain is discretized with the use of *symmetry plane* as the boundary condition (BC) along the centerline. An *inletOutlet* BC is set for the upper boundary to mimic the atmosphere and a no-slip BC is used for the bottom. The surfaces of the hull and ice sheet are treated as solid walls. No-slip boundary conditions are assumed, i.e. the fluid velocity is $\mathbf{u} = \mathbf{U}_{\text{ship}}$ at the hull surface and $\mathbf{u} = 0$ at all surfaces of the ice sheet. A *zero-gradient* BC is applied for the side wall and the downstream boundaries to let ship-generated waves go through, which includes a *zero-gradient* condition for the velocity and volume fraction, and a fixed pressure of zero. The inlet boundary is assigned with *waveAlpha* and *waveVelocity* BCs that are defined in the *waves2Foam* solver (version v1812) for wave generations, but no waves or inflow are prescribed in this work as the ship is set to move in stationary water. A wave damping zone is implemented in the upstream to absorb the waves that travel upstream, which are generated during the speed ramp-up process, such that these waves will not be reflected by the inlet boundary and contaminate the internal ship-wave-ice system. The numerical damping zone has a length of L and has a relaxation function as a wave outlet in Jacobsen et al. (2012)

$$\alpha_r(\chi_r) = 1 - \frac{e^{{\chi_r}^n} - 1}{e - 1} \quad \text{for} \quad \chi_r \in [0, 1] \tag{2.1}$$

α_r is the factor controls the variation of physical quantaties and inside the damping zone

$$\phi = \alpha_r \phi_{\text{computed}} + (1 - \alpha_r)\phi_{\text{target}}, \tag{2.2}$$

where ϕ represents the transported quantities and is either the velocity or volume fraction of water in this study, ϕ_{computed} is the computed value which usually contains pressure disturbance and ϕ_{target} is set as calm water condition. χ_r is the translating coordinate inside the damping zone and is 0 at the start (left of damping zone) and 1 at the end (right of damping zone, which is also the inlet position). The exponent n controls the shape of the transition and a default value of 3.5 is used.

The ship and the entire fluid domain move with the ship velocity relative to stationary water. The ship is first accelerated through a smooth curve to a desired speed U with an average acceleration of $0.1g$, and then travels at the constant speed, and the entire computational domain moves on the ship course at the same speed. The acceleration process is important for the wave fields to reach a steady state. A smooth speed ramp-up can help reach the steady state more quickly. A cosine function is used for the speed ramp-up in this work

$$U_{\text{ship}} = \frac{1}{2}\left[U - \cos(\frac{t}{t_r}\pi)\right], \tag{2.3}$$

where $t_r = U/0.1g$ is the ramp-up time. This cosine function and its derivative, which is the acceleration, are both continuous and differentiable for $t > 0$.

2.1.2 Numerical Solver and Governing Equations

The wave field and resistance are found by numerical solution of the unsteady RANS (URANS) equations of an incompressible two-phase fluid

$$\nabla \cdot \mathbf{u} = 0, \tag{2.4}$$

$$\frac{\partial \rho \mathbf{u}}{\partial t} + \nabla \cdot (\rho \mathbf{u}\mathbf{u}) = -\nabla p_{\text{rgh}} - \mathbf{g} \cdot \mathbf{x} \nabla \rho + \nabla \cdot \left[\mu_{\text{eff}} (\nabla \mathbf{u} + \nabla \mathbf{u}^T) \right], \tag{2.5}$$

where $\mathbf{u}$ is the flow velocity, ρ is the fluid density, $\mu_{\text{eff}} = \mu + \mu_t$ is the effective dynamic viscosity, $\mathbf{g}$ is the gravity vector, and p_{rgh} is the hydrodynamic pressure that deviates from the hydrostatic part. The turbulent viscosity μ_t is solved as a function of the turbulence model and is evaluated by the one-equation Spalart-Allmaras turbulence model (Spalart and Allmaras, 1992). Both full-scale and model-scale ship models are analyzed in this work and high Reynolds numbers are expected. Having fully resolved turbulent boundary layers is not practical considering the computational cost. Spalding's wall function (Spalding, 1961) is applied to predict the friction velocity.

The moving air-water interface is captured using the volume-of-fluid (VOF) approach, in which an artificial compression term is added to maintain a sharp fluid interface,

$$\frac{\partial \alpha}{\partial t} + \nabla \cdot (\mathbf{u}\alpha) + \nabla \cdot [\mathbf{u}_r \alpha (1 - \alpha)] = 0. \tag{2.6}$$

Water and air are distinguished by the indicator function $\alpha(\mathbf{x}, t)$,

$$\alpha(\mathbf{x}, t) = \begin{cases} 1 & \text{water} \\ 0 & \text{air} \\ 0 < \alpha < 1 & \text{interface.} \end{cases} \tag{2.7}$$

In the one-fluid model, it is assumed that the intrinsic fluid properties, such as density and viscosity, are updated based on the VOF function as,

$$\rho = \rho_1 \alpha + \rho_2 (1 - \alpha) \quad \text{and} \quad \mu = \mu_1 \alpha + \mu_2 (1 - \alpha) \tag{2.8}$$

where $\rho_1 = 998.8$ kg/m^3 and $\rho_2 = 1$ kg/m^3 are the densities, μ_1 and μ_2 are the dynamic viscosity coefficients of water and air respectively. The URANS and VOF equations are solved on a finite-volume discretization of the flow domain with a cus-

tomized flow solver based on the OpenFOAM open-source CFD library.

A finite-volume cell-centered discretization is applied for arbitrary grid topologies as described in Jasak (1996). The base OpenFOAM toolbox provides a variety of numerical schemes for solving the discretized equations. Second-order spatial discretization schemes are used together with the first-order implicit Euler scheme for time advancing and the varying time step size is determined by limiting the Courant number

$$C = \frac{u\Delta t}{\Delta x} \leq C_{\max}, \tag{2.9}$$

and $C_{\max}$ is set as 3, where the real time step sizes after the simulations reach a steady state fall in the approximate range of $0.002 \text{ s} < \Delta t < 0.005 \text{ s}$, depending on the ship speed. The convection term is treated with a second-order linear upwind scheme to preserve numerical stability while retaining the nominal second-order accuracy. A non-orthogonal correction coefficient of 0.5 is specified to add non-orthogonal correction to the orthogonal component to maintain solution accuracy on a non-regular mesh with skewed cells. The cell-limited scheme is applied on the velocity gradient to enforce boundedness in face interpolations. A second-order central difference method is applied to discretize the diffusion term. The volume-fraction divergence term is discretized using the vanLeer scheme to maintain its boundedness. The VOF equation is solved with the multidimensional universal limiter for explicit solution (MULES) method. The Pressure-Implicit Split-Operator (PISO) algorithm is used for the velocity and pressure coupling.

2.1.3 Ship Models and Spatial Discretization

Two frequently-used ship models are adopted in this work, which are the full-scale Office of Naval Research Tumblehome (ONRT) and a model-scale Generic Prismatic Planing Hull (GPPH). The hull geometry, general characteristics and spatial dis-

cretization are introduced in the following.

The ONRT ship model is a preliminary design of a modern surface combatant, which is publically accessible for fundamental research. A schematic of the ship model is shown in Figure 2.3. Only the bare hull with the front bulb is included in this work, appendages including skeg, bilge keels, shafts, struts, rudders and most of the superstructure are removed to reduce complexity of the hull geometry and corresponding mesh size. The general characteristics for the full-scale model are collected in Table 2.1.

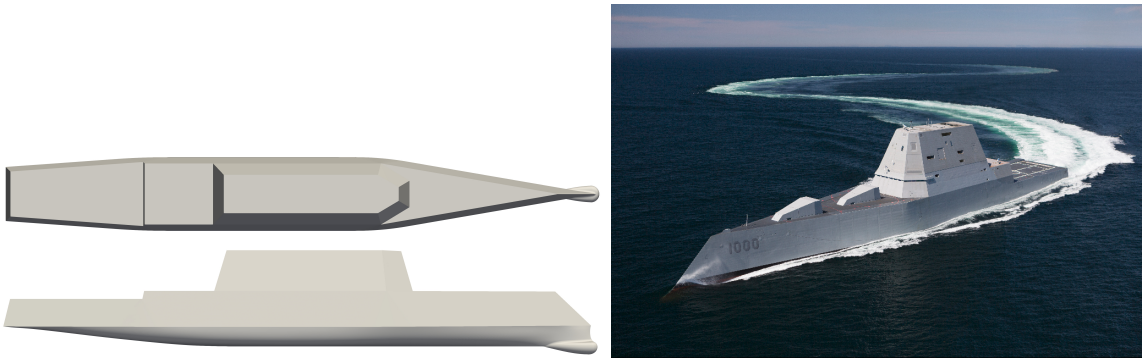

Figure 2.3: Left is a schematic of the ONRT model. Right is a photo of a the USS Zumwalt (DDG-1000).

Table 2.1: Characteristics for full scale ONRT ship model.

Length overall, m (ft)	154 (505)
Max. beam, m (ft)	18.78 (61.6)
Draft, m (ft)	5.494 (18.02)
Displacement, ton	8,507
Block coefficient	0.535
Pitch gyradius (k_{yy}), m (ft)	38.5 (126.3)
Zero speed trim	0°
Wetted surface, m^2	3,237

The GPPH model was designed as a publicly releasable hull and was chosen to be representative of typical planing hulls while minimizing geometric variables. This design allows for geometry of reduced complexity as an initial test case for CFD

predictions (Lee et al., 2017). A model scale of the GPPH with a scale factor of 10.7 and a length of 1.22 m (4.0 ft) is chosen for this study. Figure 2.4 shows a schematic of the hull model and Table 2.2 shows the general characteristics of the model scale GPPH.

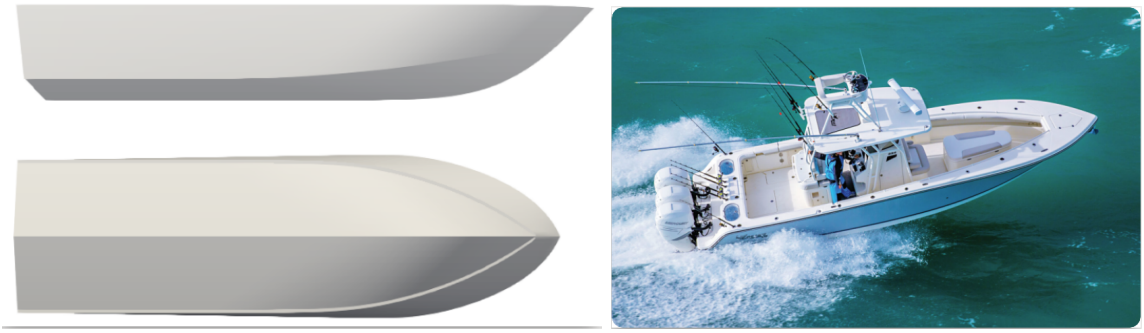

Figure 2.4: Left is a schematic of the GPPH model. Right is a photo of a planing boat.

The fluid domain is discretized with an unstructured grid composed of finite volumes that are dominantly hexahedral, which is generated by the mesh generator *snappyHexMesh*. An example of a coarse grid is demonstrated in Figure 2.5. The grid is uniform around the ship and is stretched towards the boundaries to reduce the total number of elements. Local refinement is applied near important features including the hull and free surface (though is not displayed in the figure). Boundary layers are also used for the hull surface to further reduce the y^+, where an average value of $y^+ \approx 10$ is achieved in this work.

Table 2.2: Characteristics for the model scale GPPH (10.7:1).

Length overall, m (ft)	1.22 (4.0)
Max. beam, m (ft)	0.37 (1.2)
Draft, m (ft)	0.072 (0.236)
Displacement, kg (lbs)	12.66 (27.85)
LCG (forward of transom), m (ft)	0.43 (1.41)
VCG (from keel), m (ft)	0.137 (0.449)
Pitch gyradius (k_{yy}), m (ft)	0.2713 (0.89)
Zero speed trim	0°

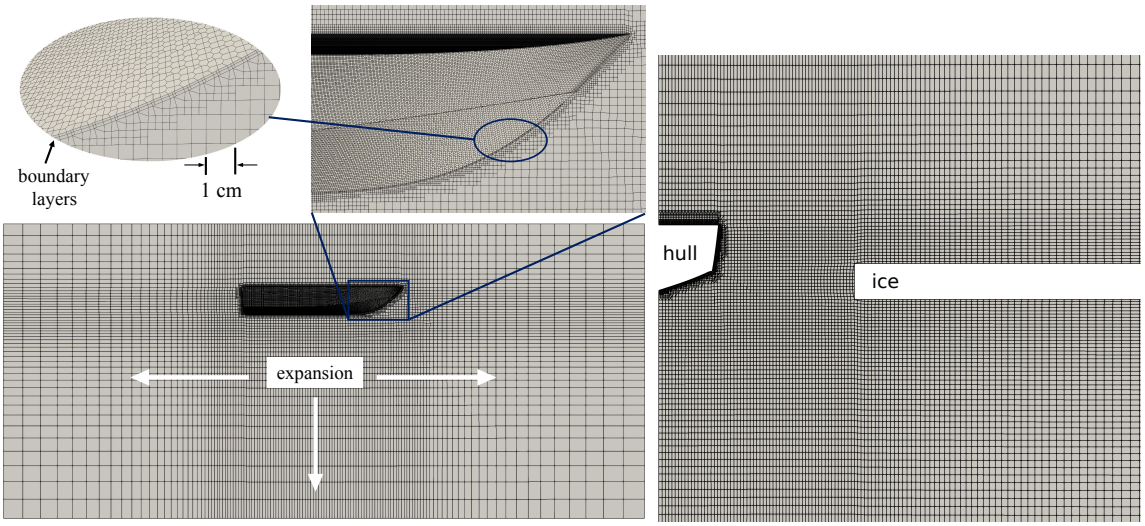

Figure 2.5: Slices through the mesh, the left is through the symmetry plane and the right is cut transversely through the midship.

2.1.4 Ship Motions and Mesh Deformation

Besides the forward motion, both ship models are allowed to heave and pitch, where the associated ship motions are handled by a six degrees-of-freedom (6DOF) library that is tightly coupled with the fluid solver. A deformable mesh technique is applied to enable mesh deformation around the hull surface due to the heave and pitch, while maintaining the mesh structure away from the hull.

The ship motions as well as the motions of the body-fitted meshes can be divided into two parts. The first part is the prescribed translations, which in this case is the ahead movement in the surge direction. The computation domain and mesh are frozen to this movement, i.e. they translate synchronously with the ship at the same forward speed. The second part is the heave and pitch movement, which are within the X-Z plane. These motions are separated from the domain movement, i.e. the computational domain does not heave or pitch with the ship. This is because the ice is also defined as a domain boundary, such domain movements will cause deviation of the ice from its equilibrium position. The heave and pitch movements can only cause local mesh deformation within a distance from the hull surface. Figure 2.6 depicts an

example of such ship motions and resulting mesh deformation.

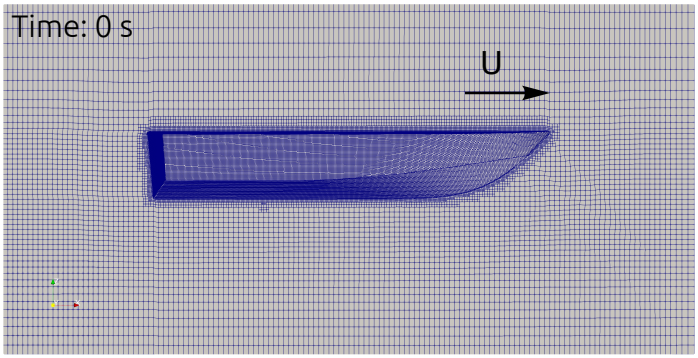

(a) undeformed mesh

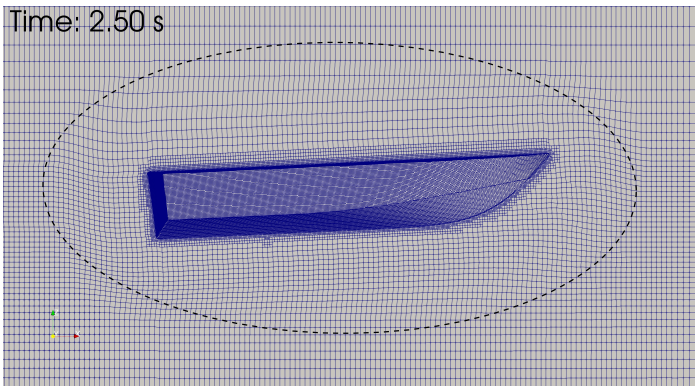

(b) mesh deformation with heave and pitch movement

Figure 2.6: Illustration of ship motions and associated mesh deformation. The dashed oval represents the outer boundary for mesh deformation (shape and position are not exact).

For a body-fitted mesh, mesh morphing is required to retain the grid connectivity (no topological changes to mesh) when solid-body motions are involved. The spherical linear interpolation (Slerp) algorithm is implemented in the *rigidBodyMotion* library in OpenFOAM to calculate the mesh displacement based on the distance of a cell to the moving body, where mesh deformation is only allowed between the user-specified *inner* and *outer* distance. Such a mesh morphing technique can preserve the mesh topology and smoothness and retain the overall mesh quality in dealing with moderate solid-body motions. Figure 2.6b gives an example of mesh morphing with the Slerp algorithm used in one of the simulations with the planing hull. More detailed examples

can be found in Windt et al. (2020).

An appropriate *outer* distance needs to be specified for the mesh morphing. Large ship motions can destroy the mesh if the distance is too small. The *outer* sphere should not reach too far as parts of domain boundaries or other geometries will be deformed if they are within the distance. As the ice surface is defined as a domain boundary and the space between the hull surface and ice edge can be limited in narrow-channel scenarios, e.g. the gap can be as little as 10% of ship beam in the case of $w/B = 1.1$. On the other hand, since only heave and pitch are allowed, the ship motions and associated mesh deformation happen mostly within the X-Z plane but are limited in the Y-direction. An outer distance of $0.5B$ is specified in this study, and both the inner and outer distances are scaled in the Y-direction by a factor depending on how narrow the channel is, such that it does not interfere with the ice edge and leaves sufficient space for ship motions.

The customized changes for separating the mesh motions and enabling directional scaling have been made to the *rigidBodyMotion* function in the *rigidbodycshl* library.

2.2 Fluid-Structure Interaction Solver

For the problem of ship transit between flexible ice sheets, the fluid-structure interaction (FSI) solver, which is first developed by Piro and Maki (2013) and Piro (2013) and further expanded in Mesa (2018); Mesa et al. (2022), is used to model the interactions between the ship-generated waves and ice sheets. Modifications are made to accommodate the mapping between the moving fluid domain and static structural domain, and the inclusion of the fluid stress due to overwash water. This section introduces the computational domain, simulation setups, the fluid and structural domain solutions, and the coupling between them.

2.2.1 Computational Domain

A schematic of the computational domain, which consists of a static structural domain and a moving fluid domain, is shown in Figure 2.7. The structural domain, which is a continuous and rectangular ice sheet of constant thickness, is fixed in a lateral position and has a much larger extension than the fluid domain. The same fluid domain described in Section 2.1.1 moves with the ship at the ship speed U relative to stationary water. The structure and fluid domains overlap at the ice surfaces within the perimeter of the fluid domain. The mutual interfaces include the upper and lower surfaces of the ice sheet, which are initially horizontal and parallel to each other, as well as the vertical ice edge. The upper surface of the ice sheet is included mainly for resolving the overwash effects.

The ice sheet is subject to external forces from the fluid domain and deforms vertically under such forces, where the deformations satisfy the equations of a thin-elastic-plate model and are solved with a modal decomposition method (Piro and Maki, 2013; Mesa, 2018). The external forces include the hydrodynamic and hydrostatic forces exerting on the lower surface of the ice, and the force on the upper surface of the ice due to overwash. The force due to overwash consists mainly of the fluid weight of the green water. The hydrostatic pressure $\rho g z$ is acting on the entire lower surface of the ice sheet that extends beyond the fluid domain, and is determined by the elevation z of the deflected lower surface (which varies across the ice surface). The hydrodynamic pressure p_{rgh} is only evaluated within the fluid domain with the assumption that the hydrodynamic pressure is only important within the fluid domain. With such assumption, a sufficiently large fluid domain is needed to ensure the hydrodynamic pressure outside the fluid domain is small enough to be neglected. In this work, the downstream length of the domain is determined such that the hydrodynamic pressure outside the fluid domain is smaller than 10% of the initial hydrostatic pressure, i.e. $p_{\text{rgh}} < 0.1 \rho g h_{\text{sub}}$ and $h_{\text{sub}} = 0.9\ h$. Although 10% of

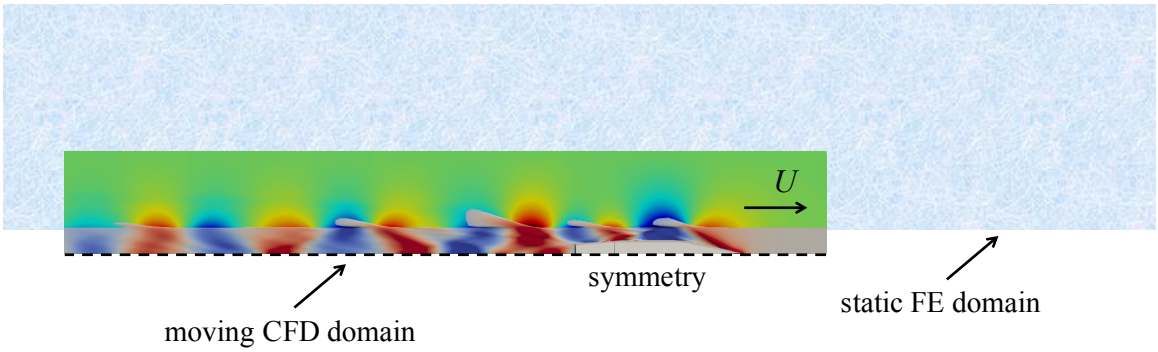

(a) Top view of the computational domain. The overlap between the two domains is colored by the hydrodynamic pressure over the lower surface of the ice.

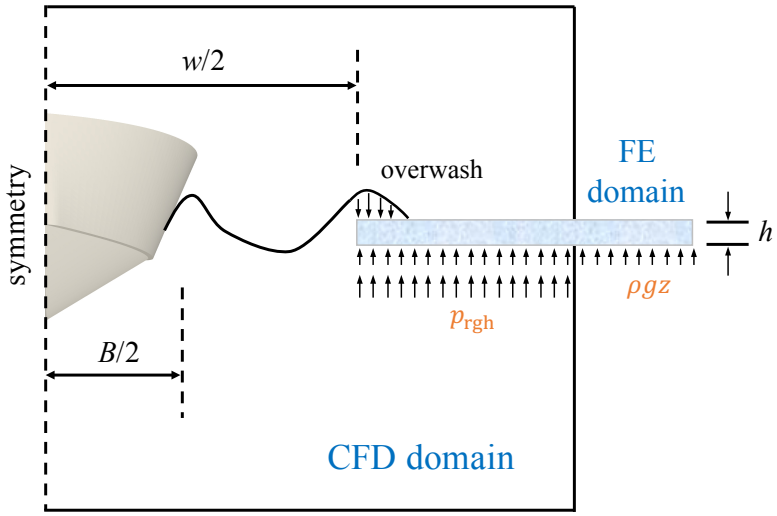

(b) Transverse slice of the computational domain. The ice sheet is subject to the hydrodynamic pressure p_{rgh} and hydrostatic pressure ρgz on the lower surface of the ice, and the pressure on the top of the ice due to overwash.

Figure 2.7: Schematic of the computational domain for the FSI problem (not to scale).

the hydrostatic pressure can be non-negligible, the truncated hydrodynamic pressure field in the downstream outside of the fluid domain is far enough from the hull ($> 5\ L$) so its impact on the near-field ice reponses is limited. The width of the fluid domain is 10 B, beyond which the hydrodynamic pressure is mostly smaller than 1% of the initial hydrostatic pressure, i.e. $p_{\text{rgh}} < 0.01\rho g h_{\text{sub}}$, as the hydrodynamic pressure declines quickly in the transverse direction. The hydroforces exerting on the vertical ice edge are not included as external forces for the structural domain as the ice sheet is

fixed in the lateral position and the normal stress on the ice edge will not contribute to rigid-body motions of the ice. Although the shear stresses on the vertical ice edge can possibly affect the vertical deflections but are neglected as they are sufficiently small. Different than that in the rigid ice simulations, the flexible ice sheet is allowed to move freely in the vertical direction and the movement is driven by the vertical net force on the ice. The weight of the ice is included as an internal force and is accounted for in the form of surface pressure ($p_{\text{ice}} = -\rho_{\text{ice}} g h$) over the ice sheet. The weight is initially balanced by the buoyancy due to the hydrostatic pressure $\rho g h_{\text{sub}}$, which results in the aforementioned equilibrium position in undisturbed water, $z = -0.9\ h$.

2.2.2 Fluid Domain Solution

The two-phase flower solver introduced in Section 2.1.2 is used to model the incompressible fluid that is governed by the unsteady Navier-Stokes equations

$$\nabla \cdot \mathbf{u} = 0, \tag{2.10}$$

$$\frac{\partial \rho \mathbf{u}}{\partial t} + \nabla \cdot (\rho \mathbf{u}\mathbf{u}) = -\nabla p_{\text{rgh}} - \mathbf{g} \cdot \mathbf{x} \nabla \rho + \nabla \cdot \left[\mu (\nabla \mathbf{u} + \nabla \mathbf{u}^T) \right], \tag{2.11}$$

but laminar flow is assumed for the flexible-ice problem.

2.2.3 Structural Domain Solution

The flexible ice sheet is a continuous rectangle of uniform thickness h and is modeled as a thin elastic plate. The key property of flexure is included, but rigid-body motions are not allowed for the ice sheet except for the vertical translation. Amplitudes of the gravity waves traveling in the ice are assumed to be small relative to the wavelength, such that linearity can be assumed.

2.2.3.1 The Thin-Elastic-Plate Model

The ice is assumed to be homogeneous and the ice sheet is modeled as a thin elastic plate. The Kirchhoff hypothesis is adopted such that a two-dimensional shell through the mid-surface plane can be used to represent the three-dimensional plate (Section 3.2 in Reddy (2006)). The following kinematic assumptions are made for the ice sheet:

- The transverse normals (i.e. straight lines perpendicular to the mid-surface) remain straight after deformation.
- The transverse normals remain normal to the mid-surface after deformation.
- The transverse normals cannot be elongated, i.e. the thickness of the plate does not change during deformation.

The deflection of the ice plate $w(x, y, t)$ satisfies the equation of a thin elastic plate

$$\rho_i h w_{tt} + D\nabla^4 w = p(x, y, z, t), \tag{2.12}$$

where $\rho_i = 917$ kg/m^3 is the ice density, h is the ice thickness, $D = Eh^3/12/(1+\nu^2)$ is the ice rigidity, $E = 4.2$ GPa (Shishmarev et al., 2019; Ren et al., 2020; Zeng et al., 2021) is Young's modulus of ice and $\nu = 0.303$ is the Poisson's ratio, $\nabla^4 = \partial^4/\partial x^4 + 2\partial^4/(\partial x^2 \partial y^2) + \partial^4/\partial y^4$ is a biharmonic operator, and $p(x, y, z, t)$ is the sum of the external fluid pressure that includes the hydrodynamic and hydrostatic pressure and the pressure due to overwash, and its own weight.

2.2.3.2 Modal Decomposition

The ice sheet is modeled using a finite number of mode shapes with associated natural frequencies. The modal theory is based upon linear superposition and the orthogonality of the mode shapes allows for the decoupling of the structural equations of

motion

$$[I]\{\ddot{q}\} + [2\zeta\omega_n]\{\dot{q}\} + [\omega_n^2]\{q\} = \{f\}, \tag{2.13}$$

where $[I]$ is the identity matrix, $[\omega_n^2]$ is a diagonal matrix of the natural frequencies, $[2\zeta\omega_n]$ is the modal viscous damping matrix which assumes proportional damping, $\{q\}$ is the vector of modal amplitudes, and $\{f\}$ is the vector of modal forces. The main advantage of using a modal model to describe the structure is that only a limited number of degrees-of-freedom are necessary to solve and accurately represent the response of the structure. A convergence study is provided in Sec. V to demonstrate the dependence of the ice responses on number of modes, which shows that 800 modes are sufficient to represent the ice sheet so the deflections and stresses can be accurately resolved.

A finite-element method is used to generate the mode shapes and frequencies based on the dimensions of the ice sheet and other mechanical properties of the ice. The commercial software for finite element analysis, Abaqus (version 2022), is used. The ice plate is discretized into elements that connect nodes. Each node contains six degrees of freedom including three translations and three rotations. The displacements at each node are interpolated with cubic shape functions, and the rotations with quadratic shape functions. The high-order interpolations bring solutions of high accuracy for displacement and rotations within the elements. Therefore, fewer finite elements are needed to accurately represent the structural domain. No constraining conditions are applied to the nodes of the ice plate, which is instead balanced by the buoyancy and its own weight.

2.2.4 Coupling of Fluid and Structural Domains

2.2.4.1 Grid Matching and Data Exchange

The fluid domain moves at the ship speed and overlaps with the static structural domain at the mutual interface, where the interactions between the ship-generated waves and ice sheet occur. The mutual interface includes the upper and lower surfaces of the ice sheet as well as the vertical ice edge. Since the structural domain features a two-dimensional shell and the hydroforces exerted on the vertical ice edge are not input as external forces for the structural domain, data exchange between the two domains only occurs on the upper and lower surfaces of the ice sheet.

At each time step, the fluid domain moves forward to a new position. Grid matching between the fluid faces and structure elements on the mutual interface is required at each time step to facilitate data exchange. The adopted 'projection method' (Maman and Farhat, 1995; Farhat et al., 1998) for grid matching does not require identical discretization of the fluid and structural domains on the mutual interface. Owing to the high-order interpolations within the FE domain and nature of the FE solution, the structure can be accurately resolved with larger elements than which are necessary for the fluid domain, therefore finer grids are used for the CFD than the FEM on the mutual interface.

A schematic that illustrates the grid matching between the two domains is shown in Figure 2.8. Quadrilateral grids, mostly squares and rectangles, are used for the discretization of both the finite elements and fluid domain on the mutual interface. Finite elements that overlap at least one face center of fluid mesh are marked as *wet elements*, which are colored green in Figure 2.8a. Each wet element has an array of 3×3 Gauss integration points (plotted in a dry element in the figure for illustration) that are used to evaluate the fluid stress acting on the structure element, where the coordinates of the Gauss points and integration weights are determined by the

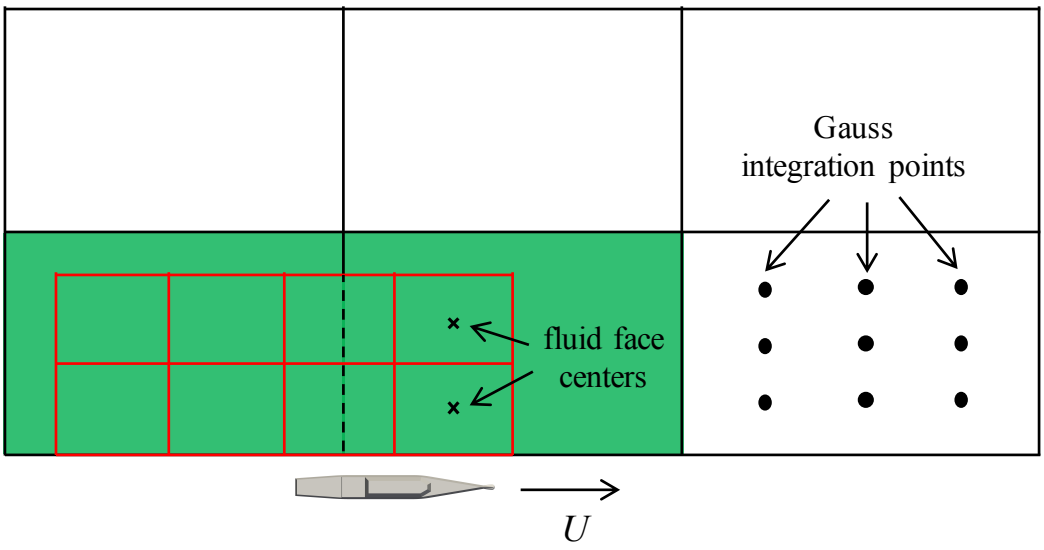

(a) Top view of the computational domain.

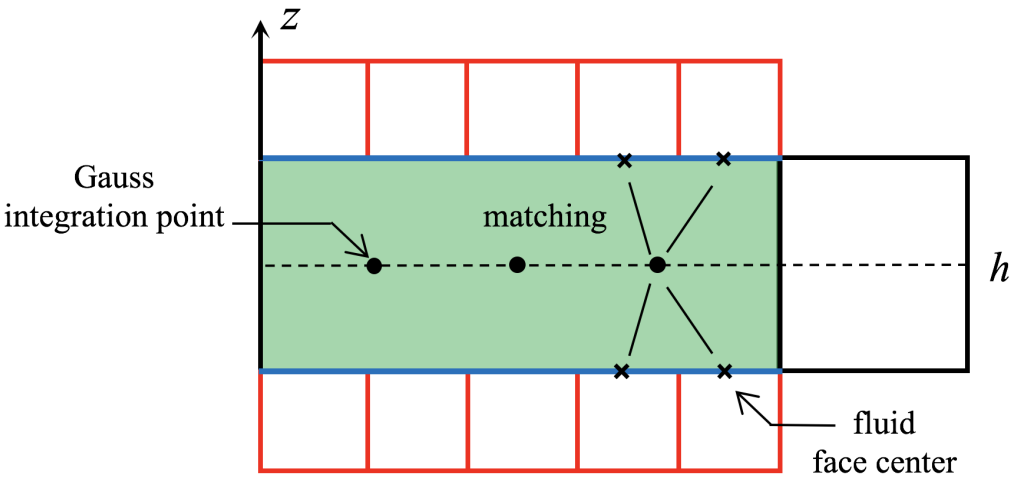

(b) Transverse slice through the fluid and structural grids. The mid-surface of the finite elements is indicated by the dashed line. The two mutual interfaces are marked by the solid blue lines.

Figure 2.8: Illustration of matching between fluid and structure grids (not to scale). Black grids are the static structure elements, red grids represent the moving fluid mesh, and green rectangles mark the wet finite elements that match the fluid domain.

Gaussian quadrature rule. The fluid stress at each Gauss integration point is found by taking a distance-weighted average of the fluid pressure at the four fluid faces that are the closest to the Gauss point. Different from that in Piro and Maki (2013), for the current problem, each wet element matches fluid faces from two independent surfaces,

which are the upper and lower ice surfaces. Therefore, the two layers of fluid face centers are first collapsed onto one single layer by leaving out the vertical coordinates, then the two closest fluid faces on each layer are found for each Gauss point by sorting the distances. Because the two parallel surfaces have almost identical discretization, the matched fluid faces are supposed to be nearly symmetric about the mid-surface. The fluid stresses on the two surface layers are added in the form of force vectors to take into account the normals of the two interfaces. Only the pressure component of the fluid stress is considered, whereas the viscous component is neglected. An illustration of the matching between a Gauss point and four fluid faces is plotted in Figure 2.8b.

The fluid domain also requires information about structural velocity and displacement. The velocity and displacement of the fluid boundary at the fluid face centers along the mutual interface are found using the structural-element shape function. The deformable structure surfaces are treated as outer boundaries in the fluid domain, where the mesh deformation is handled by the OpenFOAM library. Two forms of boundary conditions for the fluid-structure interaction analysis are provided in Piro and Maki (2013). With the no-slip BC, both forms have a fluid velocity equal to the structural velocity on the mutual interface

$$\mathbf{u}(\mathbf{x_b}, t) = \mathbf{u_b}(\mathbf{x_b}, t), \tag{2.14}$$

where $\mathbf{u_b}$ is the body velocity and $\mathbf{x_b}$ is the position of the structure. In the first method, the fluid mesh deforms to exactly follow the structural mesh and the exact no-penetration body-boundary condition is satisfied. The second method applies the structural velocity to the fluid boundary on its undeformed position based on the assumption of small structural deformation. The first method with exact mesh deformation is adopted in this work.

2.2.4.2 Under-Relaxation and Iterative Algorithm

The fluid domain solutions and structural responses are tightly coupled and are solved in an iterative manner at each time step. During each iteration, the structural deformation is updated using the fluid stress from the previous iteration. Then, the fluid domain is solved using the updated structural deflections. The selection of under-relaxation strategies and parameters is important so that convergence can be achieved with a minimal number of iterations. The explicit under-relaxation method from Piro and Maki (2013) is employed, which uses the parameter β_r to control the change in the state vector χ at an intermediate iteration as

$$\chi_{i+1}^{n+1} = (1 - \beta_r)\chi_i^{n+1} + \beta_r \tilde{\chi}_{i+1}^{n+1}, \tag{2.15}$$

where $\tilde{\chi}$ is the unrelaxed update, n is the time step, and i is the iteration counter. The selection of the under-relaxation parameter β_r is crucial for the convergence and accuracy of the solutions. Smaller β_r provides more stablility but requires a greater number of iterations to reach convergence, larger β_r converges faster but can lose stability in the iterations. A value of $\beta_r = 0.2$ is applied in this work. More detail on the under-relaxation method and iteration algorithm for the FSI solver can be found in Piro and Maki (2013) and Piro (2013).

2.3 Summary

Numerical methods applied for the problem of ship transit in a lead between either rigid or flexible ice sheets are introduced in this chapter.

The first section presents the CFD solver for modeling the two-phase flows. URANS equations are solved for both the water and air, where the VOF approach is used to capture the moving interface. The computational domain and boundary

conditions, governing equations for the two-phase fluid, and numerical schemes are described in this section. The ONRT and GPPH are selected as the two ship models, the hull geometries and general characteristics of which are given. Ships are allowed to heave and pitch, where the associated ship motions are handled by a 6DOF library. A deformable mesh technique is applied to enable mesh deformation around the hull surface due to the heave and pitch while maintaining the mesh structure away from the hull. Customized changes for separating the mesh motions and enabling directional scaling, which are applied to facilitate the simulations with a moving hull and static ice sheets, are introduced along with the deformable mesh technique.

The second section presents the FSI solver that is adapted from Piro and Maki (2013) and Piro (2013) to model the interactions between the ship-generated waves and flexible ice sheets. The computational domain that consists of a static structural domain and a moving fluid domain is described. The fluid domain is modeled by the same two-phase flow solver in the first section except laminar flow is assumed for the flexible-ice problem. For the structural domain, the ice sheet is modeled as a thin elastic plate with the use of the Kirchhoff hypothesis so that the 3D ice sheet can be modeled by a 2D shell through the mid-surface of the ice sheet. The ice sheet is represented by a finite number of uncoupled mode shapes with associated natural frequencies. Modal decomposition is applied based on linear superposition and orthogonality of the mode shapes such that the structural equations of motion can be decoupled. The commercial software finite element analysis, Abaqus, is used to generate the mode shapes and natural frequencies. Grid matching between the fluid faces and structure elements on the mutual interface is required at each time step to facilitate data exchange. The pressure component of the fluid stress is evaluated at Gauss integration points to compute the fluid pressure over the matched finite element, which is used to update the equations of motion. The structural displacement and velocity are used by the fluid domain as the boundary conditions. The fluid

domain solutions and structural responses are tightly coupled and are solved in an iterative manner at each time step with an under-relaxation strategy to help reach convergence.

CHAPTER III

Ship Moving in a Canal

A ship traveling in a canal, where two side walls extend to the bottom as depicted in Figure 1.3c, has been extensively studied with theoretical methods and is a related problem to that of ship transit near sheet ice. Theoretical methods are more efficient and affordable compared with experiments and CFD simulations. By constructing the relationship between operation in a canal and transit in water bounded by adjacent sheet ice, the knowledge from operation in a canal can be utilized to develop understanding of Arctic transit and provide an efficient tool for rapid estimations of wave resistance. This chapter uses theoretical analysis of the far-field wave patterns to study the wave resistance in deep-water canals.

3.1 Wave Pattern Analysis

3.1.1 Ship Waves in Deep Water

The wave resistance and wave field generated by a ship traveling with constant speed in a canal are studied using linearized potential flow theory. The original work by Michell (1898) represents a ship as a source or sink distribution on the centerplane of a thin hull. Figure 3.1 from Faltinsen (2005) illustrates the source and sink in this theory, where the ship moves the water and it pushes the water out at the bow, which is like a source, whereas the ship attracts water at the stern, which acts

like a sink.

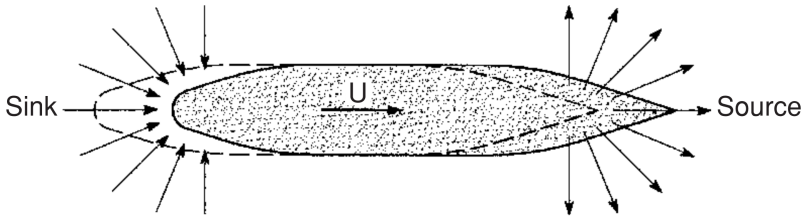

Figure 3.1: Illustration of the source and sink in the theory (Faltinsen, 2005).

The free-surface Green function satisfies linearized free-surface boundary conditions (Faltinsen, 2005)

$$U^2 \frac{\partial^2 G}{\partial x^2} + g \frac{\partial G}{\partial z} = 0 \quad \text{on } z = 0, \tag{3.1}$$

where U is the ship speed, G is the velocity potential due to the source or sink and the strength of the source or sink is proportional to the ship speed and the longitudinal slope of the ship hull. The linearized body boundary condition is accurate in the limit of the beam of the ship being small relative to the length, and is commonly referred to as thin-ship theory (Tuck and Lazauskas, 1998; Faltinsen, 2005).

The singular integro-differential equations in the Michell thin-ship theory can be solved numerically for arbitrary ship geometry, or analytically for simplified geometry. The hull geometry of the ONRT is shown in Figure 3.2. For theoretical analysis herein, the geometry of the ONRT is simplified and represented as a wedge-like shape (Faltinsen, 2005) as shown in Figure 3.3 so that the integrals can be solved analytically.

The idealized ship is defined by the parallel midbody of length L_p and beam B. The wedge-like shape is prismatic in the vertical direction and has draft T. The hull

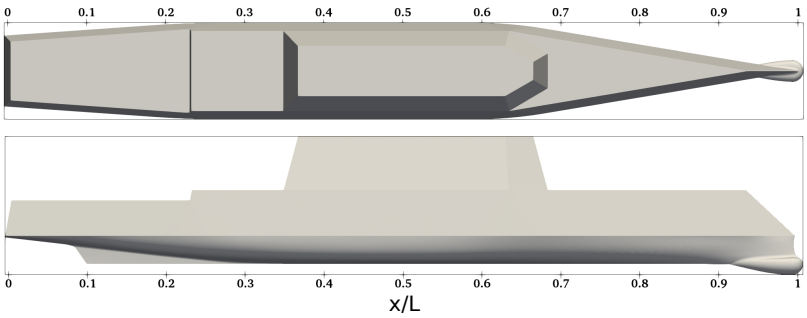

Figure 3.2: Top and side views of the ONRT bare-hull geometry with local longitudinal coordinate x with respect to the ship length L.

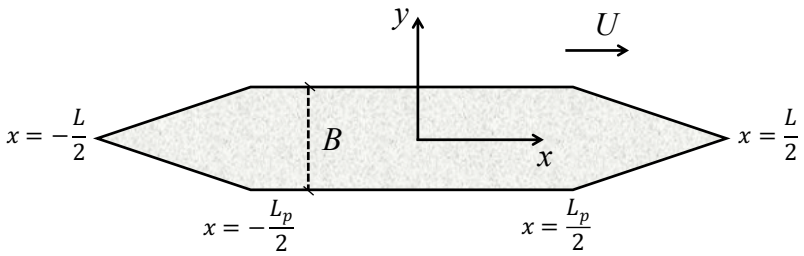

Figure 3.3: Waterplane of the Wigley's wedge-shaped body with draft D.

surface function η has a derivative with respect to x as

$$\eta_x = \begin{cases} \frac{B}{L-L_p} \equiv C & \text{for } x = [-\frac{L}{2}, -\frac{L_p}{2}) \\ 0 & \text{for } x = (-\frac{L_p}{2}, \frac{L_p}{2}) \\ -C & \text{for } x = (\frac{L_p}{2}, \frac{L}{2}]. \end{cases} \tag{3.2}$$

The following values, which are non-dimensionalized with respect to the ship length, are selected for the wedge-shaped body to approximate the ONRT model: $L = 1$, $L_p = 0.5$, and $B = 0.12$. The ship draft is $T = 0.05$.

The ship-generated wave system is defined by the function $z = \xi(x, y)$. For waves that are sufficiently far from the hull the wave field can be calculated by summing up plane waves traveling at various angles relative to the ship track according to Newman

(2018),

$$\xi(x,y) = Re \int_{-\pi/2}^{\pi/2} A(\theta) e^{-ik(\theta)[x\cos\theta + y\sin(\theta)]}\, d\theta, \tag{3.3}$$

where $A(\theta)$ is the amplitude of the wave traveling at angle θ and is a function of the submerged ship shape and speed (see Figure 3.4). For this wedge-shaped body, $A(\theta)$ takes the form (Faltinsen, 2005)

$$A(\theta) = \frac{4C}{\pi i k_0}\left(1 - e^{-k_0 \sec^2\theta D}\right)[\cos(0.5k_0 \sec\theta \cdot L_p) - \cos(0.5k_0 \sec\theta \cdot L)]. \tag{3.4}$$

The wave number $k(\theta) = k_0 \sec^2\theta$ is determined from the dispersion relation for plane waves moving at oblique angle θ with respect to the ship track, and $k_0 = g/U^2$ is the wave number of pure transverse waves that correspond to $\theta = 0$. The waves that travel steadily with the ship occur in the range $0 \leq \theta < \pi/2$. A diagram of a steady wave system is shown in Figure 3.4. The ship-generated waves appear within a triangular region extending behind the ship and the half-angle of this region is called the Kelvin angle. In deep water, the value of the half-angle is approximately 19 deg.

The spectrum of far-field waves in deep water can be decomposed into two sets of waves. The set of transverse waves possess heading angle $0 \leq \theta < \theta_1$, where $\theta_1 = \arcsin(1/\sqrt{3}) \approx 35°16'$, and the remaining waves in the spectrum are called diverging waves that occur in the range $\theta_1 \leq \theta < \pi/2$.

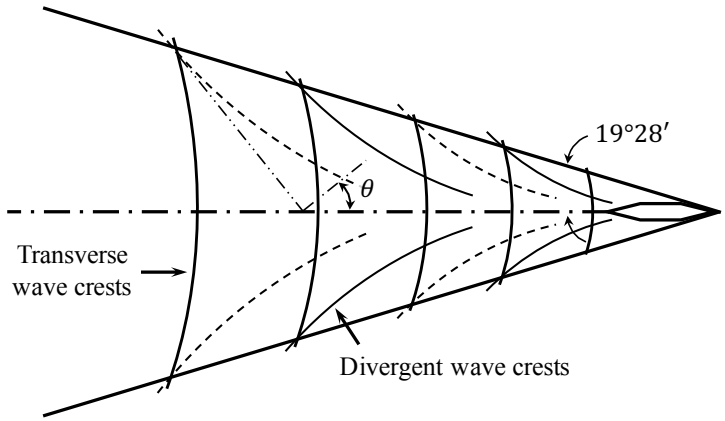

Figure 3.4: The Kelvin ship-wave pattern in deep water.

Havelock (1965) (also in Newman (2018)) show by energy arguments how to relate the complex wave amplitude function $A(\theta)$ to the wave resistance R_w

$$R_w = \frac{\pi}{2}\rho U^2 \int_{-\pi/2}^{\pi/2} |A(\theta)|^2 \cos^3\theta \; d\theta. \tag{3.5}$$

3.1.2 Multihull Model

For the study of ships in a canal, Newman (1962) applied the *method of images* to mimic the effects of walls in a canal by placing image pressure distributions in a transverse array. The same idea is used to impose canal walls by applying equations for multihull vessels (Tuck and Lazauskas, 1998; Faltinsen, 2005), where waves generated by each separate hull are linearly superposed to calculate the wave resistance. The wave amplitude function $A(\theta)$ due to N hulls can be expressed as

$$A(\theta) = \sum_{j=1}^{N} A_j(\theta) e^{-ik(\theta)[x_{j0}\cos\theta + y_{j0}\sin\theta]}. \tag{3.6}$$

Here $A_j(\theta)$ is the wave amplitude function of hull number j, the center of which has coordinates (x_{j0}, y_{j0}, z_{j0}) in the translating coordinate system (see Figure 2.1). While typical multihull studies are restricted to catamarans ($N = 2$), or trimarans ($N = 3$), in this study, more identical hulls are placed in a non-staggered fashion ($x_{j0} = 0$) with the same distance w between centerlines of adjacent hulls to achieve the effect of the central hull to be in a canal. Figure 3.5 shows a diagram of the multihull arrangement with three hulls. The three identical hulls are placed in a non-staggered way ($x_{j0} = 0$) with the same distance between adjacent hulls, symmetry plans are generated at the centerlines between adjacent hulls (dash lines in Figure 3.5) due to the symmetric wave patterns generated by individual hulls. The central hull is in between two symmetry planes, which mimics the scenario of a ship moving in a canal of width w.

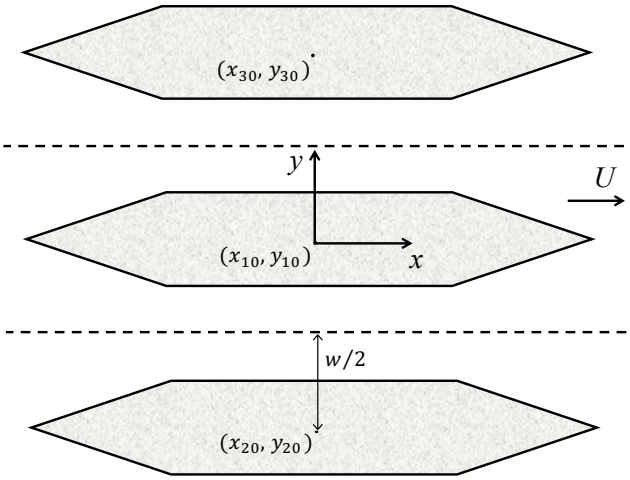

Figure 3.5: Schematic of a nonstaggered triple-hull system travelling at speed U in the translating coordinate system.

An infinite number of hulls is needed to create an ideal canal condition. This work uses a finite number of hulls to approximate the effects of canal walls at a reasonable cost. First, a convergence study on the number of hulls is performed to determine how many hulls are needed. The wave resistance is computed for the number of hulls in the range of $1 < N_{\text{hulls}} < 21$, and the results are shown in Figure 3.6. The results for all three speeds show that for $N_{\text{hulls}} = 15$ and above the canal condition is nearly achieved. Therefore, 15 hulls are used in the multihull model throughout this work for the evaluation of ship resistance in a canal.

By inserting Eqn. 3.6 into Eqn. 3.5, the equation for the total wave resistance of the multihull becomes

$$R_w = \frac{\pi}{2}\rho U^2 \int_{-\pi/2}^{\pi/2} |A(\theta)|_{ws}^2 \left(\sum_{m=1}^{n} 2\cos(m\mathcal{F}) + 1 \right) \cos^3\theta \; d\theta, \tag{3.7}$$

where $n = 7$ for a fifteen-hull system and A_{ws} is the wave function for a single hull. The term in parentheses is a hull interference function $F(\theta) = \sum_{m=1}^{m=7} 2\cos(m\mathcal{F}) + 1$ that captures the interaction among the fifteen hulls. The function $\mathcal{F}$ depends on the

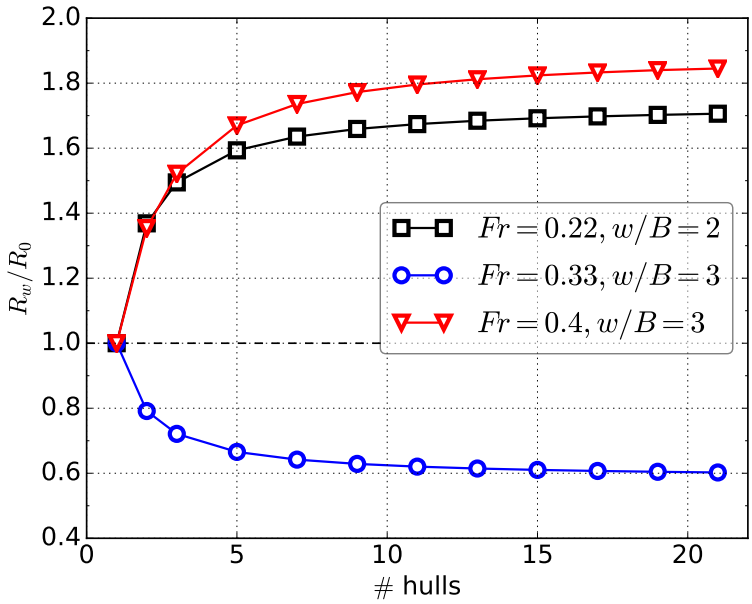

Figure 3.6: Relative resistance in canals against number of hulls used in the multihull model.

Froude number Fr, the ratio of hull spacing w and the ship length L, and θ,

$$\mathcal{F} = \frac{w/L}{Fr^2 \cos^2 \theta} \sin \theta. \tag{3.8}$$

The contribution to the integral for $\theta \to \pm\pi/2$ corresponds to contributions for divergent waves with very small wavelengths that travel perpendicular to the ship's track and have negligible influence on the wave resistance. Therefore, in the numerical evaluation of the integral in Eqn. 3.7, the limits are narrowed to $\pm(\pi/2 - \epsilon)$ to ease the difficulty in integrating around singularities at $\theta = \pm\pi/2$, here ϵ is a small number and a value of 0.02 is used.

3.2 Wave Resistance in a Canal

Eqn. 3.7 is evaluated for a range of hull separation w/B and Froude number, where w is the canal width or the distance between adjacent hull centers and B is the ship

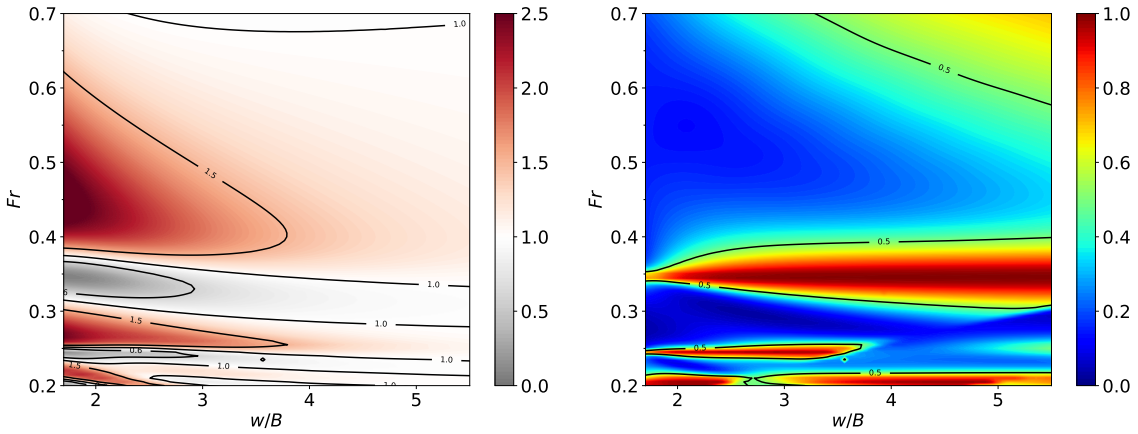

(a) Wave resistance relative to open water R_w/R_0

(b) Fraction of diverging wave resistance to total wave resistance $R_{w,d}/R_w$.

Figure 3.7: Wave resistance of ship in a canal as a function of Froude number and canal width.

beam. The results are shown in Figure 3.7a as the relative wave resistance R_w/R_0, where R_0 is the wave resistance in open water ($w \gg B$). Note that the wave resistance has either an increase up to +129% or a decrease up to −82% relative to the open water condition, and for lower speeds of $0.2 < Fr < 0.4$ the resistance oscillates rapidly with Froude number. For example for $w/B = 2$, a local maximum of wave resistance occurs near $Fr \approx 0.28$, and local minima occur for speeds of $Fr \approx 0.24$ and 0.35. Another major increase in resistance occurs between $Fr = 0.4$ and 0.5 in narrow canals. Higher ship speeds or wide canals generally have R_w/R_0 close to 1, which means the canal condition has no significant impact on the wave resistance compared to that in open water.

To further analyze how the wave resistance can vary in such a dramatic manner with relatively small changes in speed, the contributions of the transverse and

diverging waves to the drag are calculated separately. Eqn. 3.7 is expressed as

$$R_w = 2\int_0^{\pi/2-\epsilon} K(\theta)\, d\theta \tag{3.9}$$

$$= \underbrace{2\int_0^{\theta_1} K(\theta)\, d\theta}_{R_{w,t}} + \underbrace{2\int_{\theta_1}^{\pi/2-\epsilon} K(\theta)\, d\theta}_{R_{w,d}} \tag{3.10}$$

where the kernel function is $K(\theta) = |A(\theta)|^2_{ws} F(\theta) \cos^3\theta$. The first term in Eqn. 3.10 is the contribution to the resistance of the transverse waves $R_{w,t}$, and the second term is that of the diverging waves $R_{w,d}$. The fraction of the total wave resistance due to the diverging waves is calculated as $R_{w,d}/R_w$. This quantity is shown in Figure 3.7b. A striking feature appears in which the total resistance is dominated by the diverging waves for a speed $Fr \approx 0.35$, over the entire range of the canal width.

Note the strong correlation between the importance of divergent waves and reduced wave resistance by comparing Figure 3.7a and 3.7b for speed near $Fr \approx 0.35$. The large contribution of diverging waves also means the transverse waves are less significant. This is confirmed visually in Sec. IV using CFD simulations. It is also interesting to observe that the importance of the diverging waves is relatively independent of the canal width for $Fr \approx 0.35$, although the change in wave resistance decreases for larger values of canal width for other speeds.

The dominance of diverging waves for $Fr \approx 0.35$ or transverse waves for $Fr \approx 0.28$ can be explained by the fundamental wavelength. The fundamental wavelength is the length scale of the longest wave in the ship-generated wave system and is a function of ship speed and gravity: $\lambda = 2\pi U^2/g$ or $\lambda = 2\pi Fr^2 L$. For thin-ship theory, the source from the bow and sink from the stern can cancel or enhance each other at certain ship speeds, which also depends on the hull geometry. If the length of either the bow or stern part is small, that is, the ship has a long parallel midbody, then for $Fr = 0.4$, $\lambda = 2\pi Fr^2 L \approx L$, the bow source and stern sink are one wavelength

apart. The source and sink is 180° out of phase, we get minimum transverse waves as a cancellation effect is achieved. Correspondingly, for $Fr = 0.56$, the wavelength is $\lambda = 2\pi Fr^2 L \approx 2L$, the bow source and stern sink amplify each other and cause a relatively large transverse wave amplitude. There are also other Froude numbers for which either strong cancellation or amplification of transverse waves occurs, especially at lower speeds.

For the present wedge-shaped body with nonnegligible bow and stern parts as shown in Figure 3.3, the corresponding Froude numbers for strong cancellation or enhancement are shifted. The integrand $|A|^2\cos^3\theta$ in the resistance integral in Eqn. 3.5 is ploted for two Froude numbers in Figure 3.8. This figure shows how at $Fr = 0.35$ the wave resistance is dominated by diverging waves, whereas for $Fr = 0.28$ is it mostly transverse waves.

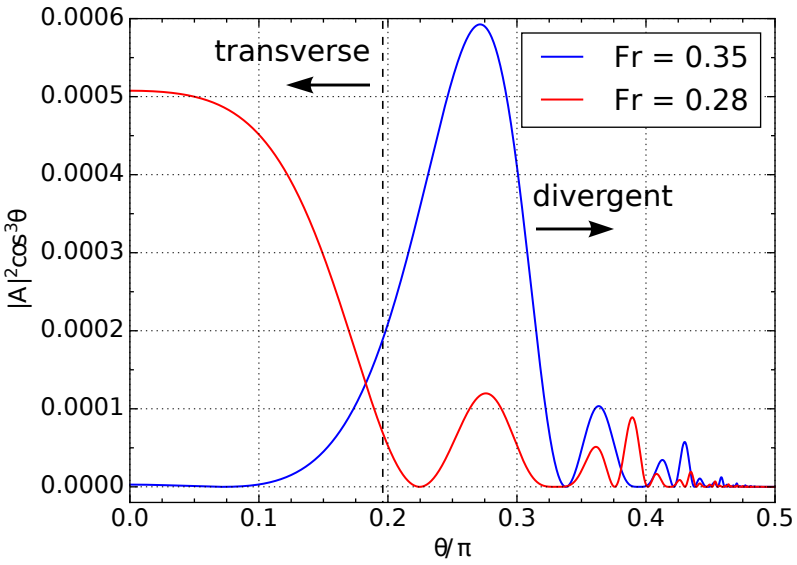

Figure 3.8: The integrand $|A|^2\cos^3\theta$ as a function of θ in the integral for wave resistance.

The relative contribution of transverse or diverging waves at different ship speeds can also be observed in experiments. Towing tank experiments were performed by a student team at the Aaron Friedman Marine Hydrodynamics Laboratory (Arciniega

et al., 2023), in which a model scale ONRT hull ($L = 3.14$ m) was towed at different speeds. The elevation time histories of the ship-generated waves were recorded by the wave probe on one side of the tank. More details of the experiments can be found in Appendix. A.

The ship-generated waves are analyzed in the frequency domain by applying Fast Fourier Transform (FFT) on the wave elevation sequences. Figure 3.9 demonstrates the frequency components of the waves at two Froude numbers, $Fr = 0.22$ and $Fr = 0.29$. The experiment with perforated spherical shells that mimic floating pancake ice is included in the plot but will not be analyzed in this work. The starting angular frequencies of the transverse and divergent waves, ω_T and ω_D, are plotted for reference. The angular frequencies are evaluated by the dispersion relation for deep-water free waves, i.e. $\omega^2 = gk(\theta)$, $\theta = 0$ and $\theta = 35°16'$ for the transverse and divergent waves, respectively, and $k(\theta) = k_0 \sec^2\theta$ is the wave number and $k_0 = g/U^2$. Transverse waves are those between ω_T and ω_D, beyond ω_D are the divergent waves. The plots clearly show that divergent waves are more evident for $Fr = 0.22$ and transverse waves are dominant for $Fr = 0.29$, which are consistent with the plot of contribution fractions in Figure 3.7b.

3.3 Summary

This chapter uses a theoretical analysis based on the work in Tuck and Lazauskas (1998) and Faltinsen (2005) for multi-hull vessels that is adapted to analyze a single ship in a deep-water canal, where the geometry of the ONRT is simplified and represented as a wedge-like shape such that the wave resistance can be evaluated analytically.

The changes of the wave resistance relative to that in open water are analyzed with respect to the ship speed and canal width. It is found that in deep-water but

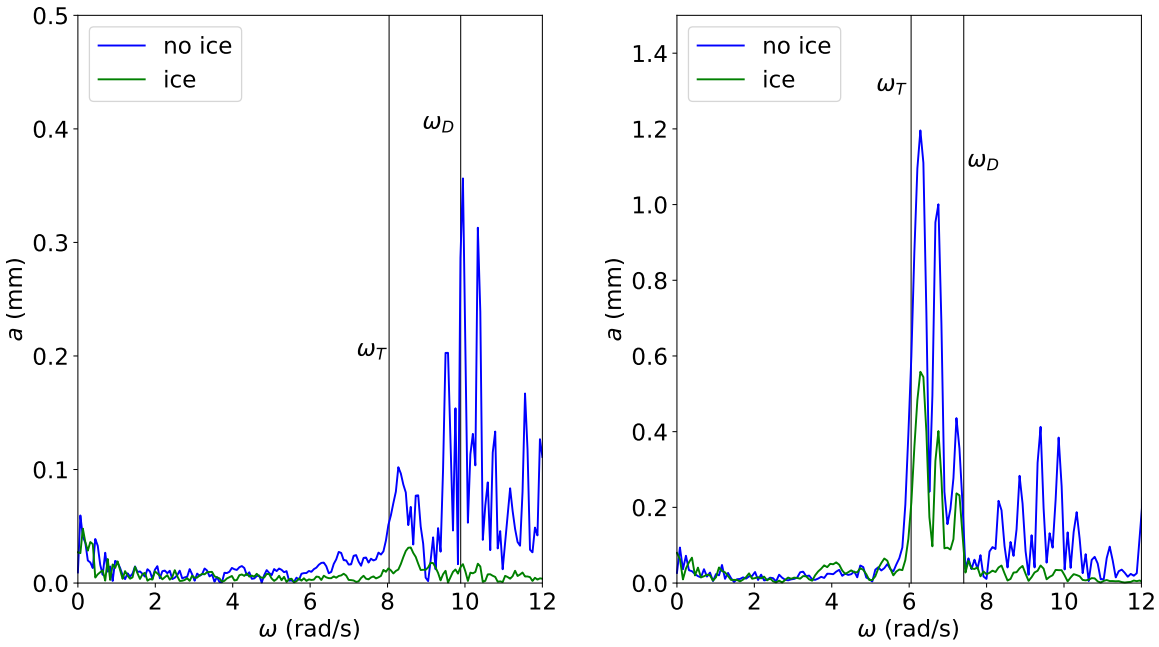

(a) $Fr = 0.22$ (b) $Fr = 0.29$

Figure 3.9: Spectral analysis of the wave profiles recorded at the wave probes with or without the perforated spherical shells. ω_T and ω_D are the starting angular frequencies of the corresponding transverse waves and divergent waves, respectively.

laterally constrained canals, a significant increase or decrease in wave resistance can happen with increases up to +129% and decreases up to −82% relative to the open water condition, depending on both the ship speed and canal width. The relative wave resistance oscillates rapidly for $Fr < 0.4$ in narrow channels. For higher ship speed or wide canals, the changes are moderate and canal effects are less pronounced.

The wave resistance is decomposed into the portions due to transverse and divergent waves. A striking feature is found for the ship speed $Fr \approx 0.35$, where strong dominance of divergent waves exists over the entire range of canal width. Strong correlation between the importance of divergent waves and reduced wave resistance is found for the ship speed $Fr \approx 0.35$ and other speeds like $Fr \approx 0.25$ and $Fr \approx 0.2$. Significant resistance increases are found for the conditions with transverse-wave dominance, but not vice versa. The dominance of divergent waves for $Fr \approx 0.35$ or transverse waves for $Fr \approx 0.28$ is explained by the fundamental wavelength and

cancellation of transverse waves that are generated by the ship bow and stern.

Time series of wave elevations, which were recorded in towing-tank experiments conducted by a student team, are analyzed on the frequency domain. The spectral distribution confirms the dominances of transverse and divergent waves at two different ship speeds from the theoretical analysis. The experiments also validate the linear theory of the simplified hull geometry.

CHAPTER IV

Ship Moving in a Lead between Rigid Ice Sheets

In this chapter, CFD simulations are used to study the problem of ship transit in open-water ice channels as depicted in Figure 1.3b, where the ice sheets of finite thickness are treated as rigid and the full-scale bare-hull ONRT is adopted as the ship model. The first section discusses the typical ice thicknesses in the Arctic region and utilizes the knowledge of the relationship between ice flexure and critical speed to justify the rigid-ice assumption. Section 4.2 presents the validation of CFD against experiments and a grid dependence study. Comparisons with the theoretical analysis for canal conditions are given in Section 4.3. CFD results are shown in Section 4.5 to demonstrate the effects of ice thickness on wave resistance. Simulations for a planing hull model are also included in the last section to discuss the higher ship speeds up to $Fr = 1.4$.

4.1 Ice Thickness and Flexure

First-year ice can grow to a thickness of up to 1 m, and multi-year ice can be much thicker. Submarine and satellite measurements (Kwok, 2018) show that the mean winter and fall ice thickness in the Arctic region varies from 1 to 3 m, and can be even thicker, especially when considering ridges. For example, Figure 4.1 shows a

map of sea ice thickness in the Arctic region in the later spring of 2023, when the ice is the thickest in a year. The ice thickness is mostly under 3 m, except for the regions off the coast of Greenland and the Canadian Archipelago, where ice thicker than 4.5 m can be found.

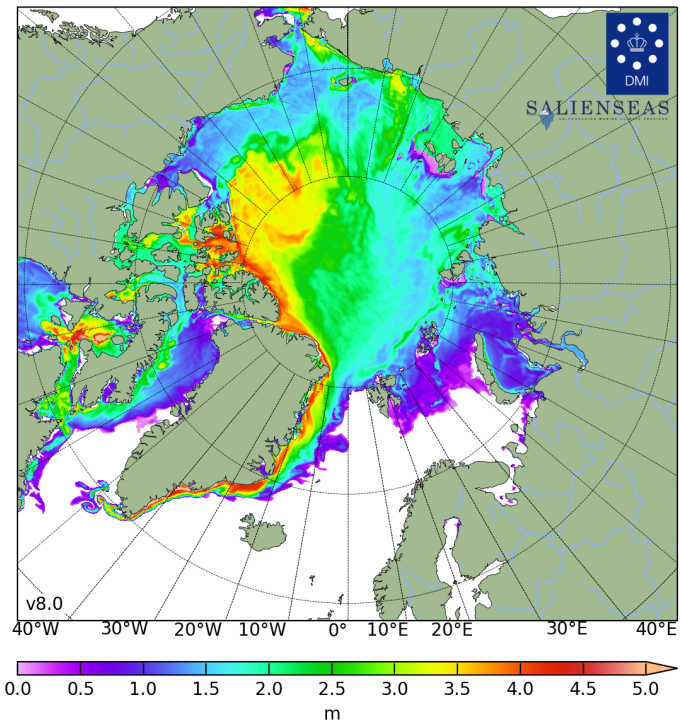

Figure 4.1: Real-time map of sea ice thickness in the Arctic region in May 2023, when the Arctic sea ice extent peaks in a year. Source: model calculations by Danish Meteorological Institute (DMI).

Thin ice covers can be considered to be flexible due to their large extent in the water plane, and small thickness, although due to the brittle nature of ice, its deflection is limited. Also, the deflection depends on the hydrodynamic forcing. When the speed of the ship is small relative to the critical speed in which flexural-gravity waves are generated and travel upstream of the ship, the deflections are very small. For example, the work of Xue et al. (2021) presents a method to analyze a pressure patch that either moves on an ice sheet, or over water between two ice sheets. Their results show how the ice deformation is related to the critical speed where flexural-gravity

waves appear in front of the disturbance. The critical speed in deep water for ice of infinite extent is defined as in Squire et al. (1996)

$$U_{\text{crit}} = 2\left(\frac{Dg^3}{27\rho}\right)^{\frac{1}{8}}, \tag{4.1}$$

where the ice rigidity is $D = Eh^3/12(1-\upsilon^2)$. Here E is Young's modulus of ice, and υ is the Poisson ratio. Xue et al. (2021) show that the ice deformation is very small for speeds that are smaller than the critical speed. As the speed is increased towards the critical speed the deformation grows rapidly and reaches a maximum, and then as the speed continues to increase the ice deformation slowly decreases.

The relationship between the critical speed and ice thickness, Eqn. 4.1, is indicated by the red curves in Figure 4.2. The conditions of the present CFD simulations that include the ice thickness and ship speed are plotted as symbols in Figure 4.2 for comparison. It is clear that the simulated ship speeds are well below the critical speeds that are evaluated by theory, which indicates small ice flexure. Note only the thinnest ice sheets of the simulations are displayed for each ship speed in the figure, thicker ice sheets are further from approaching the critical speed hence are not shown.

Given the above analysis, this chapter considers a simplified model using rigid ice sheets as small ice flexure is expected for the selected ice thickness and ship speed. It is assumed the ice flexure is sufficiently small (Xue et al., 2021) such that it does not alter the velocity or wave fields near the ship. It is also assumed that the transfer of energy away from the ship in the form of flexural-gravity waves is negligible with respect to the near-field waves and the force on the hull (Squire et al., 1996). Using a rigid-ice assumption also simplifies the CFD as the rigid ice can be simply treated as walls in the simulations. If the ice deflection is large relative to the wave field, or if the speed more closely approaches the critical speed such that flexural-gravity waves become significant, then ice flexure should be accounted for in the analysis. Flexible

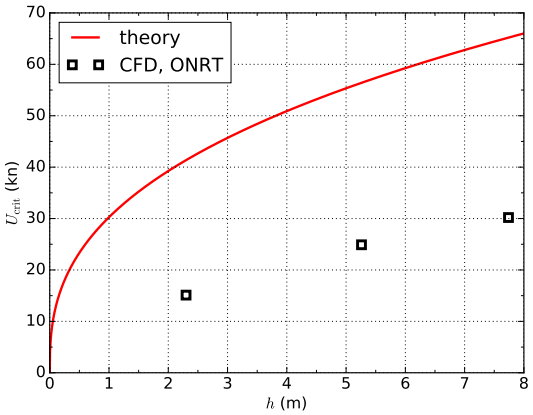

(a) theoretical U_{crit} and CFD simulation conditions for the ONRT model

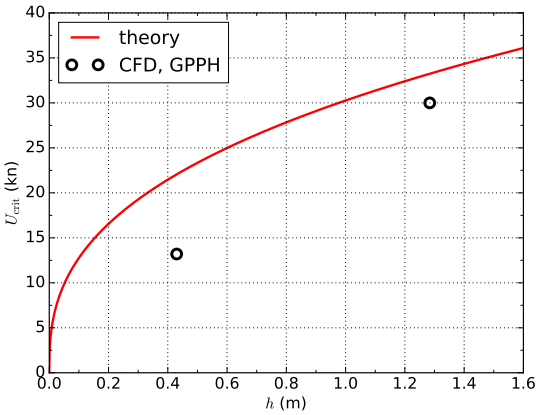

(b) theoretical U_{crit} and CFD simulation conditions for the GPPH model

Figure 4.2: The curves present the critical speed U_{crit} in deep water as a function of ice thickness h, derived for ice of infinite extent (Squire et al., 1996). The symbols indicate the conditions of the present CFD simulations with the two ship models (both evaluated in full scale). Only the thinnest ice is shown for each ship speed.

ice is studied in Chapter V.

4.2 Verification and Validation of CFD

Dependence of the CFD results on the mesh resolution is examined in terms of the total ship resistance in open water. The grid refinement ratio is used to represent the relative mesh resolution and is defined as

$$r_i = \sqrt[3]{\frac{N_1}{N_i}}, \tag{4.2}$$

where N_i is the total cell number of the i-th set of grid and N_1 is that of the finest grid. Five sets of systematically refined grids with grid refinement ratio values from $r_i = 1$ to 2 are adopted. The cell sizes and total number of cells are collected in Table 4.1. The simulations are run on the Great Lakes computing cluster and the finest grid requires approximately 40 hours to run for 120 seconds in physical time

with 180 Intel Xeon processors (3.0 GHz).

Table 4.1: Cell size and total number of cells for different mesh resolution. $Fr = 0.2$, open water.

r_i	$\Delta x_{\min}$ (m)	# cells (million)
2	0.15	1.745
1.6	0.12	3.246
1.4	0.105	4.672
1.2	0.09	7.466
1	0.075	13.55

The convergence of the total ship resistance R_T with the grid refinement ratio r_i is shown in Figure 4.3, where a fitted convergence curve with an estimated convergence order is also plotted. The fitting curve and estimated order-of-accuracy are determined following the procedure in Eça and Hoekstra (2014). In the procedure, the discretization errors are estimated with power series expansions as a function of the typical cell size (cell sizes in the bulk of the flow domain are used in this work), where the expansions are fitted to the data in the least-squares sense. The basic equation to estimate the discretization error ϵ_ϕ is

$$\epsilon_\phi \simeq \phi_i - \phi_0 = \alpha h_i^p. \tag{4.3}$$

where ϕ_i stands for any integral or other functional of a local flow quantity, ϕ_0 is the estimate of the exact solution, α is a constant to be determined, h_i is the typical cell size and p is the observed order of grid convergence. For the results in Figure 4.3, the exact solution is estimated to be $\phi_0 = 3.658$ N, a favorable order of $p = 2.4$ is observed for the convergence of the total ship resistance, which indicates the resistance converges faster than second order with grid refinement. The grid with $r_i = 1.2$ is selected for the rest of the simulations for the balance of numerical accuracy and computational cost.

Figure 4.4 compares the ship resistance coefficient C_T with experimental data

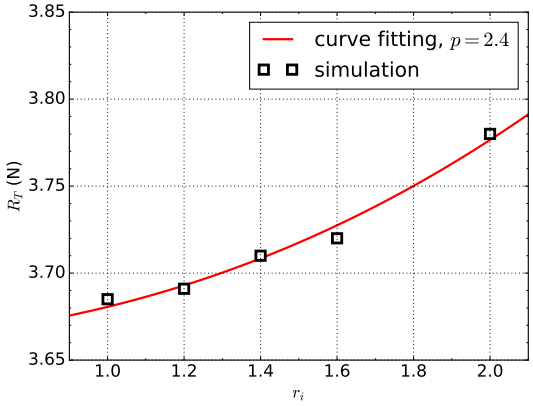

Figure 4.3: Convergence of the total ship resistance R_T with the grid refinement ratio r_i. The fitting curve and order of accuracy are estimated following the procedure in Eça and Hoekstra (2014). $Fr = 0.2$ in open water.

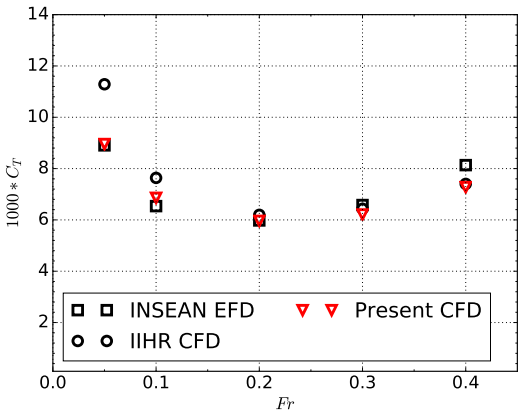

Figure 4.4: Resistance coefficient of present simulations as a function of Froude number, compared with experimental data from INSEAN and CFD results from IIHR (Cook, 2011).

from INSEAN and CFD results from IIHR (results for bare hull w/o BK in Table 4-1 in Cook (2011)) for validation purpose, in which C_T is defined as

$$C_T = \frac{R_T}{0.5\rho_w S U^2}, \tag{4.4}$$

where R_T is the total ship resistance and $S = 3,237$ m^2 is the wetted area. A good agreement can be observed between the present CFD results and the referenced experimental or CFD data.

4.3 Comparison with Theoretical Analysis

The CFD is run with the ONRT ship model for deep-water canals to compare the wave resistance with that of the theoretical analysis. The relative resistance R_w/R_0 of CFD simulations in a deep-water canal is plotted in Figure 4.5, along with the corresponding results from the theoretical analysis, where R_0 is the open-water wave resistance that is obtained by simulations of a wide canal ($w/B = 16$). In the CFD,

the wave resistance R_w is defined as the pressure part of the total resistance

$$R_w = \int_S -pn_x \, dS, \tag{4.5}$$

where S is the wetted surface of the ship and n_x is the x component of the outward-oriented normal to the ship surface. The other part of the total ship resistance in the CFD is the frictional resistance R_f, i.e. $R_T = R_w + R_f$. As R_f hardly changes for various channel conditions, only R_w will be analyzed in this work.

Two ship speeds are shown, and the CFD results generally follow the curve of the theoretical model. Discrepancy exists between the results though, especially in narrower canals, which is assumed to be mostly due to the difference in the detailed feature of the hull geometries and wave nonlinearity. Note that the resistance can increase by as much as 100 % at $Fr = 0.3$, or decrease by more than 20% at $Fr = 0.37$.

Figure 4.6 shows the relative resistance of both theoretical and CFD models in a canal of width $w = 3B$. Similarly, the CFD results exhibit both the increase and decrease in the resistance for different ship speeds in accordance with the linearized theory. The Froude numbers $Fr = 0.33$ and 0.4 are selected for the rest of the study of investigation into ice channels since significant decreases and increases in resistance occur at these two ship speeds. $Fr = 0.22$ with a narrower channel of $w = 2B$ is also studied based on the theoretical analysis in Figure 3.7a that suggests an increased wave resistance occurs at this condition.

The contribution to the resistance by transverse and divergent waves from the linear theory is also shown in Figure 4.6. For $Fr = 0.33$, divergent waves contribute 69.9% of the total resistance, while for $Fr = 0.4$, transverse waves contribute slightly more at 56.4%. The alteration of the resistance due to the ice sheet is due in part because of waves from the bow that reflect from the ice sheet and return to the hull. The transverse waves are oriented along the ship track $\theta < \theta_1 \approx 35$ deg, and do

not reflect and return to the ship (they interact much farther downstream). On the other hand, the diverging waves are oriented with a significant lateral component, and reflect from the nearby ice sheets within a short distance of leaving the ship hull and return to alter the near-field waves. Thus the conditions with significant diverging waves see stronger effects of reflection of the ship wave by the ice sheet on the wave resistance.

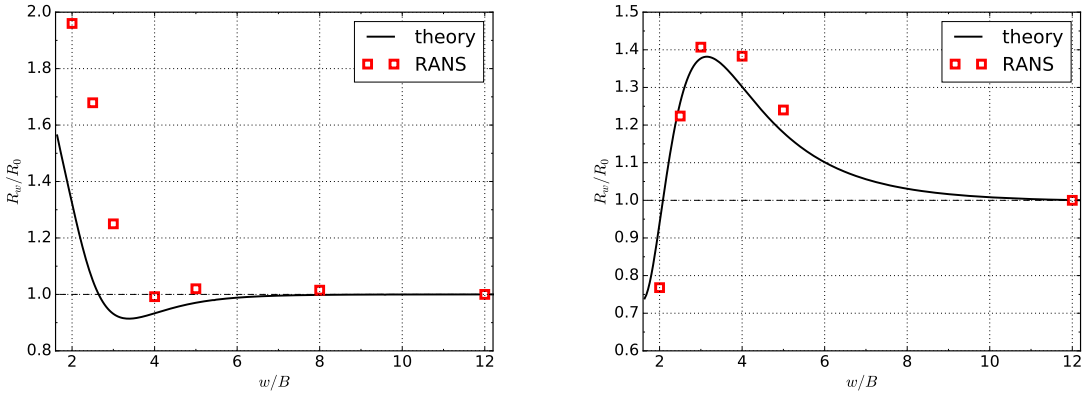

(a) $Fr = 0.3$ (b) $Fr = 0.37$

Figure 4.5: Relative wave resistance of theoretical and numerical modeling as a function of canal width.

4.4 Momentum Flux Analysis

A momentum flux analysis is performed on open-water simulations to motivate the connection between the ice thickness and the fundamental wavelength as the primary parameter that characterizes the interaction of ice sheets and the ship-wave field.

Conservation of linear momentum for a control volume around the hull links the momentum flux through the extent of the volume to the force of the hull on the fluid. The potential flow solution of free water waves indicates that the momentum is concentrated in the vicinity of the free surface which is where the ice interacts with the ship-generated waves. The fundamental solution for the velocity potential of a

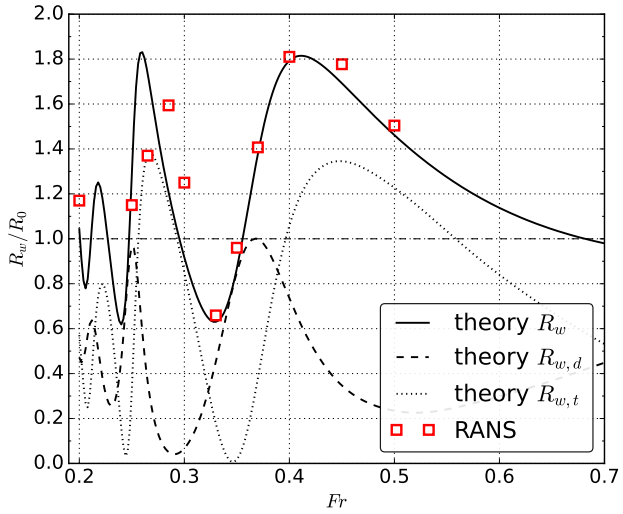

Figure 4.6: Relative wave resistance versus Froude number for a canal width of $w = 3B$. Dotted and dashed lines are the transverse and divergent wave resistance of the theory, respectively.

monochromatic small-steepness wave in deep water has a dependence on the vertical coordinate as e^{-kz}. The wave field generated by a ship can be decomposed into a spectrum of waves with different lengths, amplitudes, and heading angles, Eqn. 3.3. The ship wave field is sufficiently complex and it is not immediately evident how the edge of an ice sheet of finite thickness can act as a wall does in a canal. In order to investigate the analogy of a canal for operation in a lead, the axial momentum flux density is assessed using the CFD solution to see how it is concentrated near the water surface.

Consider a control volume of V that surrounds the ship hull, as shown in Figure 4.7. The volume has Cartesian boundary planes upstream A, downstream B, port P, starboard S, and bottom H. The volume is closed with the hull surface η and air-water interface ξ. Since the momentum of the fluid in this control volume is constant for steady operation, the momentum balance is the sum of the boundary terms. For the x component of momentum the conservation law can be expressed as $\sum \dot{M} = \sum F$

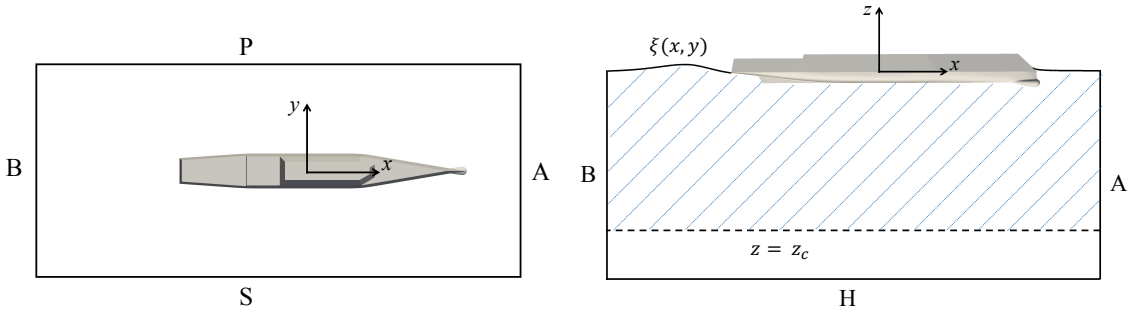

(a) Top view. (b) Side view.

Figure 4.7: Control volume and control surfaces around the hull in the translating coordinate system. The control volume is bounded by boundary plane upstream A, downstream B, port P, starboard S, and bottom H and is closed with the hull surface η and air-water interface ξ. Shadow in (b) indicates the integration area of the momentum flux $\dot{M}(z_c)$ in Eq. 4.8.

or

$$\dot{M}_A + \dot{M}_B + \dot{M}_S + \dot{M}_P = -R + F_A + F_B, \tag{4.6}$$

where $\dot{M}_c$ is the rate of x-direction momentum flowing through control plane c, and F_A and F_B are the pressure forces acting on planes A and B. R is the total force of the ship acting on the fluid.

The momentum flux through the port-side plane at $y = 3B/2$ is

$$\dot{M}_P = \int_{-H}^{\xi(x,3B/2)} \int_{x_A}^{x_B} \rho uv \; dxdz. \tag{4.7}$$

Here u and v are the horizontal and transverse components of the velocity due to the ship operation. They are dominated by the wave flow and each component is a function of space, i.e. $u(x, y, z)$ and $v(x, y, z)$, with an expected exponential decay in the vertical direction. The momentum flux through the lateral plane that is a function of the bottom coordinate z_c is evaluated as

$$\dot{M}(z_c) = \int_{z_c}^{\xi(x,3B/2)} \int_{x_A}^{x_B} \rho uv \; dxdz, \quad \text{for } z_c \geq -H \tag{4.8}$$

where z_c is the lower coordinate of integration and the integration area is demonstrated by the shadow in Figure 4.7b. When $z_c = -H$, i.e. when the integration is performed to the bottom of the domain, $\dot{M}(-H) = \dot{M}_P$. $\dot{M}(z_c)$ is calculated from the CFD solution for the open-water case for three Froude numbers at a lateral coordinate of $y = 3B/2$, and is shown in Figure 4.8. The momentum flux $\dot{M}(z_c)$ is normalized by $\dot{M}_P$. Also, the horizontal axis is normalized by the fundamental wavelength $\lambda = 2\pi Fr^2 L$.

Figure 4.8 shows that all three curves generally overlap with each other and the transport of axial momentum is concentrated in the layer near the water surface with a thickness of approximately 20% of the fundamental wavelength. This suggests that if the ice is thicker than 20% of λ, then it should act largely as a canal with complete refections of the wave field. This assertion is tested in the next section by computing the flow for different values of the thickness at different Froude numbers.

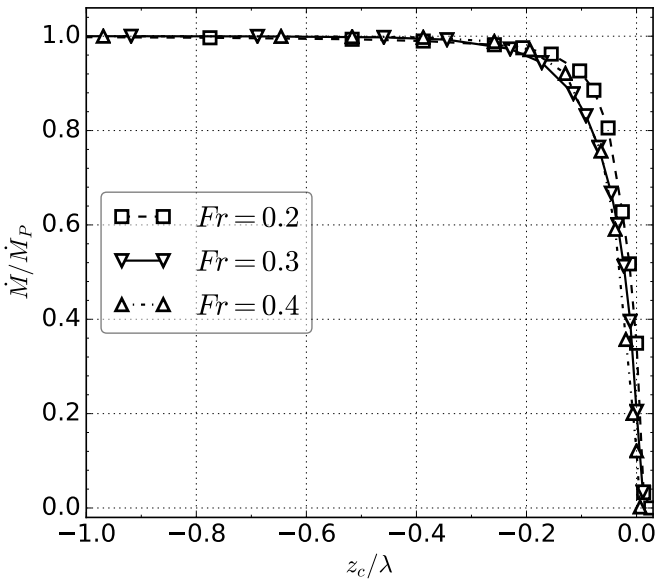

Figure 4.8: Vertical distribution of x-direction momentum flux through control plane P, at $y = 3B/2$.

4.5 Effect of Ice Thickness on Wave Resistance

A relationship between the ice thickness and the ship wave system is needed to generalize the findings across a range of ship sizes and ice thicknesses. The length scale of the longest ship-generated wave is the fundamental wavelength, which in deep water can be expressed as a function of ship speed and gravity $\lambda = 2\pi U^2/g$ or $\lambda = 2\pi Fr^2 L$. Therefore, in this section, the wave resistance of the ship operating in a lead between ice sheets of λ-dependent thickness is simulated with CFD. A range of ice thickness is investigated for different ship speeds and channel widths. Based on the momentum analysis in Sec 4.4, ice channels with four values of ice thickness in the range $0.05 < h^* < 0.2$ are investigated, where $h^* = h_{\text{sub}}/\lambda$ and h_{sub} is the thickness of the submerged part of the ice sheet. Overwash is prohibited by imposing a high freeboard. Three conditions, $Fr = 0.22$ with $w = 2B$, $Fr = 0.33$ and 0.4 with $w = 3B$, are analyzed. For each ship speed, the results for ice channels are compared with both the open-water and canal conditions.

Figure 4.9 shows the steady-state wave fields for $Fr = 0.22$ and $w = 2B$. In the top (a) of this figure a segment of the wave field for the ship in open water is shown. In the bottom (d) the canal condition is depicted. Frames (b) and (c) show the wave field for the case of ice of finite thickness. According to the theoretical analysis of a canal, both the transverse and divergent waves contribute to the wave resistance, and the resistance is significantly increased over the open-water value. The fundamental wavelength at this speed is $\lambda = 2\pi Fr^2 L \approx 0.3L$. In Figs. 4.9 b-d, the divergent waves can be seen reflected multiple times between the vertical ice edges or canal walls and the hull, creating complicated wave patterns around the hull.

The steady-state wave field for $Fr = 0.33$ is shown in Figure 4.10. This is a speed at which the diverging waves are dominant according to the theoretical analysis. The fundamental wavelength at this speed is $\lambda = 2\pi Fr^2 L \approx 0.7L$, which can be seen in the wave field behind the ship. For the canal case d, strong reflection is seen by

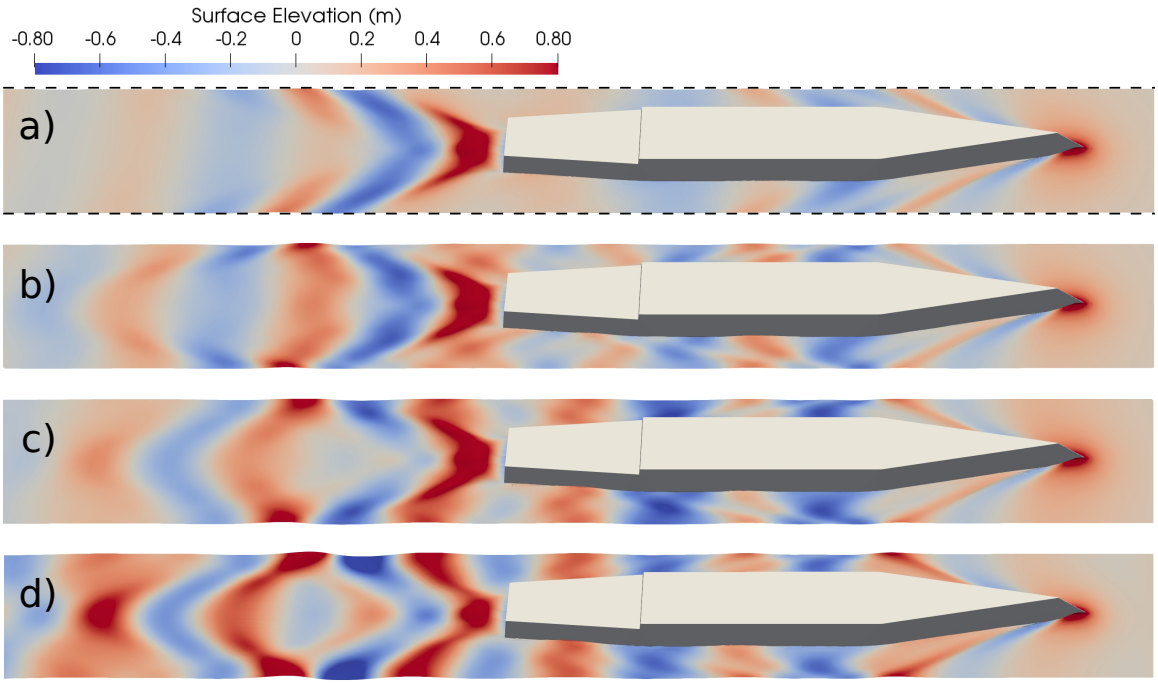

Figure 4.9: Wave fields for $Fr = 0.22$, colored by surface elevation. From top to bottom are in a) open water, b) ice channels with $h^* = 0.05$ and c) $h^* = 0.2$, and d) a canal. For a) open water, the wave field is cut at the dashed lines although the domain has a width of $16B$. For b-d the channels and canal have a width of $w = 2B$.

a large trough (depression) near the middle of the ship, and a large crest system immediately downstream of the transom. For both cases with ice shown in b and c, the reflection is also present, but to a lesser extent. Inspection of Figure 4.8 suggests that 65% of the axial momentum flux is concentrated in the layer that is blocked by the ice for the thin ice case with $h^* = 0.05$. For the thicker ice, nearly all of the axial momentum is concentrated in the layer of the ice. At this Froude number, the wave resistance decreases as the ice is thickened towards the canal condition. This is evident in the wave field because there is a reflected diverging wave that impinges the hull at $-0.4 < x/L < -0.2$ (mid-ship is at $x = 0$), and it increases the pressure on the stern region of the ship which applies a force in the direction of travel. This wave feature is shown in the figure with an oval and dashed line along the diverging wave crest. To more clearly see what is happening with changing ice thickness the

wave profile along the line $y = 0.55B$ is shown in Figure 4.11. The larger crest near the stern is evident for the channel and thicker ice together with the larger trough near midships. Note that the trough leads to reduced pressure on the hull, which could increase drag, but the axial component of the hull normal is close to zero for the middle of the ship, and thus its contribution to the hydrodynamic force integral is negligible.

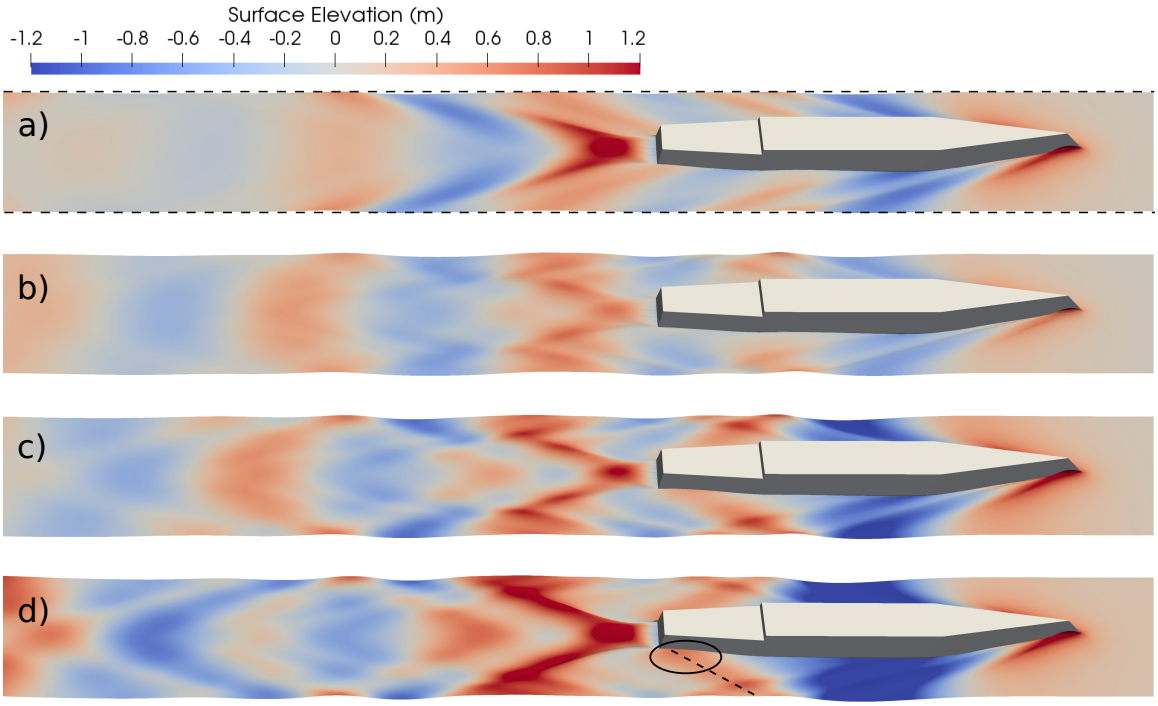

Figure 4.10: Same as Figure 4.9, but for $Fr = 0.33$, $w = 3B$.

Figure 4.12 shows the steady-state wave fields for $Fr = 0.4$. According to the theoretical analysis of a canal, both the transverse and diverging waves contribute to the wave resistance. As ice thickness increases, so does the wave amplitude. At this speed, the fundamental wavelength is nearly one ship length, and a large trough appears near the middle and rear portion of the hull $-0.5 < x/L < 0.1$. The deeper trough means a decrease in pressure and an increase in drag.

The sectional drag coefficient at location x is defined as the integration of hydro-

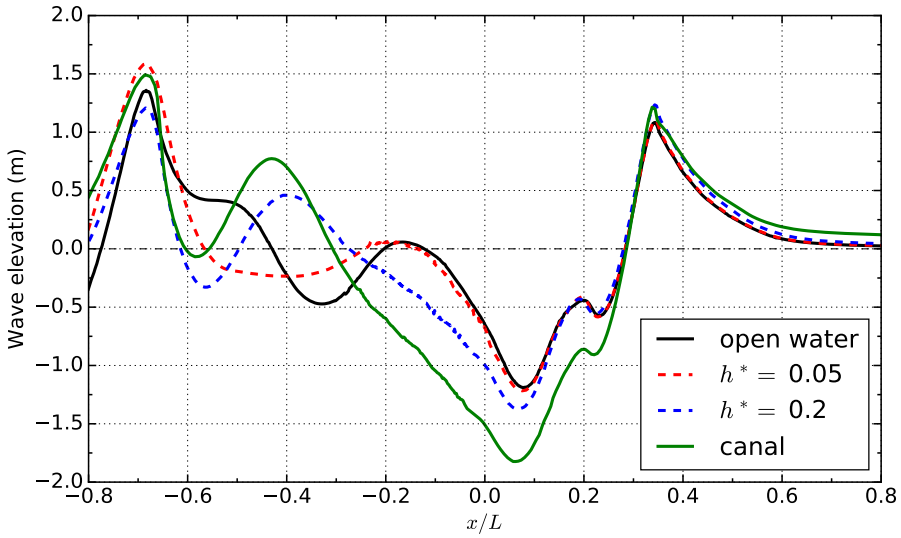

Figure 4.11: Wave elevations along $y = 0.55B$ for $Fr = 0.33$ and $w = 3B$.

pressure on the hull surface for a longitudinal length of Δx

$$C_d(x) = \frac{1}{\frac{1}{2}\rho U^2 S} \int_{A_x} -pn_x dA, \tag{4.9}$$

where A_x is the sectional hull surface area of between x and $x + \Delta x$. The integration of $C_d(x)$ over x within the range of the hull length should give the value of the total drag coefficient of the hull. Note negative values contribute to the increase of ship drag while positive values indicate *pushing* forces that offset ship drag. By showing the distribution of the drag force, we can more directly see where along the hull the resistance changes occur and confirm the analysis of the wave reflections and resistance changes.

The distribution of the drag force along the length of the hull is plotted in Figure 4.13 for $Fr = 0.33$ and 0.4. The profiles for open water and the thinnest ice of $h^* = 0.05$ are close to each other, which is consistent with the wave field observations. For $Fr = 0.33$, the section drag force for $h^* = 0.2$ is larger than that for either open water or $h^* = 0.05$ at $-0.4 < x/L < -0.2$, which indicates more *pushing* force offsets

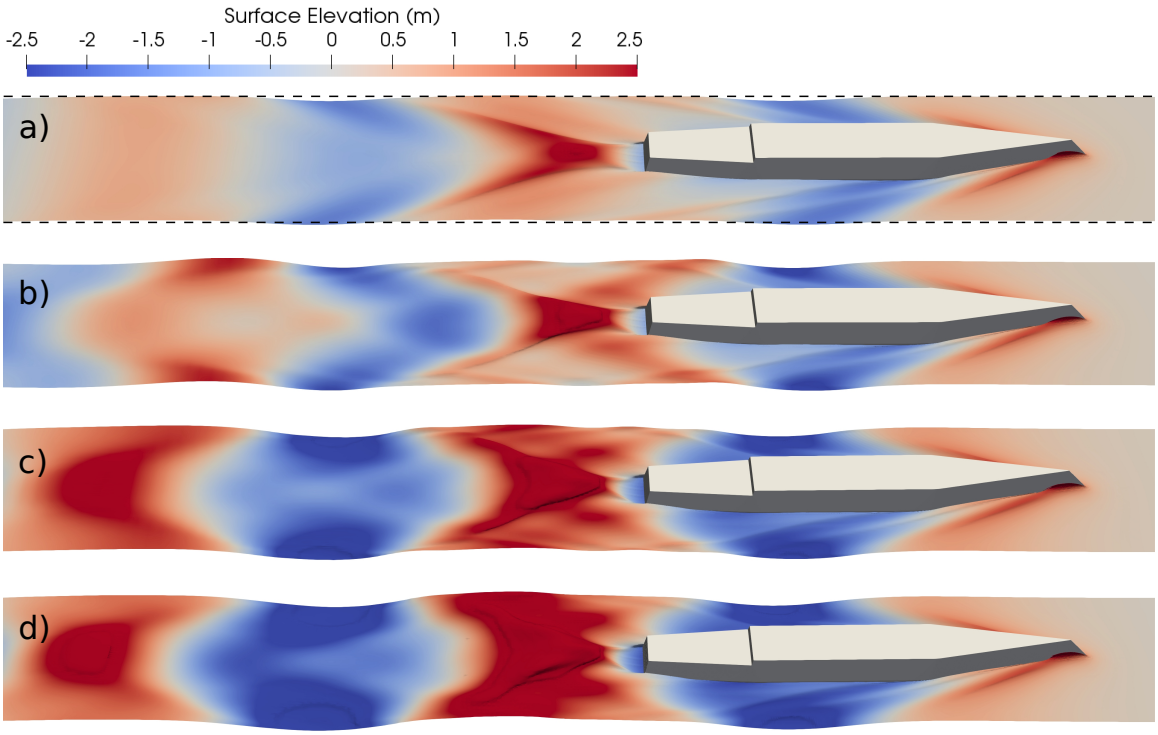

Figure 4.12: Same as Figure 4.9, but for $Fr = 0.4$, $w = 3B$

the total ship drag. This results in smaller R_w and confirms the analysis that the reflections of divergent waves impinge the hull at the stern and increase the pressure that applies a force in the direction of travel. For $Fr = 0.4$, the discrepancies exist for longer extension along the hull at $-0.4 < x/L < 0.4$, whereas they increase the total ship drag.

Table 4.2: Relative resistance (R/R_0) in open water, canal or ice channel. $w = 2B$ for $Fr = 0.22$, $w = 3B$ for $Fr = 0.33$ and 0.4.

Fr	open water	$h^* = 0.05$	$h^* = 0.1$	$h^* = 0.15$	$h^* = 0.2$	canal
0.22	1	1	1.13	1.24	1.32	1.42
0.33	1	0.93	0.76	0.7	0.69	0.66
0.4	1	1.03	1.35	1.62	1.74	1.81

The relative resistance for various conditions of speed and ice thickness are shown in Figure 4.14, and collected in Table 4.2. At $Fr = 0.33$, the relative resistance decreases as the ice thickens and approaches the canal condition. When the submerged

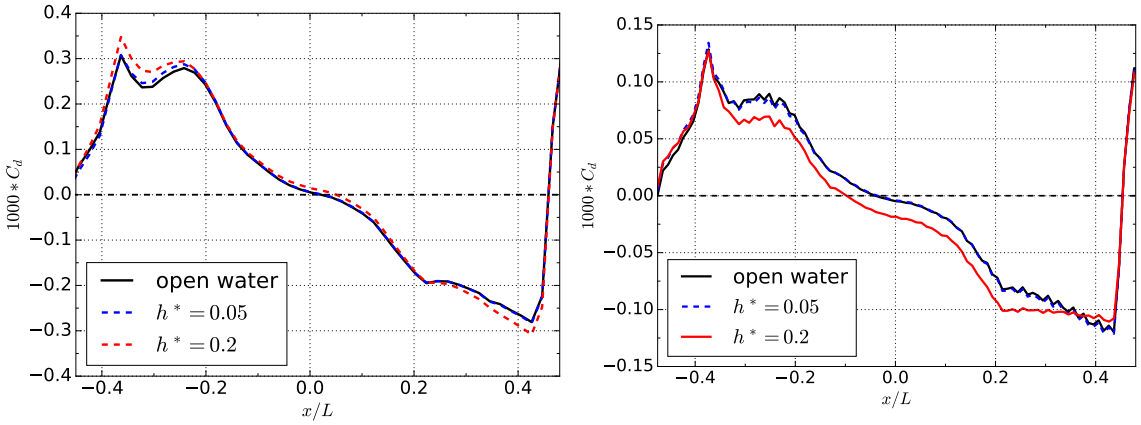

(a) $Fr = 0.33$

(b) $Fr = 0.4$

Figure 4.13: Distribution of sectional drag coefficient along the hull.

ice thickness reaches 20% of the wavelength, the relative resistance only has a 4.5% difference from that in a canal. Similarly, for $Fr = 0.4$, the relative resistance increases towards the value of the canal as ice becomes thicker. When the ice thickness is $h^* = 0.2$ the difference with a canal is less than 5% for both speeds. Note that the change in wave resistance is a 31% reduction at $Fr = 0.33$ and a 74% increase at $Fr = 0.4$, compared to the open-water case.

4.6 Planing Hull Model

High-speed planing boats are another type of craft that is of interest in this study. When at high speeds, the boat weight is predominantly supported by hydrodynamic lift, rather than hydrostatic lift (buoyancy). The ship-length Froude number, $Fr = U/\sqrt{gL}$, is usually > 1 in planing conditions. This study uses a model scale of the GPPH as the ship model. The computational domain and boundary conditions are the same as described in Section 2.1. The planing hull is allowed to heave and pitch. Only half of the computational domain is simulated with the use of a symmetry plane along the centerline and assuming the flow solutions and ship motions are

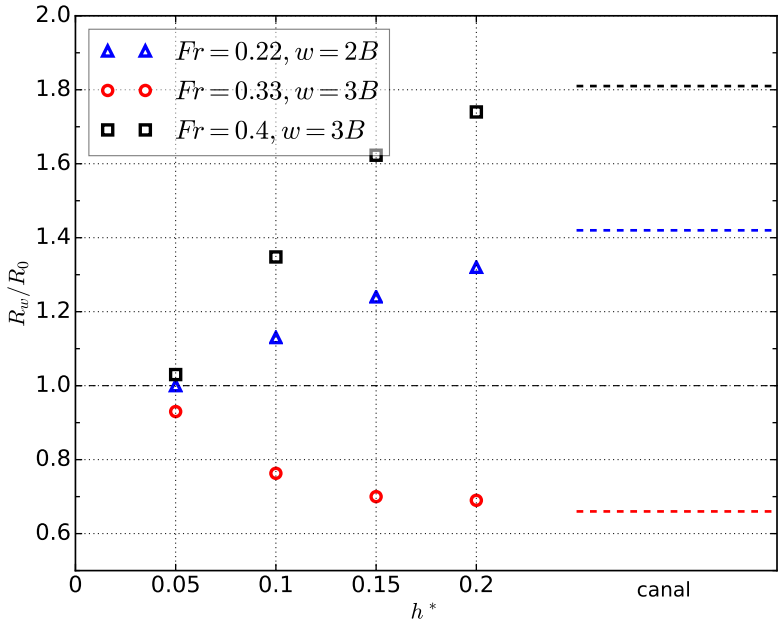

Figure 4.14: Relative resistance as a function of the relative submerged ice thickness $h^* = h_{\text{sub}}/\lambda$.

symmetric. The geometry of the ship model and spatial discretization can be found in Section 2.1.3.

4.6.1 Grid Refinement Study

A grid refinement study is first performed to assess the sensitivity of the results on the numerical discretization. Four systematically refined grids with resolutions of 40 mm, 30 mm, 24 mm and 20 mm in the bulk of the flow domain are adopted as the very coarse, coarse, medium and fine grids. The grid resolution is represented by a grid refinement ratio r_i, which is collected in Table 4.3 along with the cell size and total number of cells. Figure 4.15 shows some example partial meshes from the systematically refined meshes with different grid refinement ratios r_i. The steady-state wave profiles at different locations with various grid resolutions are displayed in Figure 4.16, which show that except the very coarse grid of $r_i = 2$ overestimate some wave crests, the other three finer grids give close solutions in terms of the wave fields.

Figure 4.17 shows the convergence of the resistance, which consists of the pressure and friction components. The convergence of the ship motions in terms of sinkage and trim angle related to calm water position is shown in Figure 4.18. Based on the above convergence studies, a grid refinement ratio $r_i = 1.2$ was selected for the rest of the parametric studies as a balance of accuracy and computational cost.

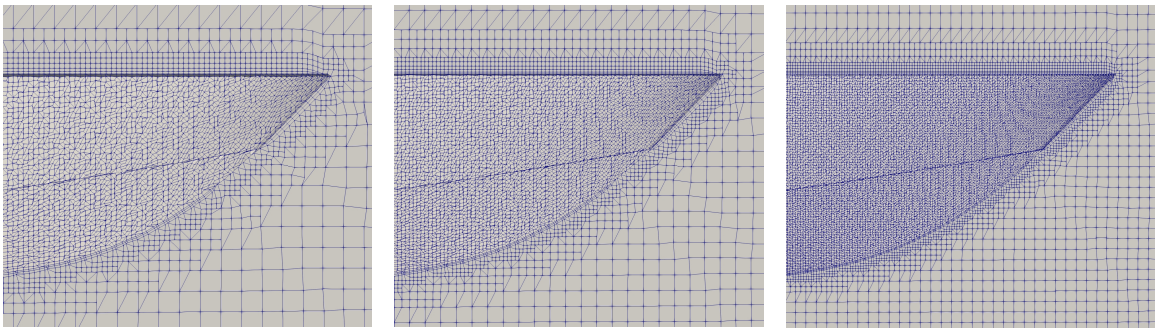

(a) $r_i = 2$ (b) $r_i = 1.5$ (c) $r_i = 1$

Figure 4.15: Systematically refined meshes with different grid refinement ratios r_i. The meshes are around the bow area, and are on the hull surface or the symmetry plane of the computational domain.

4.6.2 Convergence on the Domain Extent

The convergence on domain extent is also studied. Table 4.4 shows the steady-state quantities of forces and ship motions, from which we can see good convergence behaviors even though the domain has relatively small sizes. A combination of $h = 5L$, $L_{dn} = 4L$ and $L_{up} = 4L$ is selected for the parametric studies.

Table 4.3: Cell size and total number of cells for various mesh resolution.

Mesh	r_i	$\Delta x_{\min}$ (mm)	# cells (million)
Very coarse	2	5	0.96
Coarse	1.5	3.75	2.25
Medium	1.2	3	4.55
Fine	1	2.5	7.26

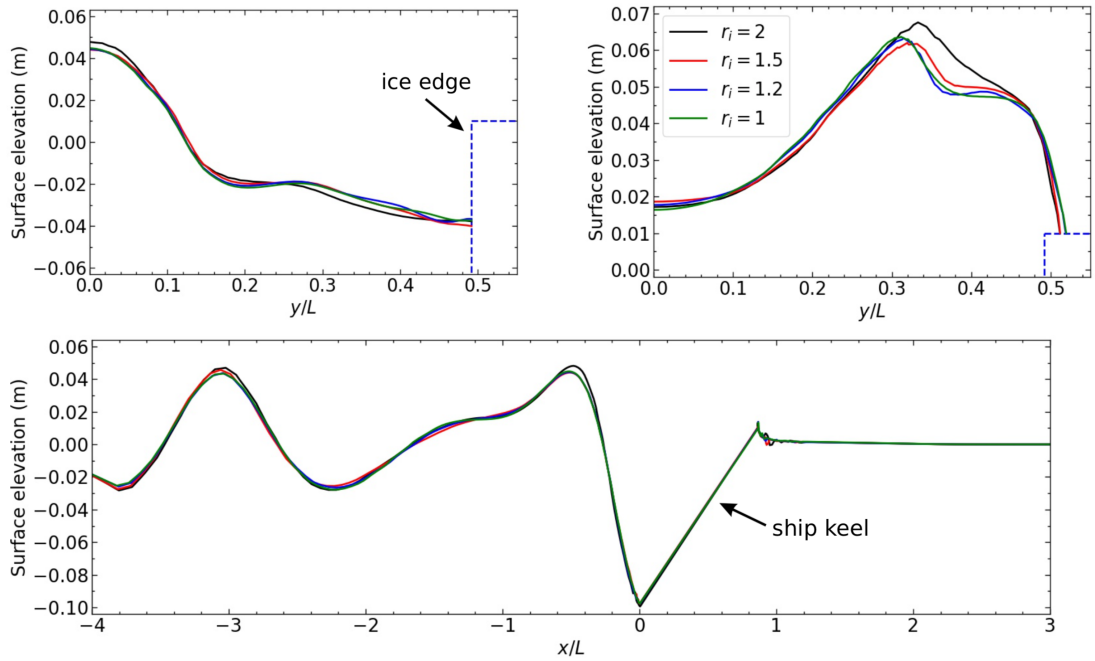

Figure 4.16: Steady-state wave profiles with various grid resolutions. The top two are transverse cuts at $0.5L$ (left) and $1L$ (right) behind the stern, the bottom is along the symmetry plane. Ice edges are indicated by blue dash lines.

4.6.3 Effects of Ship Speed, Channel Width and Ice Thickness

For the parametric study, different ship speeds (Fr = 0.4, 0.6, 0.8, 1, 1.2 and 1.4), channel width (w/B = 1.6, 3.2 and 6.5), and ice thickness ($h/B > 0.1$) are tested. The steady-state ship wake of different test conditions is compared in Figure 4.19 and Figure 4.20, where the air-water interface is colored by elevation. In Figure 4.19, the Froude number is 0.6, and three different channel widths are compared. It clearly shows that the narrowest channel has a significant effect on the wave profile. Most notably the first crest is much more pronounced, and the wavelength is reduced. Also, the amount of overwash onto the ice is increased for the narrowest channel width.

Figure 4.20 shows the effect of ship speed on the wave profile for the intermediate channel width of w/B = 3.2. The increase in speed results in an increase in the wavelength and it appears that for the greatest speed, the wave-ice interaction is far

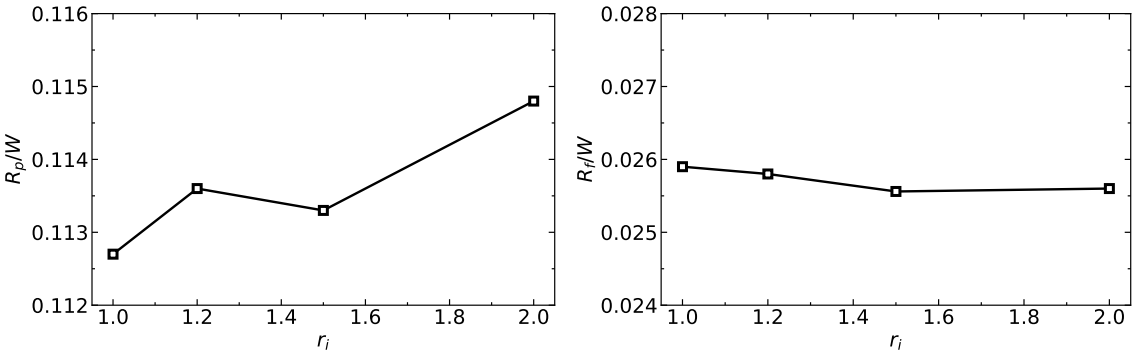

(a) pressure component (b) friction component

Figure 4.17: Normalized resistance components as a function of grid refinement ratio r_i. W is the weight of the hull.

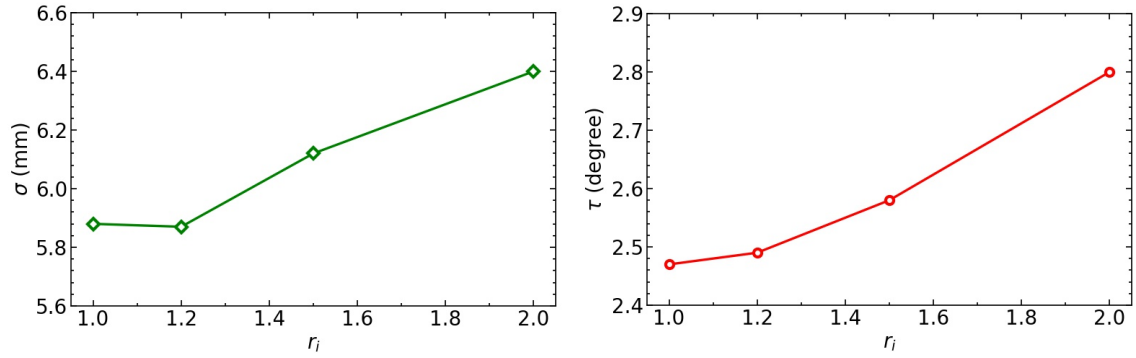

(a) sinkage (b) trim angle

Figure 4.18: Convergence of steady-state sinkage and trim angles.

behind the ship.

The effect of the channel width on the wave field is examined more closely by plotting the wave elevation on the centerline behind the vessel in Figure 4.21. The first wave crest is located at $x/L \approx -1$ for all three channel widths, but the first trough is much closer to the ship hull for the narrowest width of $w/B = 1.6$. Thus the narrow channel has the effect of shortening the wave behind the vessel. When comparing the other two channel widths the wave length of the widest channel has the smallest amplitude wave and the longest wavelength.

It is known that waves moving over a current have their length attenuated (Dal-

Table 4.4: Steady-state ship resistance, trim and sinkage with different domain sizes: upstream length (L_{up}), downstream length (L_{dn}) and water depth (H). The base case has domain sizes of $H = 2.5L$, $L_{dn} = 4L$ and $L_{up} = 2L$, which are used if not stated otherwise.

Domain size	Resistance (N)	Trim (°)	Sinkage (mm)
base case	7.03	2.58	6.1
$H = 5L$	7.03	2.59	6.1
$L_{dn} = 7L$	7.04	2.6	6.2
$L_{up} = 4L$	7.05	2.61	6.2
$L_{up} = 6L$	7.06	2.61	6.2

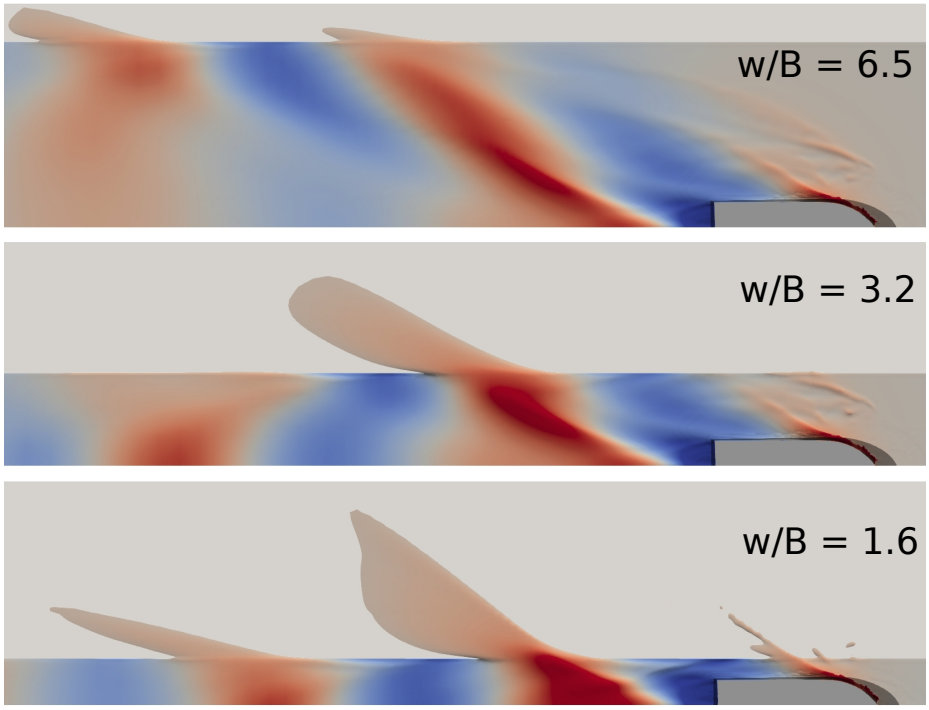

Figure 4.19: Top view of the wave fields with the hull and ice for different channel widths with $Fr = 0.6$ and $h/B = 0.1$. Air-water interface is colored by elevation.

rymple, 1974), and to investigate the role of the channel width on the fluid velocity behind the ship different profiles are shown in Figure 4.22. It can be seen that the narrower channel produces a larger perturbation to the velocity field, but no discernible current is evident. It appears the shortening of the wave is a local effect of the ship-ice interaction.

The pressure part of ship resistance R_p is presented as a function of ice thickness

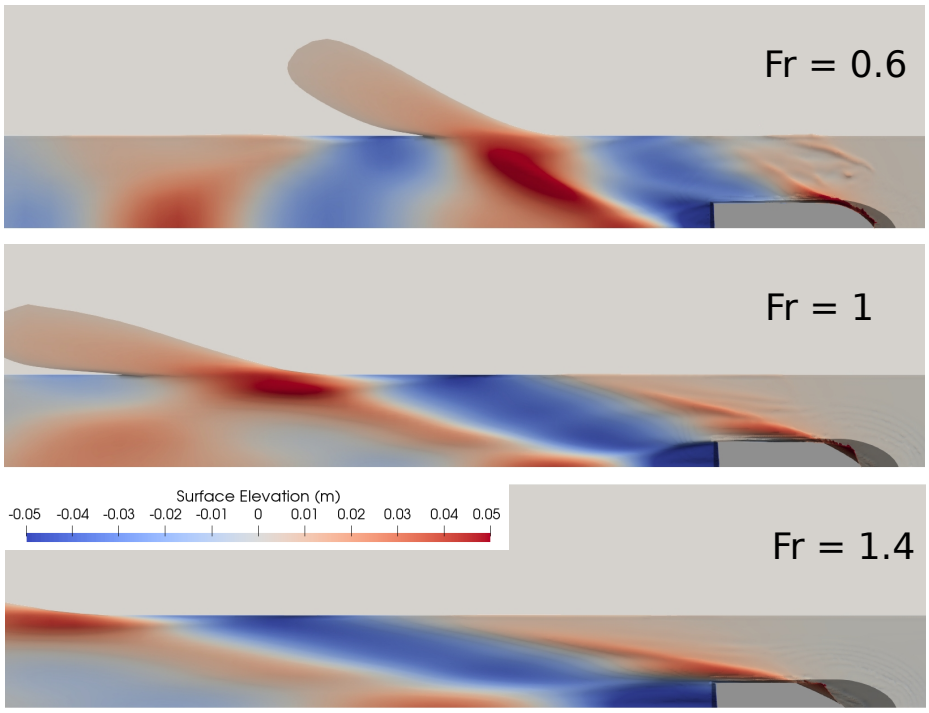

Figure 4.20: Top view of the wave fields with the hull and ice for different ship speeds with $w/B = 3.2$ and $h/B = 0.1$. Air-water interface is colored by elevation.

in Figure 4.23, which is nondimensionalized by the ship weight W. The curves for $w/B = 3.2$ and 6.5 are almost flat and are in line with the open-water and canal cases, meaning ship resistance is insensitive to ice thickness for wide channels. For the narrowest channel, ship resistance varies with the ice thickness. It is interesting to see that for the speed $Fr = 0.6$ the resistance in $w/B = 1.6$ is always greater than that for the wider channel, and the increase is greatest for very thin ice or the thickest ice. On the other hand for the speeds $Fr = 1.0$ and 1.4 the resistance decreases with increasing ice thickness for the narrowest channel, and it is less than the value for open water for the thickest ice. Variance in resistance with different channel widths or ice thicknesses exists but is much less significant than that for the ONRT cases, where the high Froude number is believed to be the main reason. The fundamental wavelength is larger for higher Froude numbers, i.e. $\lambda = 2\pi Fr^2 L \approx 2.3L$, $6.3L$ and $12.3L$ for $Fr = 0.6$, $Fr = 1$ and $Fr = 1.4$, respectively. Wave and ice interactions

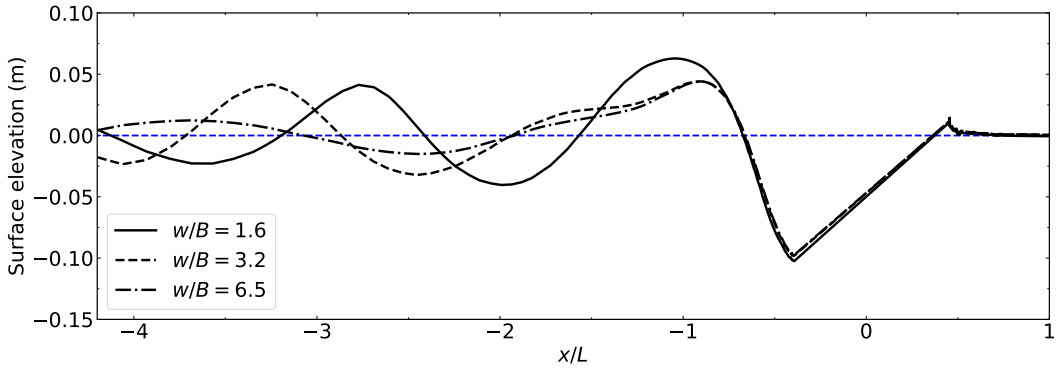

Figure 4.21: Wave elevation along the centerline at steady state, $Fr = 0.6$, $h/B = 0.1$. The COG of the ship is located at $x/L = 0$.

mainly happen further downstream, which provides less influence on the near-field hydrodynamics. Additionally, the relative ice thickness is smaller compared with the larger fundamental wavelength. Even for $h/B = 1$, the ice thickness is 0.37 m and is only 6% of the fundamental wavelength for $Fr = 0.6$. The wave resistance values for $Fr = 0.6$ and 1, and $w/B = 1.6$ and 6.5 are normalized by the corresponding open-water resistance and are plotted in Figure 4.24 as a function of the relative ice thickness $h^* = h_{\text{sub}}/\lambda$. Note for $Fr = 1$, the wavelength of the divergent waves $\lambda_D = 4\pi Fr^2 L/3$ is used instead of the fundamental wavelength of the pure transverse wave as the divergent waves are prominent at this critical speed. For the wide channel of $w/B = 6.5$, the resistance is similar to that in open water for both ship speeds, indicating the existence of ice has little impact on the ship resistance when the lead is wide. For the narrow channel of $w/B = 1.6$, the relative wave resistance in the lead approaches that in a canal as the ice thickness is increased toward 20% of λ or λ_D, which is similar to that for the ONRT ship model in Figure 4.14.

Figure 4.25 shows the ship resistance, sinkage, and trim angle as a function of Froude number. In each figure data are shown for each channel width and the ice thickness is $h/B = 0.1$ for all cases. Pressure component of ship resistance R_p is non-dimensionalized by the ship weight W. δ represents the sinkage of the center of gravity (CoG) of the ship, which is normalized by the ship length L and is positive

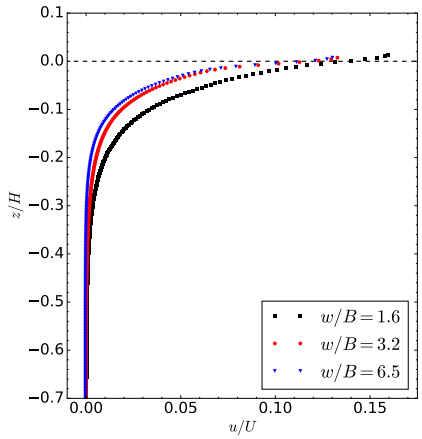

(a) Streamwise velocity on the centerline and one ship length behind the stern as a function of vertical coordinate.

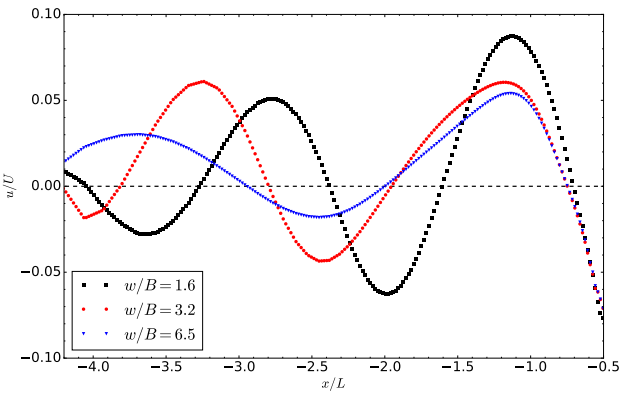

(b) Streamwise velocity on centerline at depth of stern as a function of streamwise coordinate.

Figure 4.22: Streamwise velocity profiles for different channel widths. $Fr = 0.6$, $h/B = 0.1$, $H = 3$ m.

upward. τ is the trim angle with respect to the CoG and is positive for bow up. Overall, all three quantities vary by the Froude number while only minor discrepancy exists for different channel widths, which indicates the ship speed is a more prominent factor for this high Froude number regime ($Fr > 0.4$), i.e. the ship forces and motions are not very different than in open water with this thin sheet ice ($h/B = 0.1$). The resistance first increases with the Froude number up to $Fr = 0.8$ and then decreases, which indicates the peak exits between $Fr = 0.6$ and $Fr = 1$. The sinkage increases monotonously with the Froude number and switched from negative value to positive between $Fr = 0.6$ and 0.8. The trim angle increases rapidly with the Froude number and the hull switches from bow down to bow up between $Fr = 0.4$ and $Fr = 0.6$, then gradually plateaues at around 5° for $Fr > 1$.

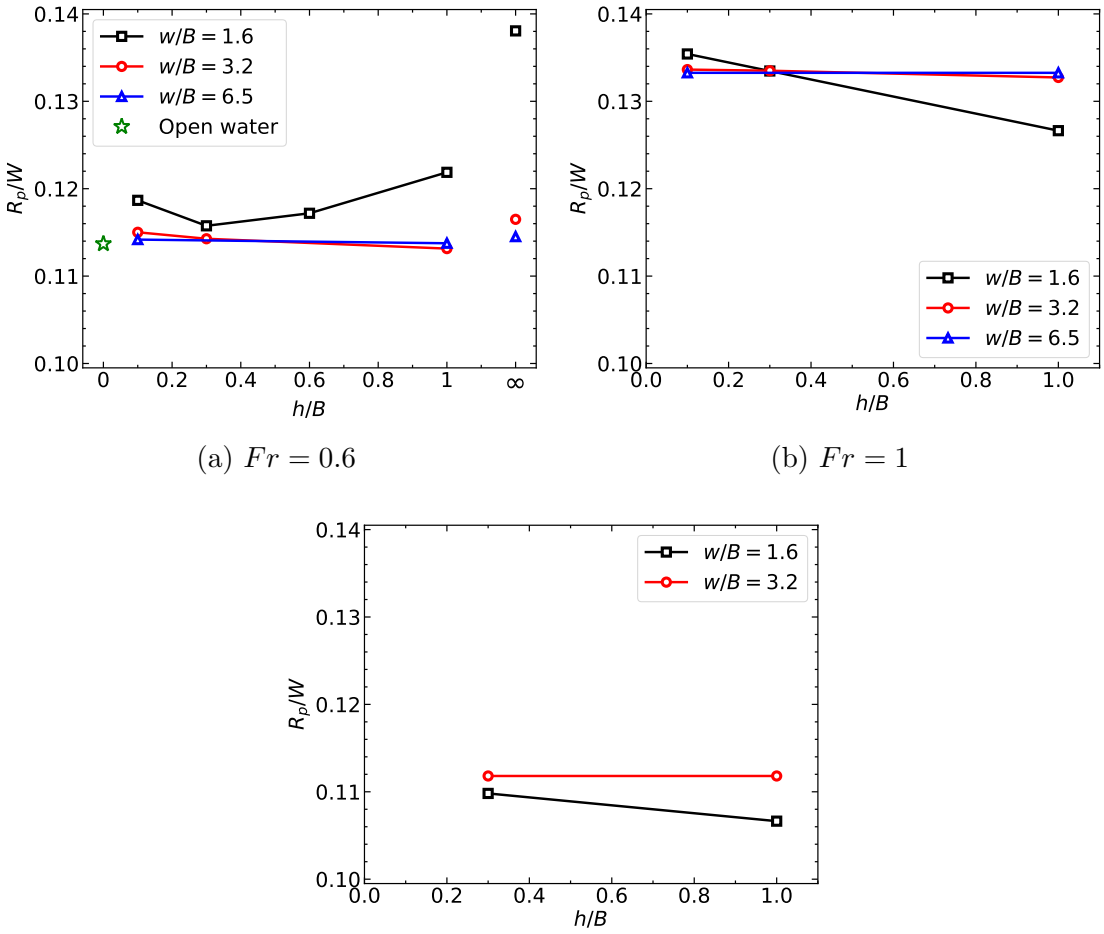

(a) $Fr = 0.6$

(b) $Fr = 1$

(c) $Fr = 1.4$

Figure 4.23: Pressure component of ship resistance versus ice thickness nondimensionalized by the ship weight W. Infinite ice thickness in (a) refers to test cases in a canal.

4.6.4 Overwash Mass Flux

Significant amounts of overwash can be observed from the wave contours in Figure 4.19 and Figure 4.20. Overwash causes energy dissipation of ship-generated waves through wave breaking, which affects the wave pattern and can alter the ship hydrodynamics. Overwash also has an impact on the hydroelasticity of the flexible ice, where the green water on top of the ice can either increase or decrease the local ice deflection and strain, which either assists or impedes ice fracture. The impact of overwash on

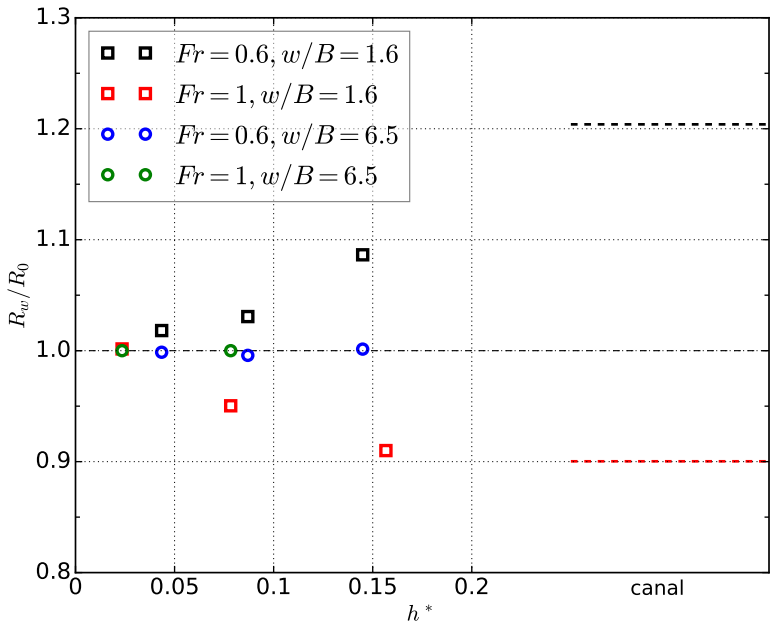

Figure 4.24: Relative resistance as a function of the relative submerged ice thickness $h^* = h_{\text{sub}}/\lambda$.

ice hydroelasticity is not considered in this chapter but is discussed in Chapter V for flexible ice. This section quantifies the overwash intensity by evaluating the overwash mass flux $\dot{m}$ over the ice sheet through the vertical plane above the ice edge

$$\dot{m} = \int_{0.1h}^{\xi(x,w/2)} \int_{x_B}^{x_A} \rho v \; dxdz, \quad \text{for } \xi(x, w/2) > 0.1h \tag{4.10}$$

where v is the y-component of the water velocity, the integration area is a finite vertical plane above the ice edge at $y = w/2$, which is horizontally throughout the computational domain from $x = x_B$ to $x = x_A$, and is vertically bounded by the top of the ice edge $z = 0.1h$ and the wave elevation above the ice edge, i.e. $z = \xi(x, w/2)$ for $\xi(x, w/2) > 0.1h$.

The overwash mass flux at steady state for two ship speeds and three channel widths are plotted in Figure 4.26 against the relative ice thickness h/B. The amount of overwash is significant as nearly 20 kg/s of mass fluxes are generated on each side of the ship, whereas the displacement of the model scale ship is only 12.66 kg. The mass

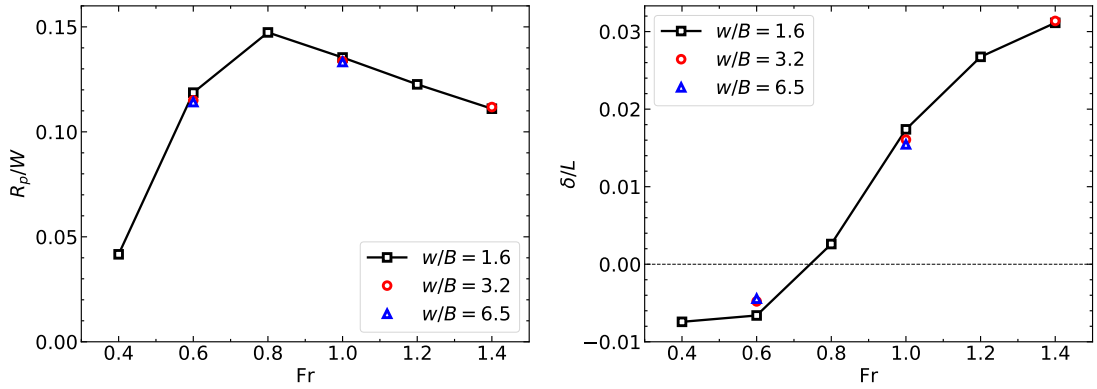

(a) nondimensional resistance

(b) nondimensional sinkage

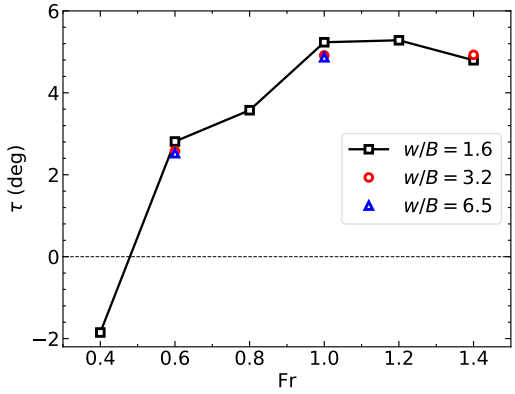

(c) trim angle

Figure 4.25: Steady-state values of resistance, sinkage, and trim angle as a function of Froude number. $h/B = 0.1$.

flux is higher in narrower channels with thinner ice, and higher ship speed generally leads to higher mass flux.

The overwash mass flux is further normalized by the displacement of the ship m, ship length L, and ship speed U

$$\dot{m}' = \frac{\dot{m}L}{mU}. \tag{4.11}$$

The normalized overwash mass flux $\dot{m}'$ for the same conditions is shown in Figure 4.27, which shows similar trends as a function of the ice thickness and channel width as in Figure 4.26, but more directly demonstrates the fraction of mass onto the ice on each side of the ship for each ship length it traveled. For example, for $Fr = 0.6$,

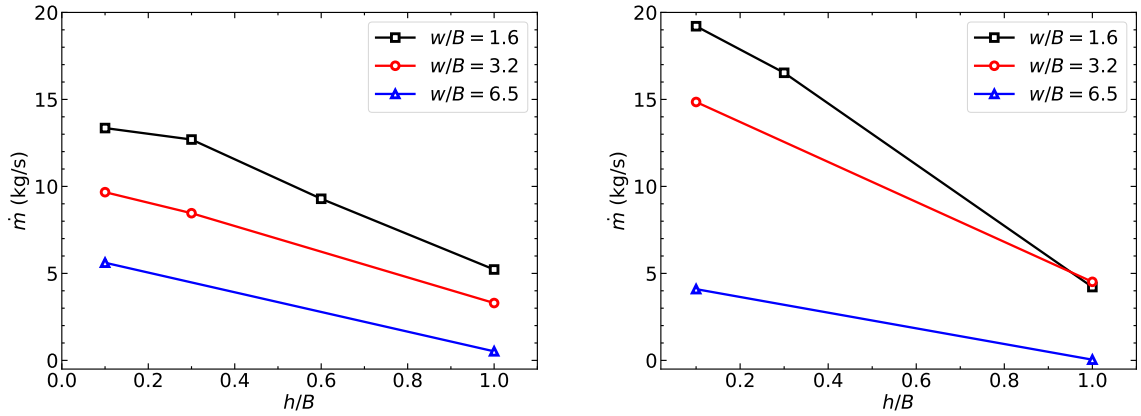

(a) $Fr = 0.6$ (b) $Fr = 1$

Figure 4.26: Overwash mass flux as a function of relative ice thickness.

$w/B = 1.6$ and $h/B = 0.1$, $\dot{m}' = 1.24$ indicates the overwash mass that is generated on each side of the ship for each ship length it traveled is equivalent to 124% of the ship displacement.

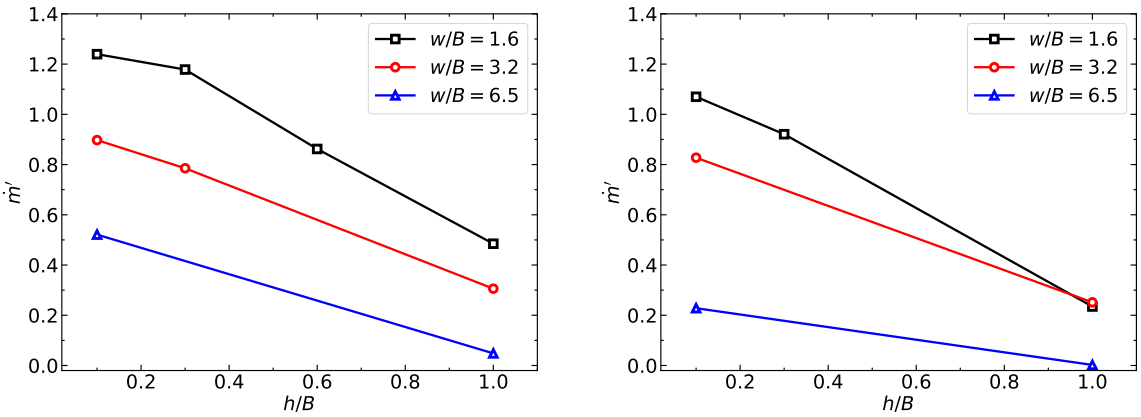

(a) $Fr = 0.6$ (b) $Fr = 1$

Figure 4.27: Normalized overwash mass flux as a function of relative ice thickness.

4.7 Summary

This chapter first discusses the typical ice thicknesses in the Arctic region and uses the knowledge of the relationship between ice flexure and critical speed to justify the

rigid-ice assumption. Since the investigated ship speeds are well below the critical speeds for the thick ice sheets studied in this chapter, the ice flexure is assumed to be sufficiently small (Xue et al., 2021) and it does not alter the velocity or wave fields near the ship. Therefore the ice sheet can be treated as rigid.

A grid refinement study is performed to determine the mesh resolution and open water tests are compared with experimental and CFD results from references for validation. Then CFD is used to study the wave resistance and wave pattern for the same idealized canal in Chapter III of constant width. Comparisons in wave resistance between the CFD simulations and theoretical analysis from Chapter III demonstrate a good agreement, which indicates the theory can provide fast and accurate estimations of wave resistance in canals with the knowledge of open-water wave resistance.

The analysis is extended to rigid ice sheets of constant thickness. By measuring the vertical distribution of the lateral momentum flux, it is demonstrated that the momentum flux is concentrated in a small region below the water surface, and nearly all the momentum flux occurs in the first 20% of the fundamental wavelength of the ship-generated waves. CFD simulations are performed to study ship transit in open water between rigid ice sheets and the results show that the wave fields in leads with ice thickness greater than 20% of λ are similar to those in corresponding canals, and so is the wave resistance, with an increase up to 74% and a decrease as much as 31% relative to the open-water conditions. Simulations with intermediate ice thickness show that the corresponding wave field and resistance are somewhere between that in open water and in a canal. This means that ship operations in a lead can realize substantial benefits, or penalties, to resistance and fuel consumption with a strong dependence on the ship speed, even in relatively thin ice conditions.

The last section of this chapter investigates the higher speed regime of $0.4 < Fr < 1.4$ with a planing hull model. The CFD results show that the ice thickness affects the ship resistance when the ship is sufficiently close to the ice. It is also shown that

narrower channels shorten the wave and produce a larger perturbation to the fluid velocity behind the ship. Overwash on top of the ice is observed for most cases and the overwash mass flux over the ice edge is mathematically defined and quantified. The amount of overwash is significant for thin ice and narrow channels as overwash mass equivalent to $> 120\%$ of the ship displacement is generated on each side of the ship for each ship length it traveled.

CHAPTER V

Ship Moving in a Lead between Flexible Ice Sheets

This chapter studies the problem of the full-scale ONRT traveling in a lead between thin ice sheets of 0.5 m $< h <$ 2 m. The ice sheets are treated as flexible as the investigated ship speeds of $0.2 < Fr < 0.4$ approach or exceed the theoretical critical speed, which is shown later in this chapter, and the ice deformation is non-negligible according to Xue et al. (2021). The interactions between the ship-generated waves and sheet ice are modeled by the FSI solver introduced in Sec 2.2. The FSI solver couples the moving fluid domain and the static ice sheet, where the fluid domain is modeled by the two-phase flow solver from Sec 2.1, and the flexible ice sheet is treated as a thin elastic plate. The ice sheet is subject to fluid stress and its deformation is solved by a linear dynamic modal decomposition method. This chapter first conducts convergence studies to determine the ice extent, finite element discretizations, and number of mode shapes, then analyzes ice deflections by performing a group of simulations with different ship speeds and ice thicknesses. Particularly, overwash is quantified and its influence on the ice responses is discussed.

5.1 Convergence Studies

Compared to the simulations with rigid ice, more numerical parameters associated with the structural domain are introduced in the simulations with flexible ice. These parameters need to be determined first. This section conducts convergence studies to examine the dependences of the solutions on the ice sheet dimensions, finite element discretization, and number of mode shapes. The test case has $Fr = 0.4, w/B = 2$ and $h = 1$ m.

5.1.1 Dependence on FE Domain Sizes

This work intends to investigate sheet ice that is of an infinite extent, whereas it is impractical to use a large number of finite elements to mimic an infinite ice sheet in numerical simulations. A sufficiently large FE domain with a finite number of FE is adopted instead and the dependence of the solutions on the FE domain sizes needs to be examined first. The length of the ice sheet is much larger (2,000 m in this case) and preliminary simulations show fluid and FE solutions are insensitive to the length. Therefore, only the width of the ice sheet is examined.

Table 5.1 collects the results of the maximum deflection of the ice, $w_{\max}$, average time period of the ice response, T_i, and the time of occurrence of the maximum deflection, $t_{\max}$, for different width values of ice plate, W. The results are recorded at a fixed probe on the ice edge at $x = 0$, which is initially next to the mid-ship. The table shows that for an ice sheet that is at least 200 m wide, the ice responses are invariant in terms of ice deflections. Even for a width of 140 m, the difference is smaller than 1%. Ice responses recorded at other probe locations demonstrate similar comparisons. Therefore an ice sheet of 2,000 m $\times$ 200 m is selected for the rest of the study.

Table 5.1: Convergence of maximum ice deflection for different widths of the ice sheets. The test case has $Fr = 0.4, w/B = 2$ and $h = 1$ m.

Width of ice sheet (m)	$w_{\max}$ (m)	$t_{\max}$ (s)
140	0.488	12.68
200	0.491	12.69
280	0.491	12.69

5.1.2 Dependence on FE Discretization

In the applied finite element method for discretizing the structure, the displacements at each node are interpolated with cubic shape functions and the rotations with quadratic shape functions. The higher-order interpolations bring solutions of higher accuracy for displacement within the elements. Hence fewer FE elements are required compared with the discretization for the fluid domain.

The resolution of the finite element discretization of the ice is examined by evaluating the ice deflections and axial stress. Three uniform Cartesian grids with different resolutions are used to discretize the ice sheet, which have 8, 16 and 32 thousand elements, corresponding to element sizes of $5\sqrt{2}$ m, 5 m and $5/\sqrt{2}$ m, respectively, with refinement ratios of $r_i = 2$, $\sqrt{2}$ and 1. Table 5.2 shows that a total number of 16 thousand elements is sufficient to give converged results, which has an element size of 5 m by 5 m.

Table 5.2: Convergence of maximum ice deflection and axial stress for different finite element discretization. The test case has $Fr = 0.4, w/B = 2$ and $h = 1$ m.

N_{FE} ($\times 10^3$)	$w_{\max}$ (cm)	$t_{\max}$ (s)	$\sigma_{\max}$ (MPa)	$t_{\max}$ (s)
8	0.464	12.66	1.85	15.44
16	0.491	12.69	1.93	15.36
32	0.493	12.71	1.95	15.36

5.1.3 Modal Convergence

The sheet ice is represented by a finite number of mode shapes with associated natural frequencies that are generated with FEM. A few example mode shapes of an ice sheet of $h = 0.5$ m are given in Figure 5.1, where the mode shapes are presented in the form of ice deflections. These presented mode shapes are selected based on the corresponding modal participation in the simulation with $Fr = 0.4$ and $h = 0.5$ m, which is plotted in Figure 5.2. Modal participation measures the significance of a vibration mode and is quantified in this work as the amplitude of the excited mode shapes. Larger values indicate a stronger contribution to the dynamic response of the ice deflections. As will be demonstrated in Figure 5.8, different ship speeds, or different ice mechanical properties, which are determined by ice thickness in this case, lead to different combinations of modal participation. The case with $Fr = 0.4$, $h = 0.5$ m is selected only for illustration purposes. From the mode shapes in Figure 5.1, we can see that the first several modes have simple deformation shapes with large wavelengths, and later modes have more complex deformation patterns with smaller wavelengths.

The number of mode shapes that are required to accurately represent the ice sheet is determined by examing the convergence on ice deflections. The time series of the ice deflections recorded at the fixed probe on the ice edge at $x = 0$ are shown in Figure 5.3 for different numbers of modes. Figure 5.3a shows the time histories of entire simulations and Figure 5.3b zooms in the time window near the occurrence of the maximum deflection. The maximum deflections are plotted in Figure 5.4 as a function of number of modes, where the maximum deflections are non-dimensionalized by that with 800 modes. This plot demonstrates that the deflections converge after around 200 modes.

(a) mode #1

(b) mode #9

(c) mode #46

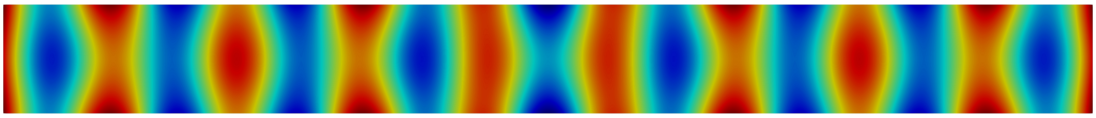

(d) mode #82

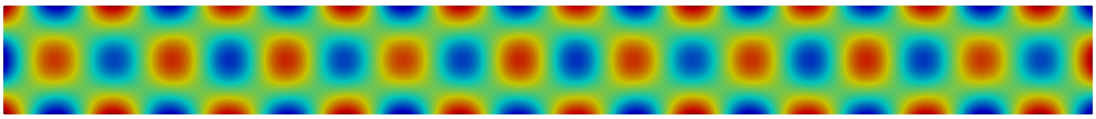

(e) mode #105

(f) mode #238

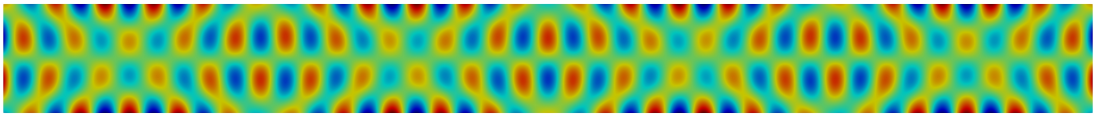

(g) mode #422

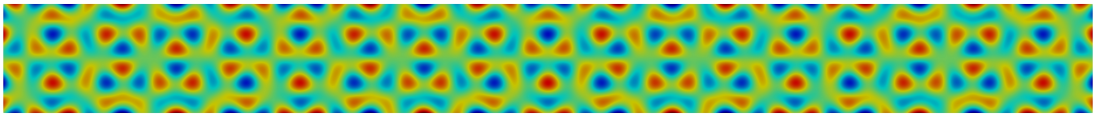

(h) mode #751

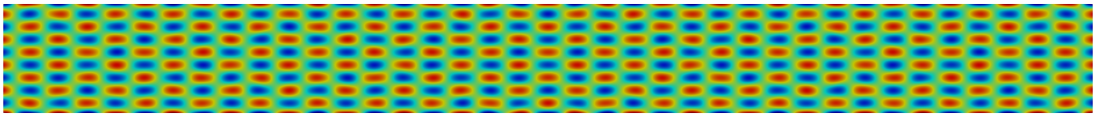

Figure 5.1: Individual mode shapes for an example ice sheet with dimensions of 2,000 m by 200 m, finite element resolution of 5 m, and $h = 0.5$ m. A total of 800 modes are used to describe the ice (788 effective). The ice sheet is colored by deflections, where the red and blue indicate positive and negative deflections, respectively.

Table 5.3: Convergence for different numbers of mode shapes.

N	$w_{\max}$ (m)	$t_{\max}$ (s)
10	0.009	13.64
20	0.030	13.79
50	0.161	13.86
100	0.372	13.30
200	0.455	12.79
400	0.494	12.75
565	0.492	12.69
800	0.491	12.69

Since stresses in the ice are proportional to the second derivatives of the ice deflections, it is supposed that more modes are required to reach a convergence than that for deflections. The relative maximum axial stress in the ice at steady state is plotted in Figure 5.5 as a function of the number of modes. Although the convergence behavior is not as ideal as for the deflections, using 400 modes is essentially adequate as it gives a stress of $< 1\%$ difference to that with 800 modes. 800 modes are used for the rest of the study.

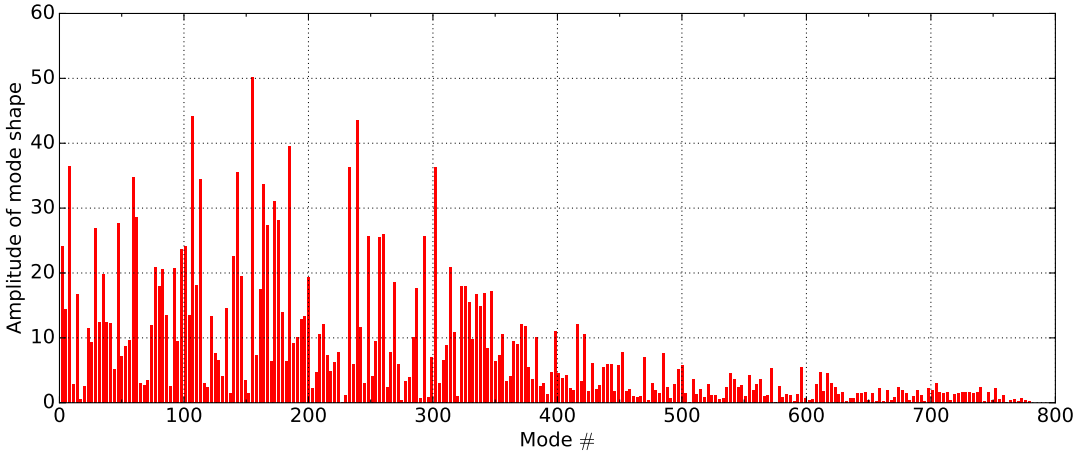

Figure 5.2: Modal participation presented in the form of amplitudes of excited mode shapes. $Fr = 0.4$, $h = 0.5$ m.

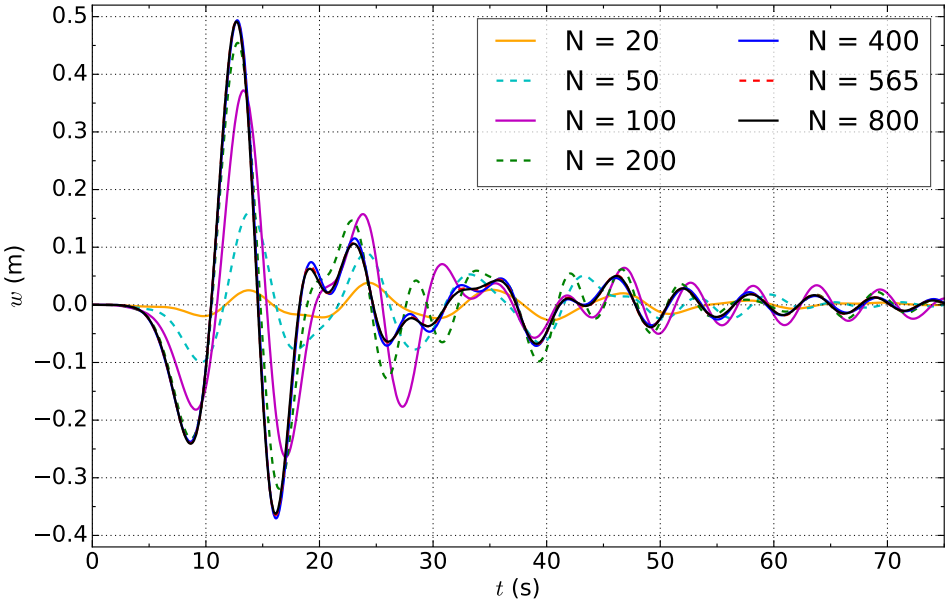

(a) entire simulation

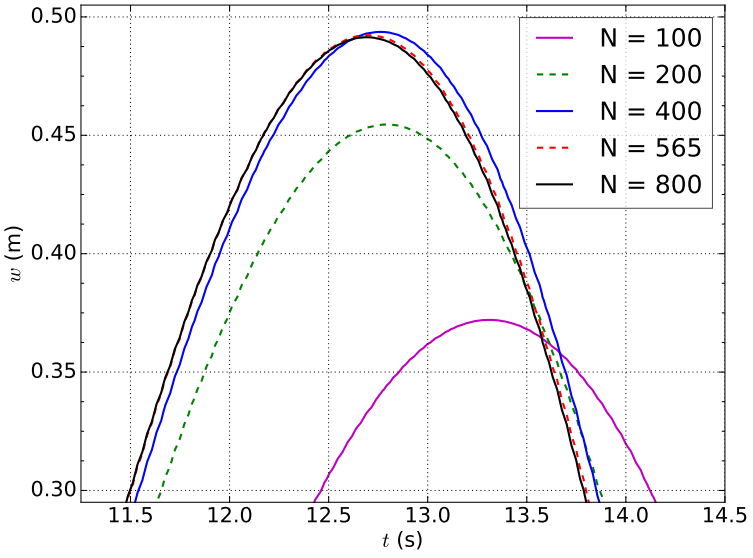

(b) near time of maximum deflection

Figure 5.3: Time series of deflections at a fixed location on ice with different numbers of mode shapes.

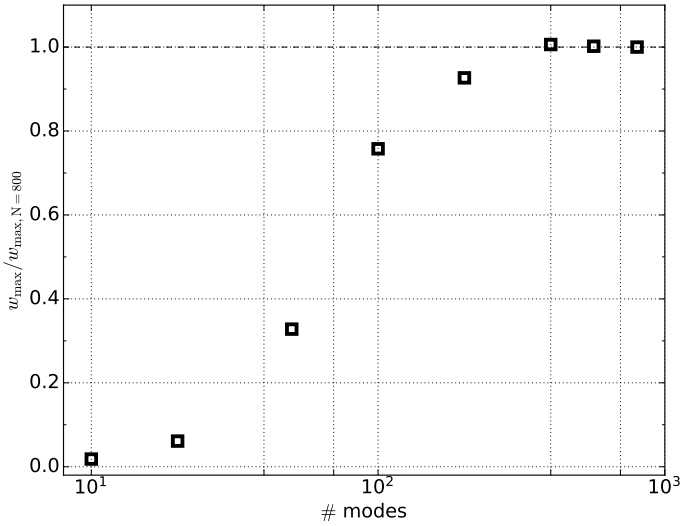

Figure 5.4: Convergence of modal description of ice plate for maximum deflection.

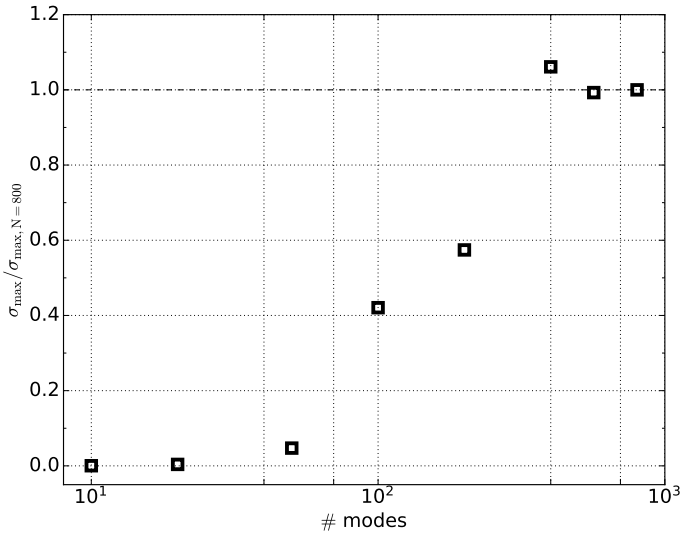

Figure 5.5: Convergence of modal description of ice plate for maximum stress.

5.2 Computational Results

5.2.1 Wave Fields and Ice Deflections

After determining the required ice dimensions, FE resolutions and number of modes, a group of simulations are performed with different ship speeds and ice thicknesses. Froude numbers $Fr = 0.2$, 0.33 and 0.4 are selected based on the theoretical and

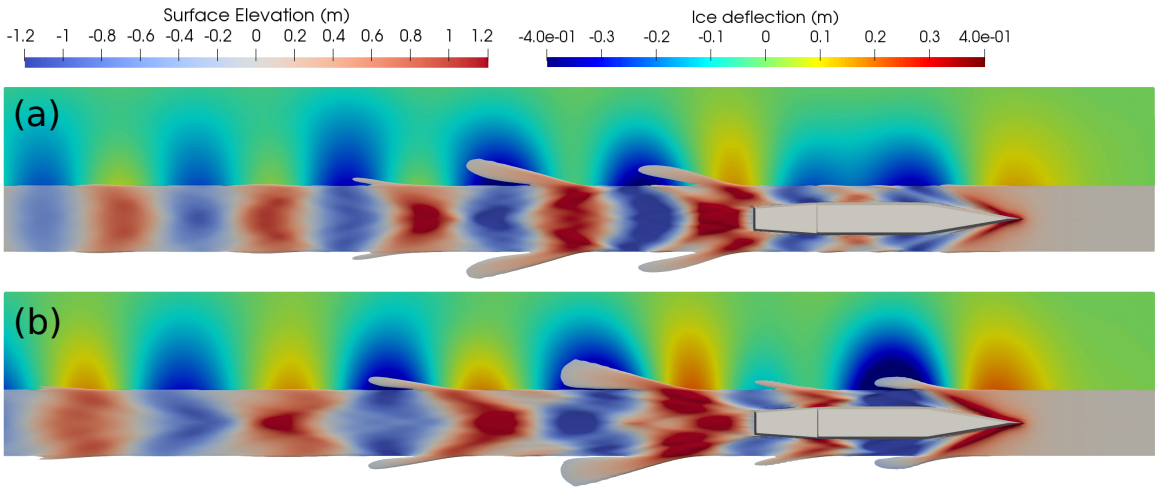

Figure 5.6: Steady-state wave fields and ice deflections for (a) $Fr = 0.33$ and (b) $Fr = 0.4$, $h = 1$ m.

numerical analysis in the previous two chapters. Three values of ice thicknesses are considered, which are $h = 0.5$ m that represents first-year ice, and $h = 1$ m and 2 m that represent medium thick multi-year ice. The channel width is set constantly as $w = 2B$ to limit the parameter space. All simulations are run for sufficiently long until they reach a steady state for both the wave fields and ice deflections in the ship-fixed coordinate system.

Steady-state wave fields and ice deflections within the CFD domain are displayed in Figure 5.6 for $h = 1$ m and Figure 5.7 for $h = 0.5$ m. Note that the ice sheets on two sides are symmetric about the centerline of the channel and only one side is displayed. One salient feature is that the ice deflections in the ship track direction have similar wavelengths to the ship-generated waves in the downstream, and the in-ice and in-water waves are generally in phase with each other, which is more clearly demonstrated by the wavecuts at the ice edge in Figure 5.14. Because the lower ship speed has a smaller fundamental wavelength, the waves in the ice for $Fr = 0.33$ are also shorter than those for $Fr = 0.4$. As these patterns are in steady-state, we also know that the waves travel with the ship at the same speed. The ice deflections are larger near ice edges and decay further away, which have similar patterns with

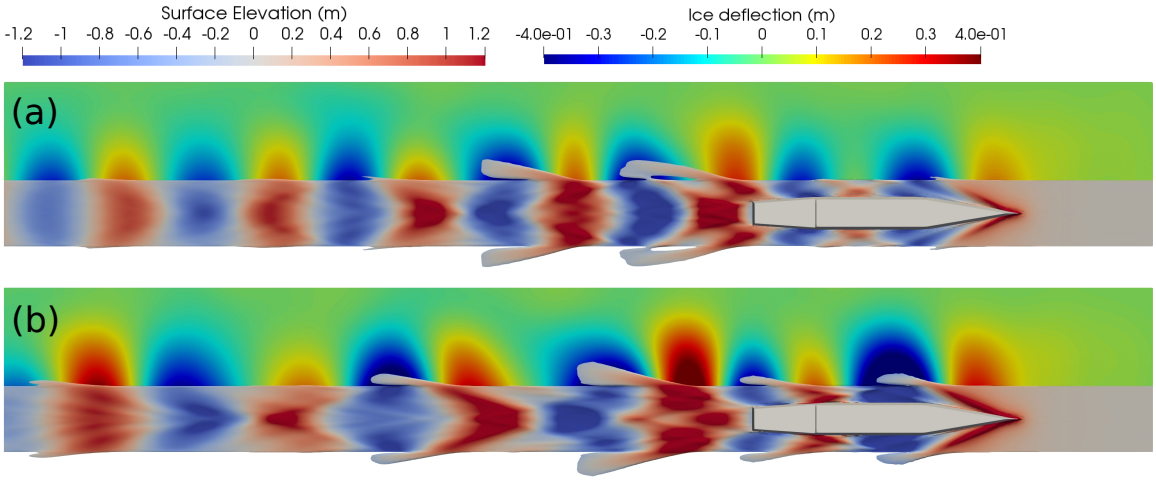

Figure 5.7: Steady-state wave field and ice deflections for (a) $Fr = 0.33$ and (b) $Fr = 0.4$, $h = 0.5$ m.

the hydrodynamic pressure acting on the lower surface of the ice sheet. Another important feature is the overwash on top of the ice. The green water flows on top of the ice at the water wave crests, which forms the overwash. The green water spreads on the ice surface and is trapped in the hollow (downward deflected ice) between two humps (upward elevated ice). The fluid stress due to the overwash is supposed to depress the ice sheet and is accounted for in the present solver.

The modal participation levels for different test conditions are presented in Figure 5.8 in the form of amplitudes of excited mode shapes. The amplitudes are plotted on a logarithmic scale to more clearly display the small-value range at the higher-frequency end (larger mode #). For all conditions, mode shapes with lower frequencies (smaller mode #) generally have larger amplitudes than those of higher frequencies, which means the former is excited to higher participation levels. The comparisons of different ship speeds and ice thicknesses show that the higher-frequency modes participate more for higher ship speeds and thinner ice.

The ice deflections can be affected by several factors including the ice rigidity, fluid stress on the lower surface of the ice sheet, and fluid stress due to overwash water. The latter two quantities can vary as the ice sheets of different thicknesses have different

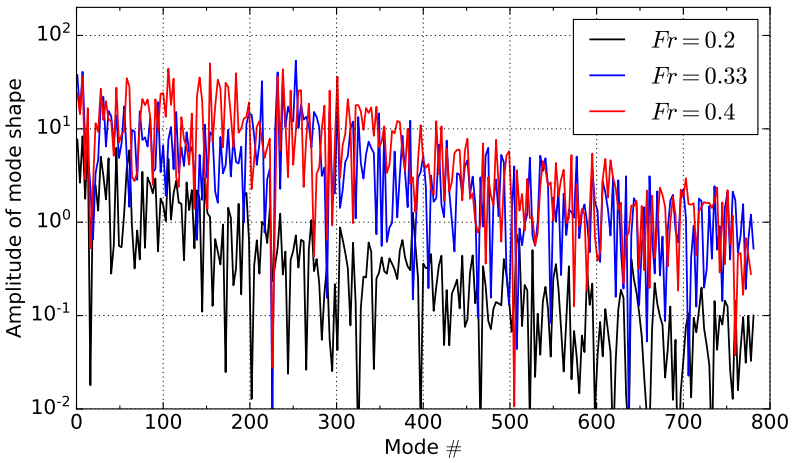

(a) different Froude numberes, $h = 0.5$ m

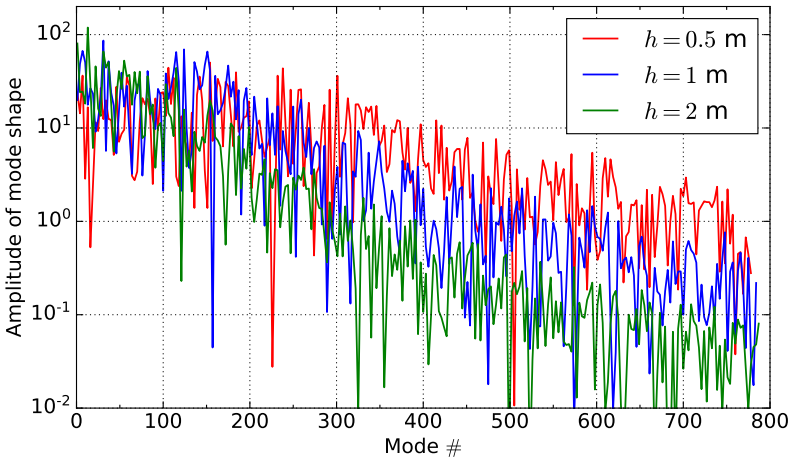

(b) different ice thicknesses, $Fr = 0.4$

Figure 5.8: Modal participation presented in the form of amplitudes of excited mode shapes, $w = 2B$.

drafts (90% h) and freeboards (10% h). Ice deflection itself can affect the overwash amount, which will be discussed in Section 5.2.2. But the most important factor is the rigidity of the ice sheet, $D = Eh^3/12(1+\nu^2)$, which is proportional to the cube of the ice thickness.

Since the ice edge has the largest deflections, the deflections along the ice edges are plotted together for comparison for different ship speeds in Figure 5.9a and different ice thicknesses in Figure 5.9b. Note the midship is located at $x/L = 0$, and the bow

and stern are respectively located at $x/L \approx 0.5$ and ≈ -0.5. The undisturbed profile of ice edge deflections ($\omega = 0$) is also indicated. Figure 5.9a demonstrates that the ice deflections increase with the ship speed. Ice deflections are much smaller for the lower ship speed of $Fr = 0.2$ than the two higher ship speeds. For all ship speeds, the larger ice deflections mostly occur in the near field and diminish into the far field as the water waves are attenuated or canceled in the downstream. Figure 5.9b shows the ice deflections along ice edges for the same Froude number $Fr = 0.4$ but with different ice thicknesses. The wavelength and phase of the ice deflections are similar for the three different ice thicknesses. With increasing ice thickness, the deflections decrease and the downward shift of the entire ice edge due to the weight of the overwash water becomes more significant.

The ice deflections away from the ice edge ($y = 4B$) are also examined in Figure 5.10 to see how the ice deflections are attenuated in the lateral direction. The deflections for the thinnest ice of $h = 0.5$ m become the smallest among all three ice sheets, whereas it has the largest deflections at the ice edge. This means the attenuation in ice deflections in the lateral direction is most significant with the thinnest ice. The slower attenuation is assumed to attribute to the higher rigidity of the thicker ice.

The maximum values of deflection of the entire ice sheet at steady state ($\omega_{\max}$) are plotted in Figure 5.11 as a function of Froude number. The maximum deflections for both ice thicknesses increase with ship speed. At the lowest speed of $Fr = 0.2$, the two ice sheets have similar maximum deflections of 84 and 71 mm. The discrepancy in $\omega_{\max}$ widens as the ship speed increases, but the ratio of the two values remains at around 0.8. At $Fr = 0.4$, the thicker ice has $\omega_{\max} = 0.61$ m and the thinner one has $\omega_{\max} = 0.78$ m. Note all the maximum deflections recorded have a negative sign (downward deflection), which is due to the overall downward shift of the ice sheet caused by the fluid weight of overwash.

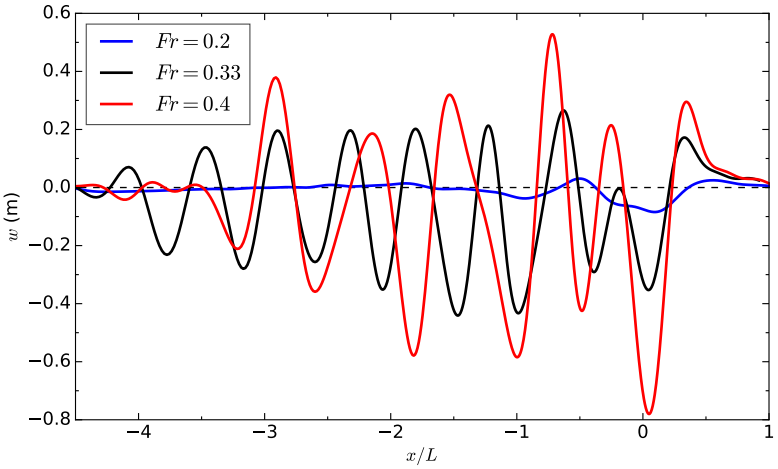

(a) different ship speeds, $h = 0.5$ m

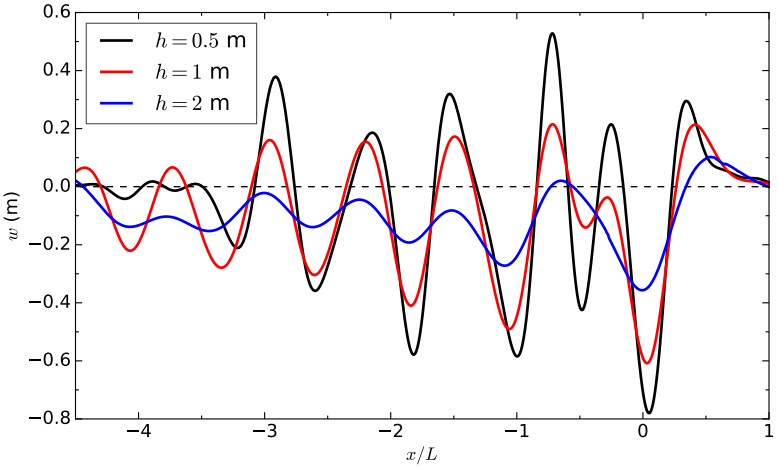

(b) different ice thicknesses, $Fr = 0.4$

Figure 5.9: Steady-state ice deflections along edges.

By using the expression in Equation 4.1 that determines the critical speed in deep water for ice of infinite extent, the critical speeds for the two ice sheets of $h = 0.5$ m and $h = 1$ m are 15.4 m/s and 11.9 m/s, or $Fr = 0.4$ and $Fr = 0.31$ for the full-scale ONRT, respectively. The theoretical critical speeds for the two ice thicknesses are indicated by the vertical dashed lines in the figure. According to Xue et al. (2021), the deformation grows rapidly and reaches a maximum as the speed is increased towards the critical speed. For $h = 0.5$ m, it can be determined that the real critical speed is over the theoretical critical speed of $Fr = 0.31$, but it is not clear if it reached critical

speed between $Fr = 0.35$ and 0.4 from Figure 5.11. Another indicator for reaching the critical speed is the generation of flexural-gravity waves that propagate upstream. No perceivable waves are captured in the upstream, which indicates the critical speed has not been reached. Higher speeds or thinner ice sheets that have larger deflections are not investigated as body-fitted meshes are used for the ice surfaces in this work and the mesh distortion caused by the ice deformation (> 0.8 m) is too large compared to the small cell height around the ice edge (< 0.5 m), which is beyond the capability of the present solver.

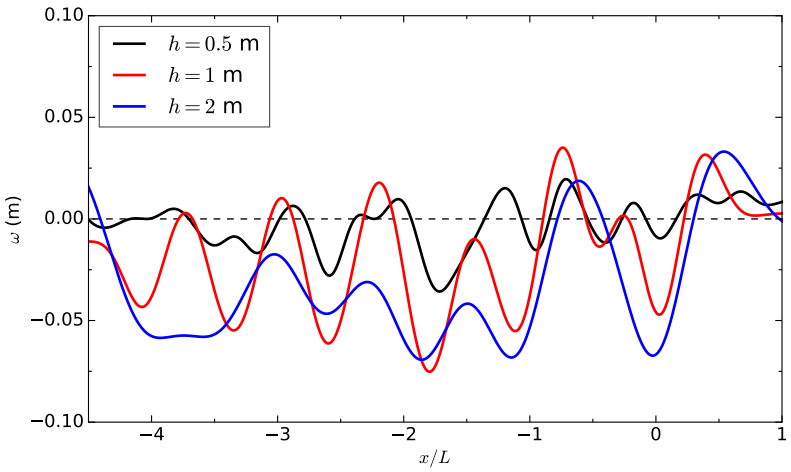

Figure 5.10: Steady-state deflections at $y = 4B$ m with different ice thickness. $Fr = 0.4$, $w = 2B$.

Figure 5.12 shows the frequency analysis of the ice deflections at two fixed probes, i.e. one at the ice edge ($y = B$) and another away from the ice edge at $y = 4B$, and both at $x = 0$. In Figure 5.12a, all three thicknesses have two significant peaks with the first one near the zero frequency that has a very long period, which is due to forces of long wavelengths (could be the overwash). The second peaks are a little over 0.63 rad/s, which indicates the ice deflections are mostly compliant with the ship waves that have a theoretical frequency of 0.631 rad/s by deep water dispersion relation. Larger frequencies indicate the in-ice waves are shortened compared to the water waves in open water, which phenomenon was also reported in the in-situ observations

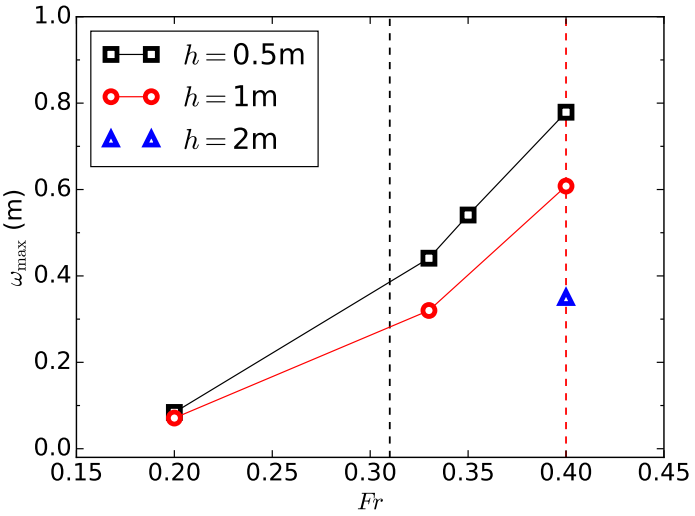

Figure 5.11: Absolute maximum deflection of the ice sheet as a function of Froude number. The theoretical critical speeds for the two ice thicknesses are indicated by the vertical dashed lines of corresponding color.

by Dumas-Lefebvre and Dumont (2021). The curves for the thinner ice sheets are slightly shifted to the right (though the comparisons are compromised by the coarse resolutions of the spectra), which means waves in thinner ice are shorter compared with thicker ice. Further away from the ice edge, as shown in Figure 5.12, the wave energy drops for all three cases. But attenuation is much more significant for thinner ice, which is consistent with that demonstrated in Figure 5.10.

5.2.2 Overwash Mass Flux

Overwash over the top surface of the ice sheet is a significant phenomenon in these simulations. The overwash mass flux over the ice edge is evaluated in a similar form as in Eq. 4.10 with only changing the lower vertical integration limit to the deflected top surface of the ice edge $z = \omega(x, w/2)$

$$\dot{m} = \int_{\omega(x,w/2)}^{\xi(x,w/2)} \int_{x_B}^{x_A} \rho v \; dxdz, \quad \text{for } \xi(x, w/2) > \omega(x, w/2) \tag{5.1}$$

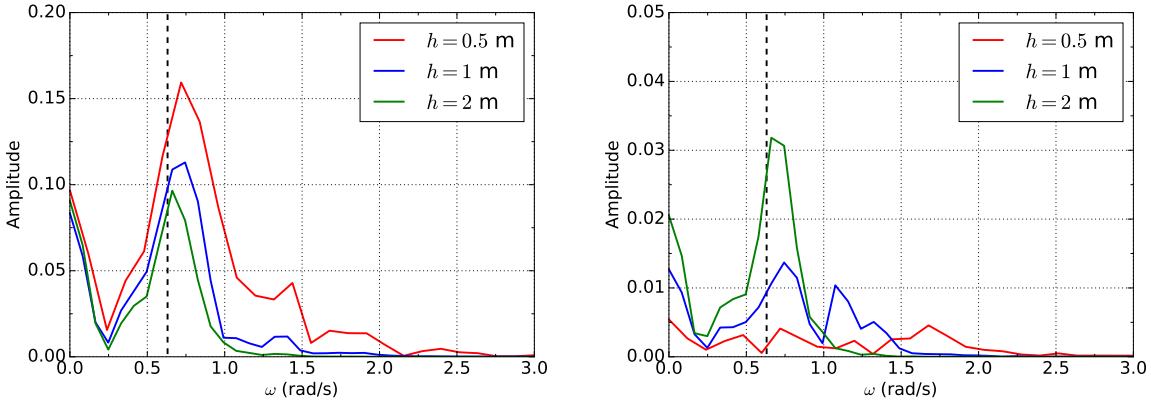

(a) probe at ice edge, $x = 0$

(b) probe at $y = 4B$, $x = 0$

Figure 5.12: Angular frequencies of the ice deflections at two fixed probes for various ice thicknesses. For the cases of $Fr = 0.4$ and $w = 2B$. The vertical dashed lines indicate the theoretical frequency ($\omega_T = 0.631$ rad/s) of pure transverse waves for $Fr = 0.4$ in open water.

and is normalized in the same way as in Eq. 4.11, $\dot{m}' = \dot{m}L/mU$, where $m = 8507$ ton is the displacement of the full-scale ONRT.

The overwash mass flux is plotted in Figure 5.13 against Froude number along with the normalized values. For $Fr = 0.2$, the $\dot{m}$ values for the two ice thicknesses are similar with the thinner ice allowed slightly more overwash. But for higher speeds of $Fr = 0.33$ and $Fr = 0.4$, the thicker ice of $h = 1$ m has more overwash than the thinner ice with considerable differences. The two-meter thick ice has even higher $\dot{m}$ for $Fr = 0.4$.

Thicker ice allowing more overwash may be unexpected as thicker ice has a higher freeboard (10% of ice thickness) that is supposed to block more lateral flow flux above the calm water surface. This may be explained by the compliance of thin ice to water waves. Figure 5.14 plots the elevation profiles of both the water waves and both the top and bottom surfaces of the deformed ice sheet along the ice edge. Note the undeformed upper surfaces sit respectively at $z = 0.05$ m and 0.2 m for the two ice sheets of $h = 0.5$ m and 2 m. The wave elevations at the ice edge are generally similar for the two conditions. The thinner ice is more compliant and has larger ice flexure

at the ice edge, and the humps (upward deflections of ice) are generally in phase with the crests of the water waves, which results in smaller wave elevation relative to the top of the ice edge. Overwash occurs where the wave elevation is higher than the top of the ice edge, i.e. $\xi(x, w/2) > \omega(x, w/2)$. These occurrences are indicated by the red shades in the figure, from which it is evident that the elevated edge of the thinner ice blocks more overwash. On the other hand, the flexure is much smaller for the thicker ice and is not totally in phase with the wave elevations, especially in the near field. This allows more overwash, despite its higher freeboard. Note possible air ventilation can happen under the ice near the mid-ship for $h = 0.5$ m as the wave profile falls below the bottom of the ice edge.

To more clearly demonstrate that ice rigidity plays a significant role in determining the overwash amount, a set of comparison simulations were performed with completely rigid ice, i.e. ice with infinite rigidity. The overwash mass flux $\dot{m}$ is plotted in Figure 5.15 for different ship speeds with both flexible ice ($E = 4.2$ GPa) and rigid ice of $h = 0.5$ m. For each ship speed, the rigid ice overwhelmingly overtops the flexible ice with more than twice of overwash as for the flexible ice.

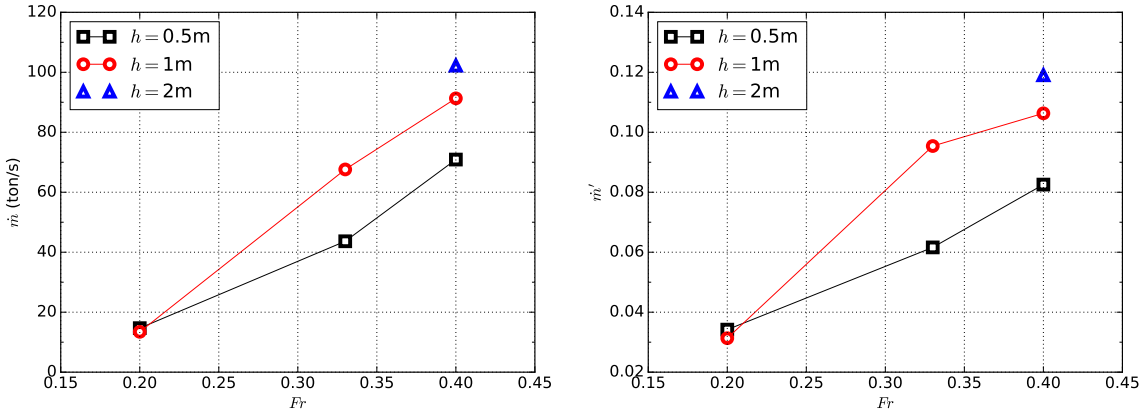

(a) original values

(b) normalized values

Figure 5.13: Overwash mass flux as a function of ship speed.

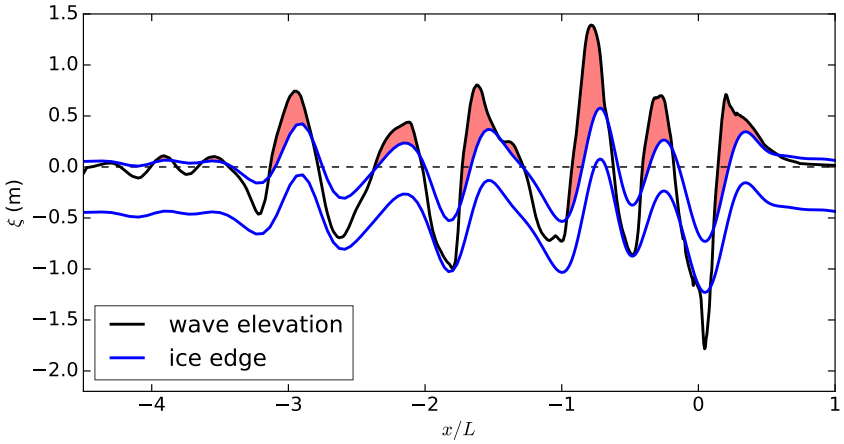

(a) $Fr = 0.4$, $h = 0.5$ m

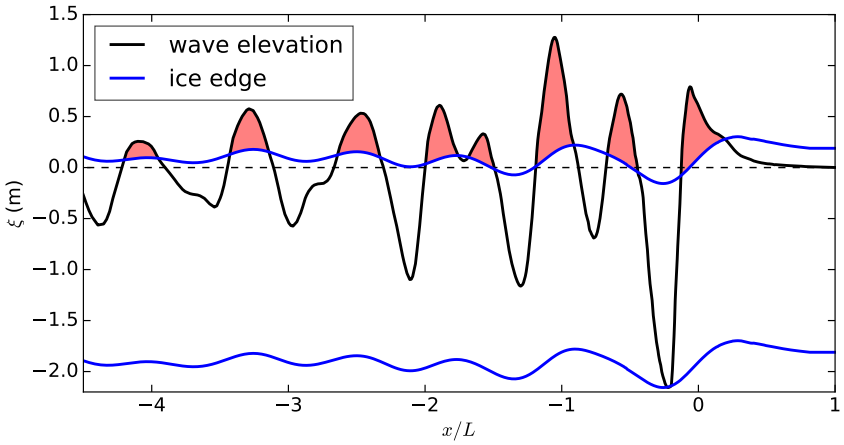

(b) $Fr = 0.4$, $h = 2$ m

Figure 5.14: Elevation profiles of water wave and both the top and bottom surfaces of the ice sheet along the ice edge. The red shades indicate where overwash occurs. Midship is at $x/L = 0$.

5.2.3 Effect of Ice Flexure

This section compares the simulations with either flexible or rigid ice sheet to see how ice flexure influences the ship hydrodynamics and wave fields.

Section 5.2.2 already demonstrated that assuming ice being rigid can lead to more overwash in certain conditions. Figure 5.16 plots the steady-state wave fields with the rigid ice of $h = 0.5$ m, which can be compared with those with flexible ice in Figure 5.7. The patterns of green water on top of the ice are different from those

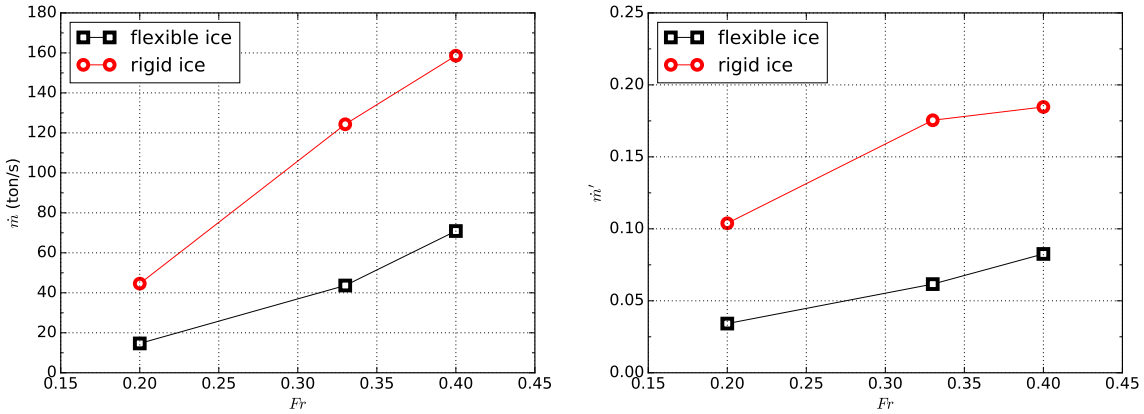

(a) original values (b) normalized values

Figure 5.15: Overwash mass flux as a function of ship speed with either flexible or rigid ice, $h = 0.5$ m.

with flexible ice. Since the upper surface of rigid ice is flat, the green water spreads out more freely compared with that on deformed ice.

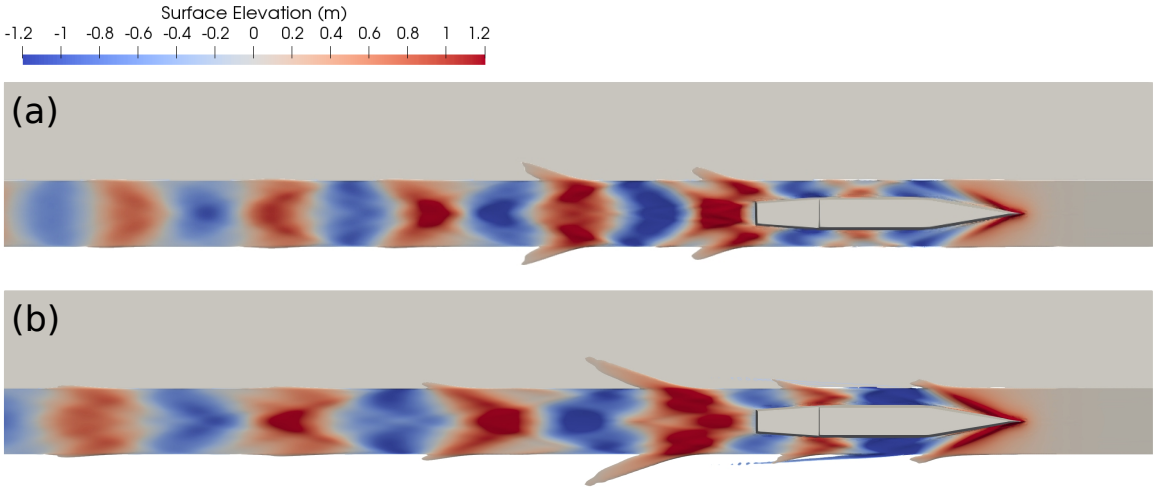

Figure 5.16: Steady-state wave fields with rigid ice for (a) $Fr = 0.33$ and (b) $Fr = 0.4$, both have $h = 0.5$ m.

The wave fields between the ice sheets are similar for the flexible and rigid ice. To more clearly demonstrate the comparison, wavecuts through the centerline of the channel are plotted in Figure 5.17. For the lower ship speed of $Fr = 0.2$, the wave profiles are almost identical in the near field up to 1.5 ship-length after the stern,

only minor differences occur after $x/L = -1.5$. Similarly, for $Fr = 0.33$, only minor differences exist in wave amplitude after $x/L = -1$ while the wavelengths and phases are similar. Notable differences happen in the case of $Fr = 0.4$, especially for wave elevations after $x/L \approx -3$. In the downstream after $x/L = -3$, amplitudes of the water waves with the flexible ice decreased dramatically, compared to the gradual attenuation with the rigid ice.

The wave resistance relative to that in open water for different ship speeds is collected in Table 5.4, where the relative resistance is compared between either a rigid or flexible ice sheet is present, both have a thickness of 0.5 m. No significant differences are found in the comparison of the resistance between rigid and flexible ice assumptions, where assuming the ice is flexible only leads to 0.9%, 0.4% and 1.8% increase in resistance for $Fr = 0.2$, 0.33 and 0.4, respectively.

Table 5.4: Relative resistance (R_p/R_0) with rigid and flexible ice sheet of $h = 0.5$ m. The last column is the ratio of wave resistance with flexible ice to that with rigid ice.

Fr	Flexible ice	Rigid ice	Ratio
0.2	1.002	0.993	1.009
0.33	1.141	1.137	1.004
0.4	0.694	0.682	1.018

5.2.4 Discussion on Stress and Potential Fracture

In this work, ice is assumed to be homogenous and the ice sheet is treated as a continuous and thin elastic plate. The structural model is able to evaluate the stress in the ice based on the deformation of the ice sheet and other properties of the ice. However, this work does not model ice fracture since even with treating the ice as plastic material, the failure criteria for sea ice are still inconclusive (Untersteiner, 2013; Weiss et al., 2007). Without modeling the ice fracture, the current solver is able to continue the simulation beyond the failure point of the ice sheet. This section

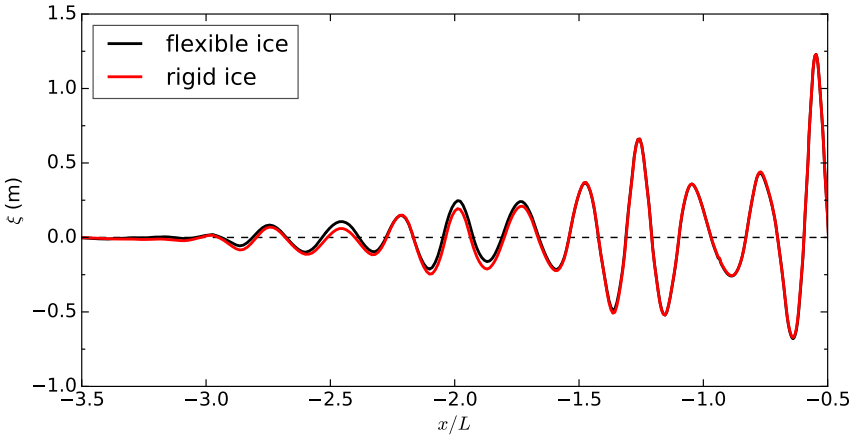

(a) $Fr = 0.2$

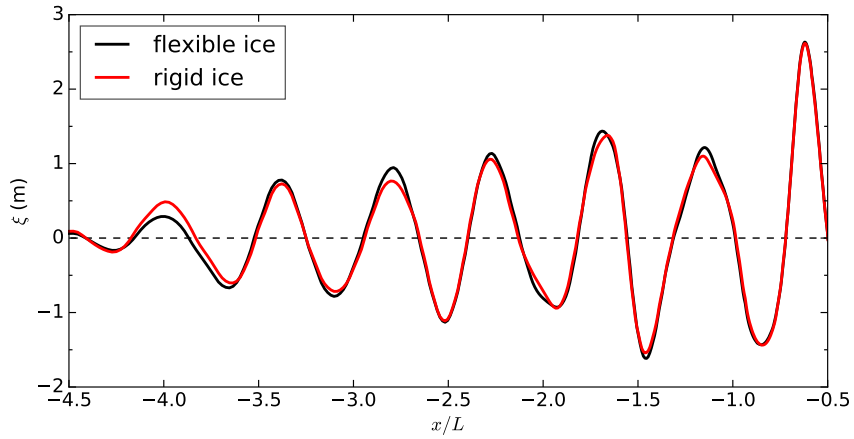

(b) $Fr = 0.33$

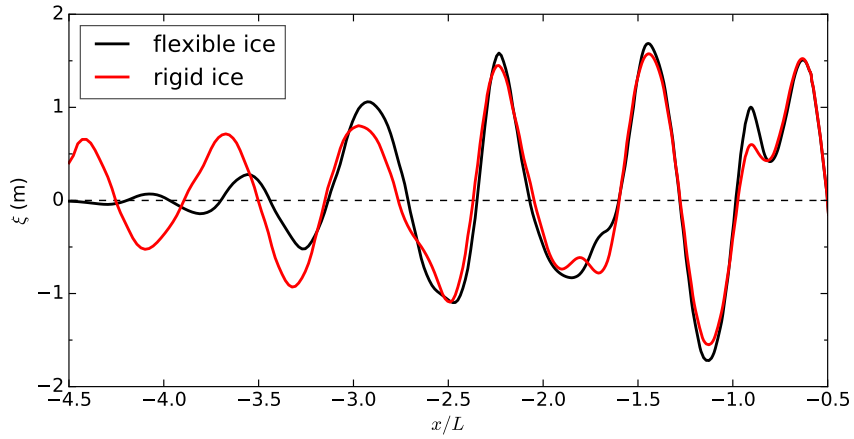

(c) $Fr = 0.4$

Figure 5.17: Comparison between flexible and rigid ice for wave profiles along the centerline of the channel with midship placed at $x/L = 0$. Ice thickness is $h = 0.5$ m.

discusses the stress in the ice and identifies potential ice fracture by using the Mohr-Coulomb (MC) criterion (Gross and Seelig, 2017).

The von Mises stress describes the distortion energy per unit volume and is evaluated as

$$\sigma_e = \sqrt{\sigma_1^2 - \sigma_1\sigma_2 + \sigma_2^2}, \tag{5.2}$$

where σ_1 and σ_2 are the principal stresses and can be calculated using axial stresses. Figure 5.18 shows the distribution of von Mises stress on the ice surface for different ship speeds with $h = 1$ m. Similar to the deflection patterns, the largest stresses concentrate along the ice edge. The stresses dissipate quickly away from the ice edge with only a fraction ($< 5\%$) of maximum σ_e at $y \approx 5\ B$. Compared to the higher speeds, the stresses in the ice with $Fr = 0.2$ are much smaller and concentrate near the moving hull. Note the range of the color map for $Fr = 0.2$ is a magnitude smaller than that for the two higher ship speeds.

The Mohr-Coulomb criterion is used to examine potential fractures in the ice. The fracture criterion depends on both the compressive strength σ_c and tensile strength σ_t of sea ice. This work uses the values of $\sigma_c = 3$MPa and $\sigma_t = 0.5$ MPa for the ice, which are from the empirical formulae reported by Timco and Weeks (2010) and have been used in Montiel and Squire (2017) and Montiel and Mokus (2022) for modeling sea-ice breaking. The steady-state stresses on the top and bottom surfaces of the ice sheets with different test conditions in Figure 5.18 are sampled at points along the ice edge ($y = B$), $y = 2B$, $3B$, and $4B$ with a longitudinal distance of 1 m apart. The stresses are plotted in the space of the principal stresses, σ_1 and σ_2, in Figure 5.19. The red curve, $\mathcal{F}(\sigma_1, \sigma_2) = 0$, is the Mohr-Coulomb yield criterion, where the symbols outside of the curve indicate failure. The points on the ice edge are highlighted with blue color.

For the lowest tested speed $Fr = 0.2$, all the sampled points are under low stresses and are well within the yield curve, which indicates the ice sheet is not likely to

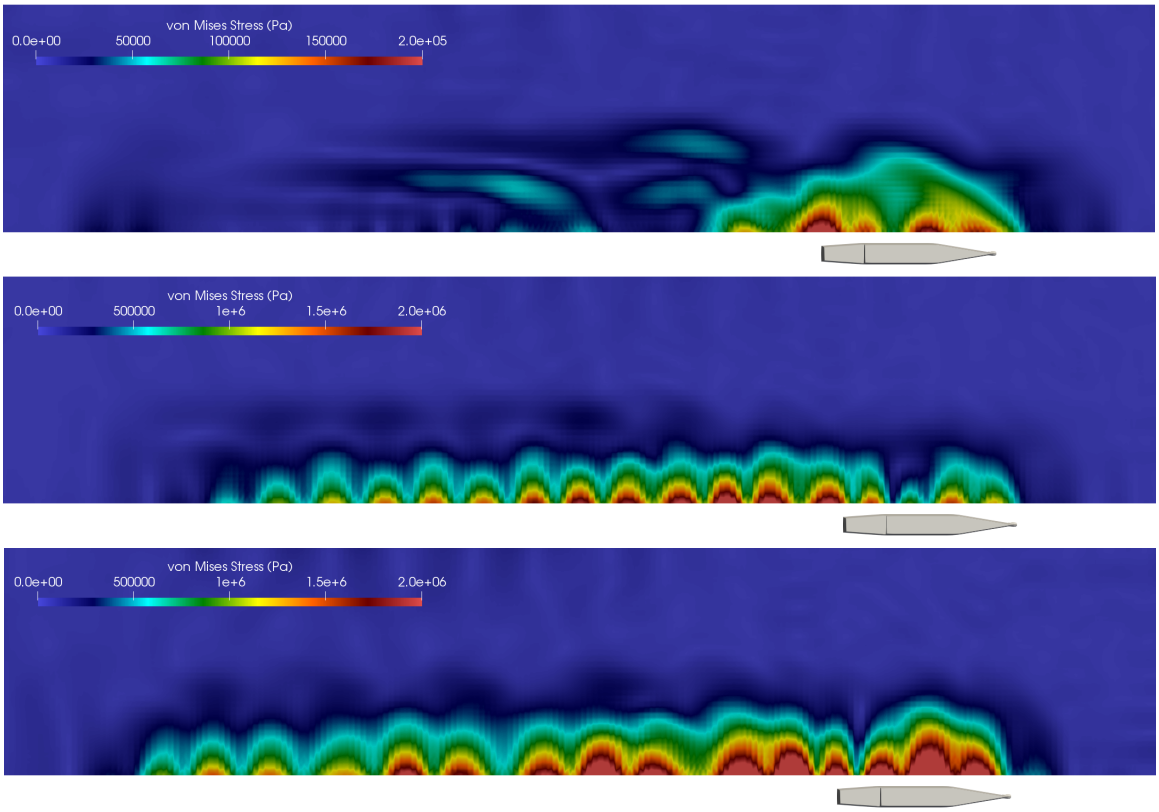

Figure 5.18: Steady-state von Mises stress across the ice surface for $Fr = 0.2$, 0.33 and 0.4 from top to bottom. Other conditions are $h = 1$ m, $w = 2B$.

fracture. For the speed $Fr = 0.33$, the symbols significantly spread out and a small amount of them fall outside of the yield curve, though most are still inside the curve and are around the origin. Most of the outside symbols fall in the first quadrant of the principal stresses, which indicates potential tensile failure. The symbols in blue are further away from the origin compared to those in black, which means the ice edge is under higher stresses and is more likely to break. Similarly, for $Fr = 0.4$, most outside points are in the first quadrant and are likely to have tensile failure, while a few in the third quadrant indicate potential pure compressible failure and all of them are located on the ice edge.

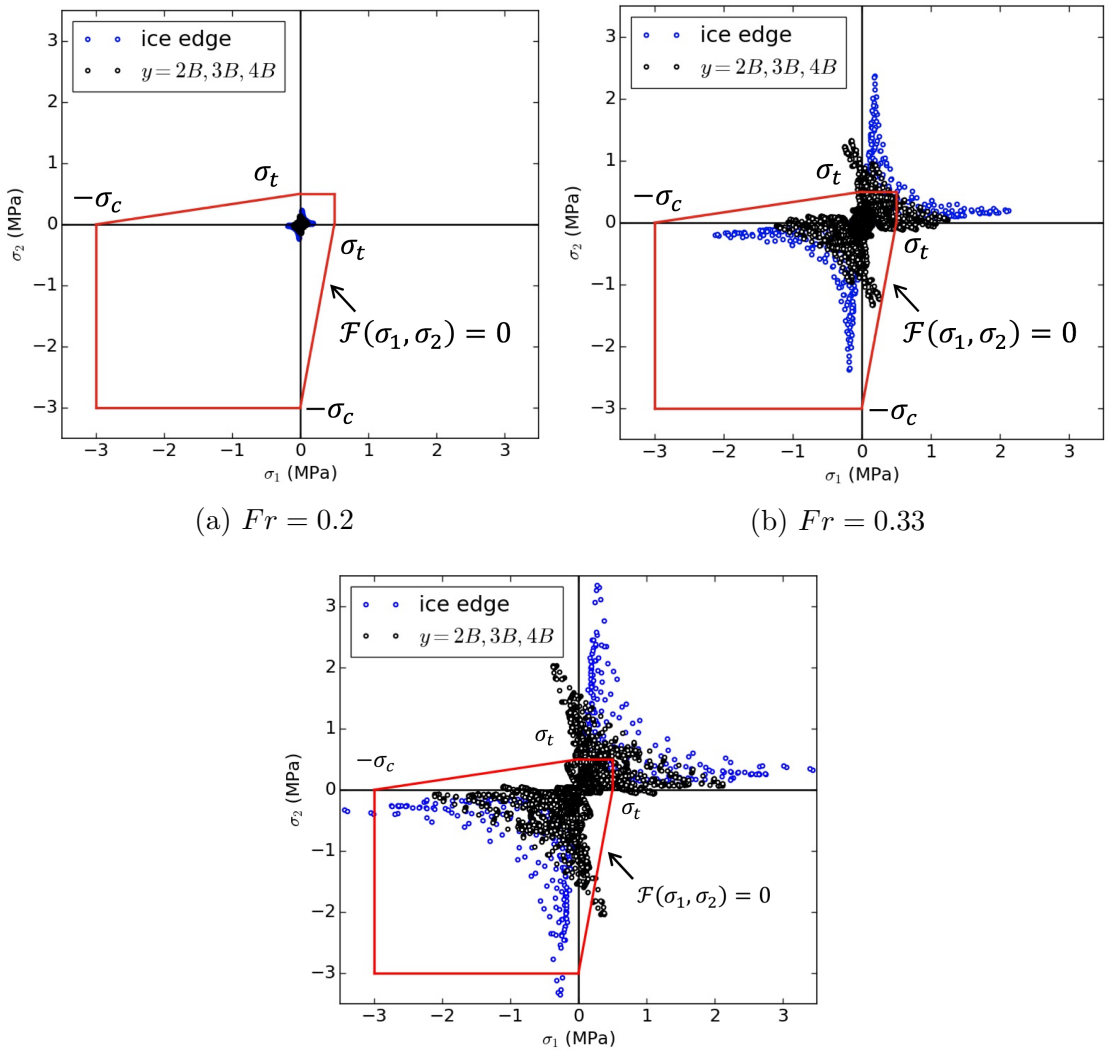

(a) $Fr = 0.2$

(b) $Fr = 0.33$

(c) $Fr = 0.4$

Figure 5.19: Sampled stresses on the ice surfaces with different ship speeds. Ice thickness is $h = 1$ m. The Mohr-Coulomb yield criterion, $\mathcal{F}(\sigma_1, \sigma_2) = 0$, is indicated by the red curve with empirical values of compressive strength $\sigma_c = 3$ MPa and tensile strength $\sigma_t = 0.5$ MPa for the sea ice.

5.3 Summary

This chapter investigates the problem of a ship moving in a lead between thin and flexible ice sheets. Convergence studies are conducted to determine the lateral extensions of the ice sheet, finite element discretizations, and number of mode shapes to represent the ice. Then a group of simulations are performed with Froude numbers of

$Fr = 0.2$, 0.33 and 0.4, ice thicknesses of $h = 0.5$ m, 1 m and 2 m, and a fixed channel width of $w/B = 2$. The ice deflections are found to have similar wavelengths and are in phase with the ship-generated waves downstream. Maximum ice deflections of the entire ice sheet $\omega_{\max}$ always occur at the ice edge and are usually near the hull, which increase with ship speed and decrease with ice thickness. Within the investigated range of ship speed $0.2 < Fr < 0.4$, the moving ship has not reached the critical speed based on the observed maximum ice deflections and absence of flexural-gravity waves traveling upstream. Shortening of in-ice waves is found by comparing the angular frequencies of waves in water and ice, where the thinnest ice is found to have the smallest wavelength.

Overwash on top of the ice is another significant phenomenon and greatly affects ice behaviors. The ice sheets have an overall downward shift that is caused by the weight of green water on top of the ice, which results in all maximum ice deflections observed being downward deflections. Overwash mass flux is calculated to quantify the overwash intensity. The flux is found to increase with ship speed but also increase with ice thickness, whereas the latter finding is unexpected as one would think a higher freeboard allows less lateral mass flux. The rigidity is found to be the primary factor by comparing the relative elevation of the water waves to the top ice edge. The thinner ice is more compliant with the water waves so the elevated ice edge blocks more lateral flux at the wave crests, while the less compliant thicker ice has smaller deflections that are not totally in phase with the water waves so it allows more lateral flux where the relative wave elevation is large, even with higher freeboard. Simulations with rigid ice but otherwise the same setups generate more than twice overwash compared with the flexible ice, which confirms the above analysis.

The wave fields with either rigid or flexible ice are compared for different ice thicknesses. Perceptible differences can be only found in the far field downstream for thinner ice sheets, while the near fields are similar for rigid and flexible ice. Less than

2% of differences are found in wave resistance between either a rigid or flexible ice sheet is present.

This chapter also discusses the stress in the ice and identifies potential ice fractures by using the Mohr-Coulomb criterion with empirical values of compressive and tensile strength for sea ice. It is found most distortion energy concentrates on the ice edge and quickly dissipates away from the ice edge. When the ship moves at $Fr = 0.2$ in the open-water ice channel with $w = 2B$ and $h = 1$ m, the stresses in the ice are much lower than those when the ship moves at $Fr = 0.33$. For $Fr = 0.2$, all the sampled points are well within the Mohr-Coulomb yield curve, indicating fractures are unlikely. Potential tensile failure is identified for $Fr = 0.33$ and 0.4. A few points on the ice edge are found to have potential compressive failure for $Fr = 0.4$.

CHAPTER VI

Conclusions and Future Work

6.1 Summary

The sea-ice coverage in the Arctic region is rapidly evolving and this polar region sees increased maritime activities each year. Much of previous research for ship activities in this polar region has focused on ice-breaking operations that are limited to low speeds. While the Arctic has already been used for tourism, military and rescue that will seek to travel at higher speeds. Yet there lacks of research on high-speed ship transit in icy conditions. This dissertation investigates the ship-wave-ice interactions for the problem of ship transit in open-water ice channels with high-resolution CFD models, where a high speed range of $0.2 < Fr < 1.4$ is studied. The questions of what happens to the ship hydrodynamics and how the ice responds to the ship wake as the ship speed and channel conditions change throughout transit are addressed.

To investigate the problem of ship transit in a lead, two numerical solvers are employed for modeling the two-phase flows and wave-ice interactions. A customized CFD solver based on OpenFOAM is applied to model the two-phase flows. URANS equations are solved for both the water and air, where the VOF approach is used to capture the moving interface. A deformable mesh technique is applied to enable mesh deformation around the hull surface due to the heave and pitch. Customized changes are made to separate mesh motions and enable directional scaling to facilitate

simulations with a moving hull and static ice sheets. An FSI solver adapted from Piro and Maki (2013) and Piro (2013) is employed to model the interactions between the ship-generated waves and flexible ice sheets. The problem consists of a moving fluid domain and a static structure domain, i.e. the ice sheet. The fluid domain is modeled by the two-phase flow solver but assumes laminar flow for the flexible-ice problem. The ice sheet is represented by a finite number of uncoupled mode shapes that are generated by FEM and the ice deflections are governed by the equation of a thin elastic plate. Grid matching between the two domains is executed at each time step to facilitate data exchange on the mutual interface. The fluid domain solutions and structural responses are tightly coupled and are solved in an iterative manner with an under-relaxation strategy to help reach convergence.

Before the numerical investigations into the lead condition, Chapter III first uses theoretical analysis of the far-field wave patterns to study the wave resistance of a ship traveling in a deep-water canal, which can be regarded as open water between ice sheets of infinite thickness. The purpose is to make the relationship between operation in a canal and transit in water bounded by adjacent sheet ice and then use the knowledge from operation in a canal to develop understanding of Arctic transit. Theoretical analysis based on Tuck and Lazauskas (1998) and Faltinsen (2005) for multi-hull vessels is adapted to analyze a single ship in a canal. The changes of the wave resistance relative to that in open water are analyzed with respect to the ship speed and canal width. It is found that significant increase or decrease in wave resistance can happen with increases up to +129% and decreases up to −82% relative to the open water condition, depending on both the ship speed and canal width. The wave resistance is decomposed into portions due to transverse and divergent waves, where strong correlation between the importance of divergent waves and reduced wave resistance is found for the ship speed $Fr \approx 0.35$. The dominance of the transverse or divergent waves is explained by the fundamental wavelength and cancellation of

bow-generated and stern-generated waves. Spectral analysis of the wave elevations recorded in towing-tank experiments that were conducted by a student team also confirms the dominance of transverse and divergent waves at two different ship speeds.

The problem of a ship moving in a lead between thick ice sheets is studied in Chapter IV with CFD. Since the investigated ship speeds are well below the critical speeds for the thick ice, the ice flexure is assumed to be sufficiently small according to Xue et al. (2021), therefore the ice sheet is treated as rigid in this chapter. The wave resistance and wave pattern of the full-scale ONRT model for the same idealized canal in Chapter III of constant width are studied with CFD simulations. Comparisons of wave resistance between the CFD simulations and theoretical analysis from Chapter III demonstrate good agreement, which indicates the linear theory can provide fast and accurate estimations of wave resistance in canals with the knowledge of open-water wave resistance. Analysis on the momentum flux and CFD simulations in the speed range of $0.2 < Fr < 0.4$ suggest that ice sheets that are thicker than 20% of the fundamental wavelength function nearly as canal walls. Simulations with intermediate ice thickness show that the corresponding wave field and resistance are somewhere in between that in open water and in a canal. This means that operation of ships in a lead can realize substantial benefits, or penalties, to resistance and fuel consumption with a strong dependence on the ship speed, even in relatively thin ice conditions. The higher speed range of $0.4 < Fr < 1.4$ is investigated with a planing hull model, where the CFD results show that the ice thickness affects the ship resistance when the ship is sufficiently close to the ice. The amount of overwash is found to be significant for thin ice and narrow channels as overwash mass equivalent to $> 120\%$ of the ship displacement is generated on each side of the ship for each ship length it traveled.

The problem of a ship traveling in a lead between thin and flexible ice sheets is studied in Chapter V with the FSI solver. Convergence studies are conducted

to determine the ice extensions, finite element discretizations, and number of mode shapes. Then a group of simulations are performed for Froude numbers of $Fr = 0.2$, 0.33 and 0.4, and ice thicknesses of $h = 0.5$ m, 1 m and 2 m. The ice deflection is found to have similar wavelengths and is generally in phase with the ship-generated waves. Maximum ice deflections of the entire ice sheet $\omega_{\max}$ always occur at the ice edge and are usually near the hull, which increase with ship speed and decrease with ice thickness. Overwash on top of the ice is a significant phenomenon and greatly affects the ice behaviors. The ice sheets have an overall downward shift that is caused by the fluid stress due to the green water on top of the ice. Overwash mass flux is found to increase with ship speed but also increase with ice thickness, whereas the latter is unexpected as the higher freeboard of thicker ice is thought to allow less lateral mass flux. The smaller relative wave elevation due to the compliance of the thin ice is found to be the primary reason: the thinner ice is more compliant with the water waves so the elevated ice edge blocks more lateral flux at the wave crests. The wave field and wave resistance with either rigid or flexible ice are compared for different ice thicknesses, where the near fields appear to be similar and differences in wave resistance are found to be $< 2\%$. This chapter also discusses the stress in the ice and identifies potential ice fractures by using the Mohr-Coulomb criterion with empirical values of compressive and tensile strength for sea ice. Tensile failure is more likely to happen as the sea ice is assumed to have a much lower tensile strength than its compressive strength due to its brittle nature. Potential tensile failure is identified for both $Fr = 0.33$ and 0.4. Potential compressive failure is found at a few locations along the ice edge for $Fr = 0.4$.

6.2 Key Contributions

The contributions of this dissertation are highlighted here, along with descriptions of their importance in the field of hydrodynamic analysis of high-speed Arctic transit.

- The major contribution of this work is its investigations into high-speed ship transit ($0.2 < Fr < 1.4$) in open-water ice channels, which is becoming an increasingly common scenario as leads are created by ocean currents or ice-going vessels, but has not been studied before. Through momentum flux analysis and CFD simulations, this work obtains that ice sheets thicker than 20% of the fundamental wavelength function nearly as canal walls. The CFD results also suggest that operation of ships in a lead can realize substantial benefits or penalties to resistance depending on both the ship speed and channel width. These conclusions can be useful for estimations of fuel consumption, emissions, time of transit, and logistical planning for Arctic transit.

- This work also applies theories of wave pattern analysis for multi-hull vessels to analyze a single ship in a canal. The theoretical analysis finds the relative wave resistance with different ship speeds and canal conditions. The contributions of transverse and divergent waves to the wave resistance are also decomposed to use the wave patterns to further explain the changes in wave resistance. With the established connection between thick ice and canal walls, the relation between the theoretical results and CFD of ship transit in a canal is made such that the analysis from the theoretical model can be used to elucidate ship operations in a lead with ice sheets of finite thickness. Therefore, the expensive CFD can be complemented by the faster and more affordable theoretical analysis.

- To the author's knowledge, this is the first numerical work on ship transit in a lead between flexible ice sheets. Hydroelastic responses of thin flexible ice sheets to ship-generated waves, the corresponding wave patterns and ship hy-

drodynamics, are investigated with the use of an adapted FSI solver. Maximum ice deflections are identified for different ship speeds and ice thicknesses. Overwash is a significant phenomenon and greatly affects the ice behaviors. The overwash effects are included in this study and its mass flux rate is investigated in detail. This work also examines the effects of assuming the ice is rigid or flexible on the wave fields and wave resistance.

- Another important contribution is the development of numerical models for studying high-speed ship transit in leads. An OpenFOAM-based CFD solver is adopted to model the two-phase flows with customized changes being made to separate mesh motions and enable directional scaling for mesh morphing to facilitate simulations with a moving hull and static ice sheets. The CFD solver is validated against experiments and is shown to have a good order of accuracy. The present model is proven to be a valuable tool for numerical investigations of high-speed ship transit in open-water ice channels. An adapted FSI solver is used to model the interactions between ship wakes and flexible ice sheets. The model matches a moving fluid domain with a large static ice sheet at each time step to tightly couple the CFD and structure domain such that using a large CFD domain can be avoided and the problem can be simulated at an affordable cost. The Kirchhoff hypothesis is used such that the 3D ice sheet can be modeled by a 2D shell through the mid-surface and then customized changes to the grid matching algorithm are made to include the effects of overwash on the ice hydroelasticity. These numerical models with the setup details could be used for reference for future numerical work on this problem.

6.3 Future Work

This dissertation investigated the problem of high-speed ship transit in open-water ice channels with theoretical and numerical approaches. The author hopes future work can be inspired and use this dissertation as a starting point. Recommendations for future research are summarized as follows, which mostly concern the simulations with flexible ice sheets

- This work assumes laminar flows for simulations with flexible ice sheets, where the assumption has its limitations. Development of turbulent models that can be integrated with the modal decomposition method in the FSI solver is necessary for accurate predictions of ship-wave-ice interactions, especially when wave breaking is involved.

- Grid matching between the moving fluid domain and static ice sheet is time-consuming, which takes up nearly half of the overall CPU time, even after optimizations in running speed have been made. The current algorithm for grid searching and matching loops all finite elements or wet elements at each time step with a time complexity of $\mathcal{O}(n * m)$, where n is the number of finite elements and m is the number of fluid faces on ice within the CFD domain. Using a more efficient matching algorithm is necessary. Also, the current solver runs in parallel for the CFD part but only the master processor is utilized for grid matching and FE domain solutions. Enabling parallel computing for grid matching can substantially reduce the computation time and cost, which is worth trying.

- More realistic sea ice can be considered in future work with appropriate continuum models for governing ice behaviors. For instance, this work models the ice sheet as a thin elastic plate, which describes many features of sea ice behaviors and is suitable for large rigidity, but ice viscosity should be considered for thin-

ner ice with smaller rigidity. The visco-elastic model, taking the KelvinVoigt model for example, considers the ice viscosity by adding a dissipation term in the governing equation for ice deflections, has been successfully applied for studying continuous ice covers (Shishmarev et al., 2016, 2019; Khabakhpasheva and Korobkin, 2021) and should be considered in future research.

APPENDIX A

Experiments with Perforated Spherical Shells

The experiments and all the measurements were conducted at the Aaron Friedman Marine Hydrodynamics Laboratory by a student team, the team members are L. Victoria Arciniega, Logan Galindo and Jackson Brown, and supervised by the laboratory director Professor Kevin J. Maki. The author would like to thank all of them for providing the data and pictures for this analysis and presentation.

Experiments were performed in a towing tank to study the wave attenuation by a field of floating pancake ice (Arciniega et al., 2023). Figure A.1 depicts the schematic of the experiment setups including the location of the wave probe. As demonstrated in the left picture of Figure A.2, a model scale ONRT hull with a ship length of $L = 3.14$

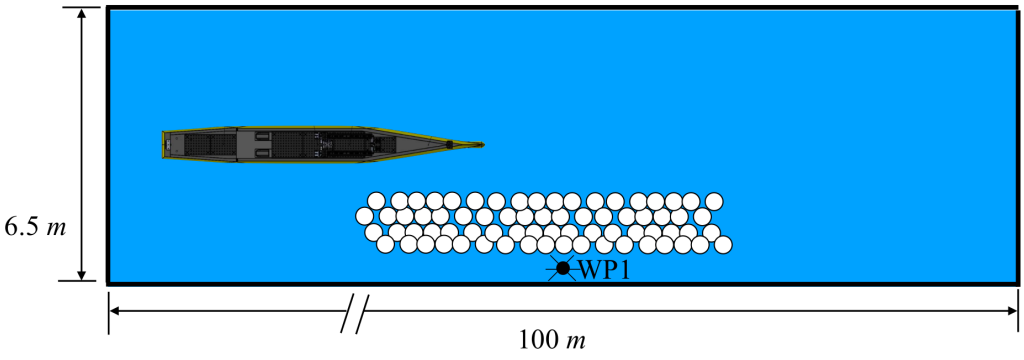

Figure A.1: Schematic of the experiment facility (not to scale). WP1 indicates the location of the wave probe.

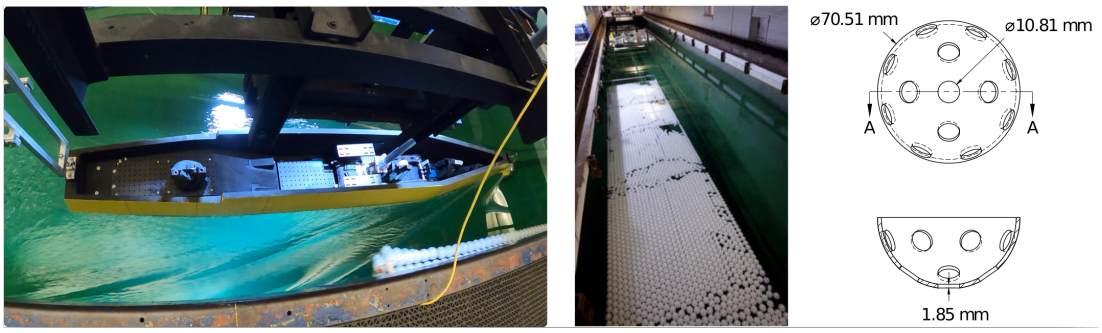

Figure A.2: From left to right are (left) Snapshot of the ship model traveling at a constant speed of $Fr = 0.29$, (middle) image of the raft consisting of Whiffle balls, (right) drawing of the perforated spherical shell.

m was towed at constant speeds passing near the ice, where the ship-generated waves propagate and interact with the floating ice. Perforated spherical shells, which are commonly known as Whiffle balls, were used as surrogates for pancake ice. Around 7,000 Whiffle balls were placed together to form a raft that resembles the marginal ice zone (MIZ) featured by a field of broken ice floes (see the middle picture in Figure A.2). A schematic of the Whiffle ball is shown on the right of Figure A.2, the ball has a diameter of $D = 70.51$ mm and a shell thickness of 1.85 mm. The ball has 26 holes of diameter 10.81 mm. The material is made of polyethylene and has a density of 930 kg/m^3, which is close to that of sea ice.

The ship model was also towed without the Whiffle balls, which can be regarded as an open-water condition. Wave elevations were recorded by the wave probe for different ship speeds and are analyzed on the frequency domain by applying FFT on the time sequences. The spectral analysis is presented in III to confirm the contributions of transverse and divergent waves to the wave resistance at different ship speeds.

BIBLIOGRAPHY

Arciniega, L. V., Galindo, L., and Maki, K. J. (2023). Wave dissipation in a field of floating perforated spherical shells. 38th IWWWFB.

Bai, W., Zhang, T., and McGovern, D. J. (2017). Response of small sea ice floes in regular waves: A comparison of numerical and experimental results. *Ocean Engineering*, 129:495–506.

Bennetts, L. and Williams, T. (2015). Water wave transmission by an array of floating discs. *Proceedings of the Royal Society A: Mathematical, Physical and Engineering Sciences*, 471(2173):20140698.

Chen, X.-N. and Sharma, S. D. (1997). Zero wave resistance for ships moving in shallow channels at supercritical speeds. *Journal of fluid mechanics*, 335:305–321.

Cook, S. S. (2011). *Effects of headwinds on towing tank resistance and PMM tests for ONR Tumblehome*. PhD thesis, The University of Iowa.

Council, A. (2009). Arctic marine shipping assessment 2009 report.

Dalrymple, R. A. (1974). A finite amplitude wave on a linear shear current. *Journal of Geophysical Research*, 79(30):4498–4504.

Doctors, L. J., Day, A. H., and Clelland, D. (2008). Unsteady effects during resistance tests on a ship model in a towing tank. *Journal of ship research*, 52(04):263–273.

Dumas-Lefebvre, E. and Dumont, D. (2021). Aerial observations of sea ice break-up by ship waves. *The Cryosphere Discussions*, pages 1–26.

Eça, L. and Hoekstra, M. (2014). A procedure for the estimation of the numerical uncertainty of cfd calculations based on grid refinement studies. *Journal of computational physics*, 262:104–130.

Faltinsen, O. M. (2005). *Hydrodynamics of High-Speed Marine Vehicles*. Cambridge University Press.

Farhat, C., Lesoinne, M., and Le Tallec, P. (1998). Load and motion transfer algorithms for fluid/structure interaction problems with non-matching discrete interfaces: Momentum and energy conservation, optimal discretization and application to aeroelasticity. *Computer methods in applied mechanics and engineering*, 157(1-2):95–114.

Fox, C. and Squire, V. A. (1994). On the oblique reflexion and transmission of ocean waves at shore fast sea ice. *Philosophical Transactions of the Royal Society of London. Series A: Physical and Engineering Sciences*, 347(1682):185–218.

Gross, D. and Seelig, T. (2017). *Fracture mechanics: with an introduction to micromechanics*, pages 45–49. Springer.

Guo, C.-y., Xie, C., Zhang, J.-z., Wang, S., and Zhao, D.-g. (2018). Experimental investigation of the resistance performance and heave and pitch motions of ice-going container ship under pack ice conditions. *China Ocean Engineering*, 32(2):169–178.

Hansen, C. Ø., Grønsedt, P., Graversen, C. L., and Hendriksen, C. (2016). *Arctic shipping: commercial opportunities and challenges*. CBS Maritime.

Havelock, T. (1965). *The collected papers of Sir Thomas Havelock on hydrodynamics*, volume 103, pages 391–393. Office of Naval Research, Department of the Navy.

Higuera, P., Lara, J. L., and Losada, I. J. (2013). Realistic wave generation and active wave absorption for navier–stokes models: Application to openfoam®. *Coastal Engineering*, 71:102–118.

Hirt, C. W. and Nichols, B. D. (1981). Volume of fluid (vof) method for the dynamics of free boundaries. *Journal of computational physics*, 39(1):201–225.

Howell, S. E. and Yackel, J. (2004). A vessel transit assessment of sea ice variability in the western arctic, 1969–2002: implications for ship navigation. *Canadian Journal of Remote Sensing*, 30(2):205–215.

Huang, L., Li, M., Romu, T., Dolatshah, A., and Thomas, G. (2021a). Simulation of a ship operating in an open-water ice channel. *Ships and Offshore Structures*, 16(4):353–362.

Huang, L., Li, Z., Ryan, C., Ringsberg, J. W., Pena, B., Li, M., Ding, L., and Thomas, G. (2021b). Ship resistance when operating in floating ice floes: Derivation, validation, and application of an empirical equation. *Marine Structures*, 79:103057.

Huang, L., Ren, K., Li, M., Tuković, Ž., Cardiff, P., and Thomas, G. (2019). Fluid-structure interaction of a large ice sheet in waves. *Ocean Engineering*, 182:102–111.

Huang, L., Tuhkuri, J., Igrec, B., Li, M., Stagonas, D., Toffoli, A., Cardiff, P., and Thomas, G. (2020). Ship resistance when operating in floating ice floes: A combined cfd&dem approach. *Marine Structures*, 74:102817.

Jacobsen, N. G., Fuhrman, D. R., and Fredsøe, J. (2012). A wave generation toolbox for the open-source cfd library: Openfoam®. *International Journal for numerical methods in fluids*, 70(9):1073–1088.

Jasak, H. (1996). *Error analysis and estimation for the finite volume method with applications to fluid flows*. PhD thesis, Imperial College London (University of London).

Keller, J. B. (1998). Gravity waves on ice-covered water. *Journal of Geophysical Research: Oceans*, 103(C4):7663–7669.

Khabakhpasheva, T. and Korobkin, A. (2021). Blunt body impact onto viscoelastic floating ice plate with a soft layer on its upper surface. *Physics of Fluids*, 33(6):062105.

Kim, M.-C., Lee, S.-K., Lee, W.-J., and Wang, J.-y. (2013). Numerical and experimental investigation of the resistance performance of an icebreaking cargo vessel in pack ice conditions. *International Journal of Naval Architecture and Ocean Engineering*, 5(1):116–131.

Kwok, R. (2018). Arctic sea ice thickness, volume, and multiyear ice coverage: losses and coupled variability (1958–2018). *Environmental Research Letters*, 13(10):105005.

Landrum, L. and Holland, M. M. (2020). Extremes become routine in an emerging new arctic. *Nature Climate Change*, 10(12):1108–1115.

Lee, E., Weil, C. R., and Fullerton, A. (2017). Experimental results for the calm water resistance of the generic prismatic planing hull (gpph): Nswccd-80-tr-2017/015. *Naval Surface Warfare Center Carderock Division*.

Leiviskä, T., Tuhkuri, J., and Riska, K. (2001). Model test on resistance in ice-free ice channels. In *Proceedings of the International Conference on Port and Ocean Engineering Under Arctic Conditions*.

Li, F., Suominen, M., and Kujala, P. (2021). Ship performance in ice channels narrower than ship beam: Model test and numerical investigation. *Ocean Engineering*, 240:109922.

Li, Z., Shi, Y., and Wu, G. (2017). Interaction of wave with a body floating on a wide polynya. *Physics of Fluids*, 29(9):097104.

Li, Z. and Wu, G. (2021). Hydrodynamic force on a ship floating on the water surface near a semi-infinite ice sheet. *Physics of Fluids*, 33(12):127101.

Lu, P., Li, Z., Zhang, Z., and Dong, X. (2008). Aerial observations of floe size distribution in the marginal ice zone of summer prydz bay. *Journal of Geophysical Research: Oceans*, 113(C2).

Luo, W.-Z., Guo, C.-Y., Wu, T.-C., and Su, Y.-M. (2018). Experimental research on resistance and motion attitude variation of ship–wave–ice interaction in marginal ice zones. *Marine Structures*, 58:399–415.

Maki, K., Zhang, Z., Korobkin, A., Khabakhpasheva, T., Marleaux, P., and Abdel-Maksoud, M. (2022). Viscoelastic response of level ice to ship wakes. In *Proceedings of the 9th International Conference on Hydroelasticity in marine technology*.

Maman, N. and Farhat, C. (1995). Matching fluid and structure meshes for aeroelastic computations: a parallel approach. *Computers & Structures*, 54(4):779–785.

Melia, N., Haines, K., and Hawkins, E. (2017). Implications from opening arctic sea routes.

Mesa, J. (2018). *Hydroelastic Analysis of Aluminum and Composite High-Speed Planing Craft Structures During Slamming*. PhD thesis.

Mesa, J. D., Maki, K. J., and Graham, M. T. (2022). Numerical analysis of the impact of an inclined plate with water at high horizontal velocity. *Journal of Fluids and Structures*, 114:103684.

Michell, J. (1898). Wave-resistance of a ship. *Phil. Mag.*, 45(272):106–123.

Mokus, N. G. A. and Montiel, F. (2022). Wave-triggered breakup in the marginal ice zone generates lognormal floe size distributions: a simulation study. *The Cryosphere*, 16(10):4447–4472.

Montiel, F. and Mokus, N. (2022). Theoretical framework for the emergent floe size distribution in the marginal ice zone: the case for log-normality. *Philosophical Transactions of the Royal Society A*, 380(2235):20210257.

Montiel, F. and Squire, V. A. (2017). Modelling wave-induced sea ice break-up in the marginal ice zone. *Proceedings of the Royal Society A: Mathematical, Physical and Engineering Sciences*, 473(2206):20170258.

Mulherin, N. D. et al. (1996). The northern sea route-its development and evolving state of operations in the 1990s.

Myland, D. and Ehlers, S. (2016). Influence of bow design on ice breaking resistance. *Ocean engineering*, 119:217–232.

Nelli, F., Bennetts, L., Skene, D., Monty, J., Lee, J., Meylan, M., and Toffoli, A. (2017a). Reflection and transmission of regular water waves by a thin, floating plate. *Wave Motion*, 70:209–221.

Nelli, F., Skene, D. M., Bennetts, L. G., Meylan, M. H., Monty, J. P., and Toffoli, A. (2017b). Experimental and numerical models of wave reflection and transmission by an ice floe. In *International Conference on Offshore Mechanics and Arctic Engineering*, volume 57762, page V008T07A015. American Society of Mechanical Engineers.

Newman, J. N. (1962). Wave resistance of a moving pressure distribution in a canal. *DTMB report*.

Newman, J. N. (2018). *Marine hydrodynamics*. The MIT press.

Overland, J., Dunlea, E., Box, J. E., Corell, R., Forsius, M., Kattsov, V., Olsen, M. S., Pawlak, J., Reiersen, L.-O., and Wang, M. (2019). The urgency of arctic change. *Polar Science*, 21:6–13.

Overland, J. E. and Wang, M. (2013). When will the summer arctic be nearly sea ice free? *Geophysical Research Letters*, 40(10):2097–2101.

Peters, A. S. (1950). The effect of a floating mat on water waves. *Communications on Pure and Applied Mathematics*, 3(4):319–354.

Piro, D. J. (2013). *A hydroelastic method for the analysis of global ship response due to slamming events*. PhD thesis, University of Michigan.

Piro, D. J. and Maki, K. J. (2013). Hydroelastic analysis of bodies that enter and exit water. *Journal of Fluids and Structures*, 37:134–150.

Reddy, J. N. (2006). *Theory and analysis of elastic plates and shells*. CRC press.

Ren, K., Wu, G., and Li, Z. (2020). Hydroelastic waves propagating in an ice-covered channel. *Journal of Fluid Mechanics*, 886:A18.

Ren, K., Wu, G., and Thomas, G. (2016). Wave excited motion of a body floating on water confined between two semi-infinite ice sheets. *Physics of Fluids*, 28(12):127101.

Riska, K., Leiviskä, T., Nyman, T., Fransson, L., Lehtonen, J., Eronen, H., and Backman, A. (2001). Ice performance of the swedish multi-purpose icebreaker tor viking ii. In *Proceedings of the International Conference on Port and Ocean Engineering Under Arctic Conditions*.

Shishmarev, K., Khabakhpasheva, T., and Korobkin, A. (2016). The response of ice cover to a load moving along a frozen channel. *Applied Ocean Research*, 59:313–326.

Shishmarev, K., Khabakhpasheva, T., and Korobkin, A. (2019). Ice response to an underwater body moving in a frozen channel. *Applied Ocean Research*, 91:101877.

Skene, D., Bennetts, L., Meylan, M., and Toffoli, A. (2015). Modelling water wave overwash of a thin floating plate. *Journal of Fluid Mechanics*, 777:R3.

Skene, D., Bennetts, L., Wright, M., Meylan, M., and Maki, K. (2018). Water wave overwash of a step. *Journal of Fluid Mechanics*, 839:293–312.

Smith, L. C. and Stephenson, S. R. (2013). New trans-arctic shipping routes navigable by midcentury. *Proceedings of the National Academy of Sciences*, 110(13):E1191–E1195.

Sorensen, R. (2017). Ship-generated waves. *Advances in Hydroscience*, 9:49–83.

Spalart, P. and Allmaras, S. (1992). A one-equation turbulence model for aerodynamic flows. In *30th aerospace sciences meeting and exhibit*, page 439.

Spalding, D. (1961). A single formula for the "law of the wall". *Journal of Applied Mechanics*, 28(3):455.

Spencer, D. (1992). A standard method for the conduct and analysis of ice resistance model tests. In *SNAME American Towing Tank Conference*, page D011S008R003. SNAME.

Squire, V., Hosking, R. J., Kerr, A. D., and Langhorne, P. (1996). *Moving loads on ice plates*, volume 45. Springer Science & Business Media.

Squire, V. A. (1984). A theoretical, laboratory, and field study of ice-coupled waves. *Journal of Geophysical Research: Oceans*, 89(C5):8069–8079.

Squire, V. A. (2020). Ocean wave interactions with sea ice: A reappraisal. *Annual Review of Fluid Mechanics*, 52:37–60.

Sree, D. K., Law, A. W.-K., and Shen, H. H. (2017). An experimental study on the interactions between surface waves and floating viscoelastic covers. *Wave Motion*, 70:195–208.

Su, B., Riska, K., and Moan, T. (2010). A numerical method for the prediction of ship performance in level ice. *Cold Regions Science and Technology*, 60(3):177–188.

Timco, G. and Weeks, W. (2010). A review of the engineering properties of sea ice. *Cold regions science and technology*, 60(2):107–129.

Toffoli, A., Bennetts, L. G., Meylan, M. H., Cavaliere, C., Alberello, A., Elsnab, J., and Monty, J. P. (2015). Sea ice floes dissipate the energy of steep ocean waves. *Geophysical Research Letters*, 42(20):8547–8554.

Tuck, E. O. and Lazauskas, L. (1998). Optimum hull spacing of a family of multihulls. *Ship Technology Research-Schiffstechnik*, 45(4):180.

Tuković, Ž., Karač, A., Cardiff, P., Jasak, H., and Ivanković, A. (2018). Openfoam finite volume solver for fluid-solid interaction. *Transactions of FAMENA*, 42(3):1–31.

Untersteiner, N. (2013). *The geophysics of sea ice*. Springer.

Valanto, P. (2001). On the cause and distribution of resistance forces on ship hulls moving in level ice. In *Proceedings of the International Conference on Port and Ocean Engineering under Arctic Conditions*.

Wadhams, P. (1973). Attenuation of swell by sea ice. *Journal of Geophysical Research*, 78(18):3552–3563.

Wadhams, P. and Holt, B. (1991). Waves in frazil and pancake ice and their detection in seasat synthetic aperture radar imagery. *Journal of Geophysical Research: Oceans*, 96(C5):8835–8852.

Wang, R. and Shen, H. H. (2010). Gravity waves propagating into an ice-covered ocean: A viscoelastic model. *Journal of Geophysical Research: Oceans*, 115(C6).

Weber, J. E. (1987). Wave attenuation and wave drift in the marginal ice zone. *Journal of physical oceanography*, 17(12):2351–2361.

Weiss, J., Schulson, E. M., and Stern, H. L. (2007). Sea ice rheology from in-situ, satellite and laboratory observations: Fracture and friction. *Earth and Planetary Science Letters*, 255(1-2):1–8.

Williams, T. D., Bennetts, L. G., Squire, V. A., Dumont, D., and Bertino, L. (2013). Wave–ice interactions in the marginal ice zone. part 1: Theoretical foundations. *Ocean Modelling*, 71:81–91.

Windt, C., Davidson, J., Chandar, D. D., Faedo, N., and Ringwood, J. V. (2020). Evaluation of the overset grid method for control studies of wave energy converters in openfoam numerical wave tanks. *Journal of Ocean Engineering and Marine Energy*, 6(1):55–70.

Xue, Y., Zeng, L., Ni, B., Korobkin, A., and Khabakhpasheva, T. (2021). Hydroelastic response of an ice sheet with a lead to a moving load. *Physics of Fluids*, 33(3):037109.

Yiew, L., Bennetts, L., Meylan, M., French, B., and Thomas, G. (2016). Hydrodynamic responses of a thin floating disk to regular waves. *Ocean Modelling*, 97:52–64.

Zeng, L., Korobkin, A., Ni, B., and Xue, Y. (2021). Flexural-gravity waves in ice channel with a lead. *Journal of Fluid Mechanics*, 921:A10.

Zhang, Z. and Maki, K. (2023). Wave resistance of a ship moving in a lead between rigid ice sheets of finite thickness. *Physics of Fluids*, 35(7).